MODELING THE SPATIAL STRUCTURE OF DEBRIS DISKS

Simultaneous multi-wavelength modeling and predictions on the observability of planet-disk interaction

Dissertation
zur Erlangung des Doktorgrades
der Mathematisch-Naturwissenschaftlichen Fakultät
der Christian-Albrechts-Universität zu Kiel

vorgelegt von
Steve Ertel
Kiel, 2011

Referent: Prof. Dr. Sebastian Wolf

Koreferent: Prof. Dr. Holger Kersten

Tag der mündlichen Prüfung: 07.02.2012

Zum Druck genehmigt: 07.02.2012

gez. Prof. Dr. Lutz Kipp, Dekan

To those who are more important
to me than this work

Ach! was in tiefer Brust uns da entsprungen,
Was sich die Lippe schüchtern vorgelallt,
Mißraten jetzt und jetzt vielleicht gelungen,
Verschlingt des wilden Augenblicks Gewalt.
Oft wenn es erst durch Jahre durchgedrungen
Erscheint es in vollendeter Gestalt.
Was glänzt ist für den Augenblick geboren;
Das Echte bleibt der Nachwelt unverloren.

(Goethe, Faust, Vorspiel auf dem Theater)

Abstract

The content of the present thesis can be grouped in two main topics: (1) The modeling of the spatial dust distribution in debris disks from available high spatial resolution, high quality data. (2) The modeling of planet-disk interaction in debris disks, the investigation of the observability of this process with present and near future instruments, and the preparation and execution of new observations of debris disks.

Debris disks are evolved dust disks (mostly) around main sequence stars. The dust detected in such disks must be transient or, more likely, continuously replenished by ongoing collisions of bigger objects like planetesimals left over from the planet formation process. A correlation between the existence of planets and debris disks is expected. The spatial distribution of the dust in debris disks is expected to be mainly influenced by the distribution of the parent bodies, by stellar gravity and radiation, and by the gravitational interaction with possible planets. Thus, structures in the spatial dust distribution can give insight into the configuration of the underlaying planetary/planetesimal system. As the most readily detectable signposts of other planetary systems, debris disks help us to improve our understanding of the formation and evolution of them as well as of our own solar system.

In this thesis, analytical model fitting is employed for simultaneous multi-wavelength modeling of available high quality data of debris disks. This allows to extract the most complete set of information possible about the systems modeled. Detailed modeling of the HD 107146 debris disk reveals the configuration of the system. The potential discovery of a new class of debris disks with a very strong underabundance of large grains is presented. Modeling of spatially resolved data of two debris disks obtained with *Herschel* reveals unexpected properties like an outwards increasing surface density or a multi-ring structure.

Furthermore, N-body simulations are employed to study the structures induced in debris disks due to planet-disk interaction. From these data, the observability of the found structures with present and future instruments is investigated. Planet-disk interaction is found to produce structures in debris disks that allow to constrain the configuration of a system. These structures will be observable with near-future instruments.

Finally, strategies for spatially resolved imaging of debris disks are developed and employed for new observations. An observing project accepted for execution during ALMA Early Science is presented. Furthermore, the first spatially resolved data of the dust in the habitable zone of the system around ϵ Eridani – obtained in the context of this thesis – are presented.

Zusammenfassung

Die Zielstellung der vorliegenden Dissertation kann in zwei Gebiete unterteilt werden: (1) Die Modellierung der räumlichen Staubverteilung in Debris-Scheiben anhand verfügbarer hochauflösender, qualitativ hochwertiger Daten. (2) Die Modellierung von Planet-Scheibe-Wechselwirkung in Debris-Scheiben, die Untersuchung der Beobachtbarkeit dieses Prozesses mit Hilfe aktueller und zukünftiger Instrumente, sowie die Vorbereitung und Durchführung neuer Beobachtungen von Debris-Scheiben.

Debris-Scheiben sind Staubscheiben um (hauptsächlich) Hauptreihensterne. Staub in solchen Scheiben kann nur kurzzeitig existieren – oder wahrscheinlicher – muss durch Kollisionen von großen Objekten wie Planetesimalen kontinuierlich erzeugt werden. Solche Planetesimale werden als Nebenprodukt der Planetenentstehung erwartet. Eine Verbindung zwischen der Existenz von Planeten und Debris-Scheiben wird angenommen. Die räumliche Verteilung des Staubes in Debris-Scheiben wird im Wesentlichen durch die Verteilung der ihn erzeugenden Körper, die stellare Gravitation und Strahlung und die gravitative Wechselwirkung mit möglichen Planeten beeinflusst. Daher können Strukturen in der räumlichen Staubverteilung Aufschluss über die Anordnung des sie erzeugenden Planeten/Planetesimalsystems geben. Als die am besten beobachtbaren Anzeichen anderer Planetensysteme helfen Debris-Scheiben, unser Verständnis der Entstehung und Entwicklung dieser Systeme, aber auch unseres eigenen Sonnensystems zu vertiefen.

In dieser Arbeit werden analytische Modelle verwendet um verfügbare Daten hoher Qualität über einen breiten Wellenlängenbereich simultan anzunähern. So kann ein Optimum an Informationen über die modellierten Systeme gewonnen werden. Die detaillierte Modellierung der Debris-Scheibe um HD 107146 fördert die Konfiguration dieses Systems zu Tage. Die mögliche Entdeckung einer neuer Klasse von Debris-Scheiben mit einem starken Mangel an großen Teilchen wird präsentiert. Die Modellierung durch *Herschel* gewonnener, räumlich aufgelöster Daten zweier Scheiben deckt unerwartete Eigenschaften auf, wie eine nach außen ansteigende Oberflächendichte oder eine Konfiguration aus mehreren Staubringen.

Außerdem werden Vielteilchensimulationen verwendet um Strukturen in Debris-Scheiben durch Planet-Scheibe-Wechselwirkung zu untersuchen. Mit Hilfe der gewonnenen Daten wird die Beobachtbarkeit der gefundenen Strukturen mit aktuellen und zukünftigen Instrumenten untersucht. Es wird gezeigt, dass Planet-Scheibe-Wechselwirkung Strukturen in Debris-Scheiben erzeugt, die es erlauben, die Konfiguration des für sie verantwortlichen Systems zu untersuchen. In naher Zukunft verfügbare Instrumente werden es erlauben, solche Strukturen zu beobachten.

Zuletzt werden Strategien zur räumlich aufgelösten Beobachtung von Debris-Scheiben entwickelt und für neue Beobachtungen angewandt. Ein Beobachtungsprojekt, das für die Durchführung im Rahmen von ALMA Early Science akzeptiert wurde, wird vorgestellt. Außerdem werden die ersten räumlich aufgelösten Daten des Staubes in der habitablen Zone des Systems um ϵ Eridani vorgestellt, die im Rahmen dieser Arbeit gewonnen wurden.

Contents

1 Introduction

Where do we come from? Are we alone in the universe? These are two fundamental questions of mankind. The first question is closely connected with the formation and evolution of our planet Earth and more general with the formation of our Sun and the Solar System. The second question not only addresses the existence of extraterrestrial life in our Solar System, but also on extrasolar planets, being closely connected with the search for other planetary systems. Thus, the formation and evolution of stars, planets, and planetary systems in general is a fundamental part of these questions.

The topic of the present thesis – the modeling of the spatial dust distribution in debris disks – represents one way to address these questions. There are different stages of star and planet formation. Molecular clouds represent the stellar nursery and allow one to study the raw material as well as the very first steps of star formation. Protoplanetary disks and more evolved transitional disks represent the next steps, where the formation of the central star(s) is already in its late stages. These optically thick gas and dust disks around protostars are believed to be the nursery of planets and planetary systems. There, the processes and conditions can be studied, under which planetary systems and maybe also the building blocks of life form. The outcome of these processes can be studied on the example of our own Solar System as well as on the various other planetary systems and debris disks discovered mostly around main sequence stars over the last three decades. The results from the studies of debris disks give strong and valuable constraints on the processes that lead to the configurations of the systems observed. Furthermore, they allow one to study the evolution of planetary systems after the most turbulent phase of their formation has finished. Our own Solar System only represents a snapshot of this evolution on the example of one particular realization. Finally, studies of debris disks give an insight into the environment in which planets like our Earth evolve and form the conditions under which they may harbor life. A last but not least field of research is the evolution of planetary systems around stars that leave the main sequence and evolve, i.e., to white dwarfs. This field of research is connected to the question about the future of our Solar System (Kilic et al. 2006; Jura et al. 2007; Melis et al. 2010).

The above discussion always distinguishes between planets and planetary systems. The reason for this is that planets are not the only components of such a system. Like the Asteroid Belt, the Kuiper Belt, and comets in our Solar System, planetesimal and cometary populations are believed to be a common by-product of planet formation (Safronov & Zvjagina 1969; Wetherill 1980; Lissauer 1987). Collisions between planetesimals as well as possible collisions between planets and the evaporation of comets result in a reasonable amount of small (micron-sized to millimeter-sized) dust grains. These particles are usually meant with the term “debris disk”. Due to the large surface to volume ratio of these dust par-

ticles, they are efficient radiators of thermal emission and scatterers of stellar light. This makes them the most readily detectable signposts of planetary systems. The dust detected in such disks is thought to be removed from those systems by the stellar radiation on short time scales compared to the system's age (Backman & Paresce 1993). Thus, it must be transient or more likely continuously replenished. The composition of the dust particles provides valuable constraints on the composition of the larger bodies. For isolated systems, the spatial distribution of the planetesimals and the circumstellar dust can be influenced by gravitational interaction with planets in addition to the influence of the star (Dominik & Decin 2003; Kenyon & Bromley 2004; Strubbe & Chiang 2006; Wyatt 2008). Together with an understanding of the details of dust creation mechanisms, the spatial dust distribution provides constraints on the dynamical state as well as the spatial distribution of the planetesimals and on the configuration of the planetary system.

The aims of the present thesis can be grouped in two main topics and motivated as follows:

(1) The detailed simultaneous multi-wavelength modeling of latest high quality, high spatial resolution data to extract the most complete set of information possible. This allows one to investigate what we can already conclude on the spatial structure of debris disks from available data.

(2) The modeling of planet-disk interaction in debris disks and the simulation of the observability of this process with present and future instruments. This allows one to develop strategies for specialized observations to search for the signposts of this process and to put strong constraints on the systems to be found from these observations.

The stage for the present work is set by introducing the basics of debris disk research in Chapt. 2 (physics), Chapt. 3 (observations), and Chapt. 4 (modeling). The toolbox developed in the context of the present work to account for the high quality data to be modeled is described in Chapt. 5.

In Chapt. 6, the work starts with the combined multi-wavelength modeling of high quality data of one particular debris disks, HD 107146. This face-on seen disk has been spatially resolved at optical and near-infrared wavelengths (Ardila et al. 2004; Ertel et al. 2011). At these wavelengths, the highest spatial resolution possible is reached. These observations allow one to put strong constraints on the distribution of the micron-sized grains in the system. In addition, HD 107146 has also been resolved at (sub-)mm wavelengths (Corder et al. 2009; Hughes et al. 2011). Thus, it represents one of the best candidates available for detailed modeling, but also challenges the modeling to account for the large amount of complementary data available.

In Chapts. 7 and 8, the detailed modeling of data from the *Herschel* open time key program DUNES (DUst around NEarby Stars, Eiroa et al. 2010; Liseau et al. 2010) is presented. These data represent the highest quality far-infrared data at the highest spatial resolution available and provide the strongest constraints on the systems. They allow one to put constraints on the spatial distribution of larger (millimeter-sized) grains that is expected to be closer to that of the planetesimals compared to the distribution of the

micron-sized grains. However, due to the still limited spatial resolution, detailed modeling is necessary to extract these information. In Chapt. 7, the potential discovery of a new class of peculiar debris disks with an unusually steep spectral energy distribution from 70 μm to 160 μm is presented. It is demonstrated that even a few spatially unresolved, photometric data points can constrain some parameters of the systems in this peculiar case. The peculiarity of these systems is discussed qualitatively and through detailed modeling. The modeling of two debris disks spatially resolved by *Herschel* – q^1 Eridani and HD 207129 – is described in Chapt. 8. It is demonstrated that the *Herschel* observations and modeling are the first to reveal the unexpected spatial distribution of the dust – an outwards increasing surface density or a multi-ring structure.

Detailed studies of the spatial structure of debris disks were until now only possible for a small number of nearby, bright targets. The Atacama Large Millimeter/submillimeter Array (ALMA) will allow for the first time for such studies of a large number of debris disks in the near future due to its high spatial resolution and sensitivity. Furthermore, it will allow for high sensitivity interferometric observations in the (sub-)mm with a maximum spatial resolution comparable to that of an eight meter class telescope in the optical. Thus, it is expected to be the first instrument to unequivocally reveal planet-disk interaction in debris disks. To prepare for its availability, sensitivity studies are carried out and presented in Chapt. 9. Dynamical simulations of planet-disk interaction are carried out and the observability of the structures induced in the disks is investigated in Chapt. 10. In particular, a combination of ALMA observations with high sensitivity observations at sub-arcsecond spatial resolution in the mid-infrared as expected from near-future space based instruments like the *James Webb* Space Telescope (JWST) is expected to put very strong constraints on extrasolar planetary/planetesimal systems. The first ALMA observations of a debris disk (AU Microscopii) accepted for Early Science based on the studies presented in this work are described in Chapt. 11. Already at this early stage of ALMA, the data obtained will exceed all earlier (sub-)mm observations of debris disks.

Mid-infrared instruments like the VLT Imager and Spectrometer for the mid-InfraRed (VISIR) at one of the Very Large Telescopes (VLT) are the closest to the specifications of the JWST allowing for observations with comparable spatial resolution, but with significantly lower sensitivity. An observing program carried out with VISIR to explore what is already possible with this instrument is presented in Chapt. 12. As a result, the first spatially resolved data of the dust in the habitable zone of ϵ Eridani are presented. These data provide strong constraints on the models to explain the presence of this dust.

The results are summarized in Chapt. 13 and an outlook is given there.

2 Physics of debris disks

The term debris disk usually includes every sub-planetary object in a planetary system like planetesimals, comets, and dust. Sometimes, even planets are considered to be part of the disk. However, the micron-sized to millimeter-sized dust is the most visible component of all debris disks known. The major influences on the dust particles in a debris disk are the stellar radiation and gravity. Stellar radiation is heating the dust particles and is scattered by them making them visible to us. Furthermore, it influences their dynamics in addition to the stellar gravity. Additionally, possible planets may influence the dust dynamics. In the following, the basic physics of these processes relevant for the present work is introduced.

2.1 Irradiated dust particles

In this section, the interaction between dust particles and stellar radiation is discussed. Only radiative processes are considered, while dynamical effects are discussed in Sect. 2.2. Debris disks are considered to be optically thin on any line of sight in the system to both the stellar radiation and the radiation emitted by the dust grains. It is further considered that the stellar radiation dominates the irradiation on the dust grains and that the irradiation from the other dust grains is negligible. Finally, the dust is considered to be in thermal equilibrium with the stellar radiation.

2.1.1 Mie theory

The interaction of a dust particle with incident radiation (of wavelength λ) can be described by Mie theory. A detailed description of Mie theory can be found in Bohren & Huffman (1983) and a numerical implementation has been published, e.g., by Wolf & Voshchinnikov (2004). Here, the most important quantities that result from Mie theory and that are used to describe the effects on a dust particle due to the stellar radiation are introduced. In the following, the dust particle is assumed to be spherical with radius a, compact, and homogeneous. The optical properties of the particle are determined by its complex refractive index

$$m = n + \mathrm{i}k \tag{2.1}$$

and its size parameter

$$x = \frac{2\pi a}{\lambda}. \tag{2.2}$$

The incident radiation can be described by the four-component Stokes vector $\boldsymbol{I} = (I, Q, U, V)^{\mathrm{T}}$. The Müller matrix or scattering matrix $\mathbf{S}$ describes the scattering of radiation by the particle, where $\boldsymbol{I}_0$ and $\boldsymbol{I}_1$ are the Stokes vectors before and after the scattering process:

$$\boldsymbol{I}_1 \propto \mathbf{S}\boldsymbol{I}_0. \tag{2.3}$$

The Müller matrix can be written as

$$\mathbf{S}(\theta) = \begin{pmatrix} S_{11}(\theta) & S_{12}(\theta) & 0 & 0 \\ S_{12}(\theta) & S_{11}(\theta) & 0 & 0 \\ 0 & 0 & S_{33}(\theta) & S_{34}(\theta) \\ 0 & 0 & -S_{34}(\theta) & S_{33}(\theta) \end{pmatrix}. \tag{2.4}$$

Here, θ denotes the scattering angle, i.e., the angle between the directions of incident and scattered radiation. Note that $\boldsymbol{I}$ and $\mathbf{S}$ are wavelength-dependent. Furthermore, the absorption efficiency $Q_\lambda^{\mathrm{abs}}(a)$, the scattering efficiency $Q_\lambda^{\mathrm{sca}}(a)$, and the radiation pressure efficiency $Q_\lambda^{\mathrm{pr}}(a)$ are necessary to describe the interaction of a dust particle with the stellar radiation as discussed in the following.

2.1.2 Absorption, thermal re-emission, and dust temperature

The emission of the star can be described by its monochromatic luminosity $L_{\lambda,\star}$. Employing the assumptions made before, the monochromatic power W_λ^{abs} absorbed and W_λ^{emi} re-emitted by a spherical dust grain with a temperature T_{g} at a distance r from the star can be described as

$$W_\lambda^{\mathrm{abs}} = L_{\lambda,\star}\, Q_\lambda^{\mathrm{abs}}(a)\, \frac{\pi a^2}{4\pi r^2} \tag{2.5}$$

and

$$W_\lambda^{\mathrm{emi}} = 4\pi\, a^2\; Q_\lambda^{\mathrm{abs}}(a)\; B_\lambda\left(T_{\mathrm{g}}\right). \tag{2.6}$$

Here, $B_\lambda(T)$ is the specific spectral radiance described by Planck's law. Using

$$\int_0^\infty W_\lambda^{\mathrm{emi}}\, d\lambda = \int_0^\infty W_\lambda^{\mathrm{abs}}\, d\lambda, \tag{2.7}$$

one can derive the temperature T_{g}. The resulting equation can only be expressed as an equation of $r(T_{\mathrm{g}})$:

$$r(T_{\mathrm{g}}) = \sqrt{\frac{1}{16\pi} \frac{\int_0^\infty Q_\lambda^{\mathrm{abs}}(a)\, L_{\lambda,\star}\, d\lambda}{\int_0^\infty Q_\lambda^{\mathrm{abs}}(a)\, B_\lambda(T_{\mathrm{g}})\, d\lambda}}. \tag{2.8}$$

If the star is treated as a black body radiator with temperature $T_\star$ and radius $R_\star$ ($L_{\lambda,\star} = 4\pi R_\star^2 B_\lambda\left(T_\star\right)$), Eq. 2.8 can then be expressed as

$$r(T_{\mathrm{g}}) = \frac{R_\star}{2} \sqrt{\frac{\int_0^\infty Q_\lambda^{\mathrm{abs}}(a)\, B_\lambda(T_\star)\, d\lambda}{\int_0^\infty Q_\lambda^{\mathrm{abs}}(a)\, B_\lambda(T_{\mathrm{g}})\, d\lambda}}. \tag{2.9}$$

2.1.3 Scattering of stellar radiation

In addition to its thermal re-emission, the dust also scatters stellar radiation. The total power scattered by a dust grain can be expressed as

$$W_\lambda^{\mathrm{sca}} = L_{\lambda,\star}\, Q_\lambda^{\mathrm{sca}}(a)\, \frac{\pi a^2}{4\pi r^2}. \tag{2.10}$$

The dependence on the scattering angle θ is introduced by the Müller matrix. Since the stellar radiation can be considered to be unpolarized and multiple scattering can be neglected in optically thin debris disks, $\boldsymbol{I}_0$ in Eq. 2.3 can be written as $(I_0, 0, 0, 0)^{\mathrm{T}}$. One finds

$$I_1 \propto S_{11}(\theta) I_0 \tag{2.11}$$
$$Q_1 \propto S_{12}(\theta) I_0. \tag{2.12}$$

Thus, the angle-dependent power scattered by a dust particle can be expressed as

$$W_{\lambda,\theta}^{\mathrm{sca}}\, d\theta = L_{\lambda,\star}\, Q_\lambda^{\mathrm{sca}}(a)\, \frac{\pi a^2}{4\pi r^2} S_{11}(\theta)\, d\theta. \tag{2.13}$$

Analogous, the angle dependent power of polarized scattered radiation can be expressed as

$$(W_{\lambda,\theta}^{\mathrm{sca}})_{\mathrm{pol}}\, d\theta = L_{\lambda,\star}\, Q_\lambda^{\mathrm{sca}}(a)\, \frac{\pi a^2}{4\pi r^2} S_{12}(\theta)\, d\theta. \tag{2.14}$$

Here, it is assumed that the Müller matrix is normalized to

$$\int_0^{2\pi} \int_0^{\pi} S_{11}(\theta)\, d\theta\, d\phi = 1, \tag{2.15}$$

which results in the sign "=" instead of "$\propto$" in Eq. 2.13 and 2.14 due to

$$\begin{aligned} \int_0^{2\pi} \int_0^{\pi} W_{\lambda,\theta}^{\mathrm{sca}}\, d\theta\, d\phi &= L_{\lambda,\star}\, Q_\lambda^{\mathrm{sca}}(a)\, \frac{\pi a^2}{4\pi r^2} \int_0^{2\pi} \int_0^{\pi} S_{11}(\theta)\, d\theta\, d\phi \\ &\stackrel{!}{=} L_{\lambda,\star}\, Q_\lambda^{\mathrm{sca}}(a)\, \frac{\pi a^2}{4\pi r^2} = W_\lambda^{\mathrm{sca}}. \end{aligned} \tag{2.16}$$

From Eq. 2.13 and 2.14 the degree of polarization p can be computed:

$$p = \frac{(W_{\lambda,\theta}^{\mathrm{sca}})_{\mathrm{pol}}}{W_{\lambda,\theta}^{\mathrm{sca}}} = \frac{S_{12}}{S_{11}}. \tag{2.17}$$

2.2 Dynamics of debris disks

2.2.1 One particle around one star

The interaction of a dust grain with the stellar radiation results in a number of dynamical effects in addition to the processes described above. These effects on the dynamics of a single dust particle around a star are the subject of this section.

Radiation pressure and β parameter

A dust grain with a mass m_g orbiting a star with the mass $M_\star$ at a distance r is primarily affected by two forces. These are the stellar gravitational force

$$\boldsymbol{F}_\mathrm{G} = -\frac{GM_\star m_\mathrm{g}}{r^2}\frac{\boldsymbol{r}}{r} \tag{2.18}$$

and the force on the dust grain resulting from radiation pressure

$$\boldsymbol{F}_\mathrm{R} = \frac{A\int_0^\infty L_{\lambda,\star}Q_\lambda^\mathrm{pr}(a)\;d\lambda}{4\pi r^2 c}\frac{\boldsymbol{r}}{r}. \tag{2.19}$$

Here, G is the gravitational constant, A is the cross section of the particle, and c is the vacuum speed of light. One can introduce the dimensionless quantity β:

$$\beta = \frac{|\boldsymbol{F}_\mathrm{R}|}{|\boldsymbol{F}_\mathrm{G}|} = \frac{A\int_0^\infty L_{\lambda,\star}Q_\lambda^\mathrm{pr}(a)\;d\lambda}{4\pi cGM_\star m_\mathrm{g}}. \tag{2.20}$$

Assuming a spherical, compact, and homogeneous dust particle with a bulk density ρ_g, one can express the particle cross section by $A = \pi a^2$ and the particle mass by $m_\mathrm{g} = 4/3\;\pi a^3\rho_\mathrm{g}$:

$$\beta = \frac{3}{16\pi}\frac{\int_0^\infty L_{\lambda,\star}Q_\lambda^\mathrm{pr}(a)\;d\lambda}{cGM_\star a\rho_\mathrm{g}}. \tag{2.21}$$

It is remarkable that the value of β is independent from the distance from the star, but depends on the properties of the dust particle (a, ρ_g, $Q_\lambda^\mathrm{pr}(a)$) and on the stellar properties ($M_\star$, $L_{\lambda,\star}$). The net force on a particle considering radiation pressure can be written as

$$\boldsymbol{F}_\mathrm{G+R} = (1-\beta)\boldsymbol{F}_\mathrm{G}. \tag{2.22}$$

For sufficiently large grains, one can apply a geometrical optics approximation

$$Q_\lambda^\mathrm{pr} = \frac{\int_0^\infty Q_\lambda^\mathrm{pr}L_{\lambda,\star}\;d\lambda}{\int_0^\infty L_{\lambda,\star}\;d\lambda} \approx 1. \tag{2.23}$$

This results in

$$\boldsymbol{F}_\mathrm{R} \approx \frac{AL_\star}{4\pi r^2 c}\frac{\boldsymbol{r}}{r} \tag{2.24}$$

and

$$\beta \approx \frac{AL_\star}{4\pi cGM_\star m_\mathrm{g}} = \frac{3}{16\pi}\frac{L_\star}{cGM_\star a\rho_\mathrm{g}} \propto \frac{1}{a}, \tag{2.25}$$

with $L_\star = \int_0^\infty L_{\lambda,\star}\;d\lambda$. A formula to express β in convenient numbers was given by Wyatt et al. (1999):

$$\beta \approx 575\left(\frac{\rho_\mathrm{g}}{\mathrm{kg\,m^{-3}}}\right)^{-1}\left(\frac{a}{\mu\mathrm{m}}\right)^{-1}\left(\frac{L_\star}{\mathrm{L}_\odot}\right)\left(\frac{M_\star}{M_\odot}\right)^{-1}. \tag{2.26}$$

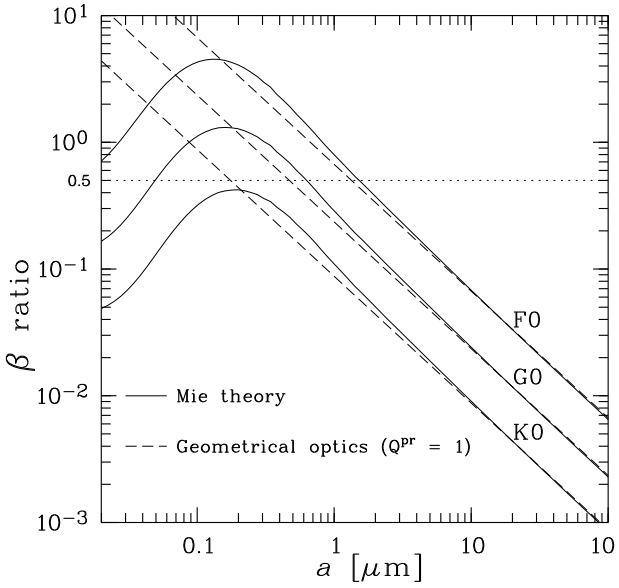

Fig. 2.1: β ratio for different Sun-like stars (implemented as black body radiators) and astronomical silicate dust ($\rho_\mathrm{g} = 3.5\,\mathrm{g/cm^3}$, Draine 2003) derived from Mie theory (Eq. 2.21) and using the geometrical optics approximation (Eq. 2.25). The spectral type is indicated at the lower right of each curve. Stellar properties $M_\star$ and $L_\star$ are taken from Binney & Merrifield (1998).

The value of β as a function of the grain size for astronomical silicate (Draine 2003) around Sun-like stars (implemented as black body radiators) as well as the corresponding curves for the geometrical optics approximation can be seen in Fig. 2.1. From this figure, one can also see what was meant before by the term "sufficiently large grains".

As the radiation pressure counteracts the stellar gravity, there are values of β that result in a liberation of the particle from the system (at least for bright stars, depending on the behaviour of $Q_\lambda^\mathrm{pr}(a)$, see Fig. 2.1). A particle released from a parent body on a circular orbit[1] without receiving any additional momentum is unbound, if its kinetic energy is equal to (or larger than) its potential energy:

$$\frac{m_\mathrm{g}}{2} v^2 \geq \frac{G m_\mathrm{g} M_\star\,(1-\beta)}{r}. \tag{2.27}$$

With $v^2 = GM_\star/r$, this results in

$$\beta \geq \frac{1}{2}. \tag{2.28}$$

An extension of the discussion for parent bodies on an excentrical orbit is given, e.g., by Rodmann (2006).

[1]Simplification: The parent body is large enough not to be affected by radiation pressure.

Poynting-Robertson drag

The star is further treated as a point source. Furthermore, the geometrical optics approximation (Eq. 2.23) is applied. Since the moving particle intercepts stellar photons with finite velocity c, the direction of the incident radiation in the particle's reference frame is not perpendicular to the direction of the particle's motion, even in the case of a circular orbit. This results in a force $\boldsymbol{F}_{\mathrm{PR}}$ on the particle in direction opposite to the direction of its motion, called Poynting-Robertson drag force (Poynting 1903; Robertson 1937; Burns et al. 1979). The result of the continuous deceleration of the particle is a continuous loss of orbital energy, i.e., the particle spirals towards the star. A formula to estimate the time it takes a particle to spiral towards the star from a distance r_0 to its sublimation radius – called the Poynting-Robertson time scale – is given by Gustafson (1994):

$$t_{\mathrm{PR}} \approx \frac{400}{\beta} \left(\frac{M_\star}{\mathrm{M}_\odot}\right)^{-1} \left(\frac{r_0}{\mathrm{AU}}\right)^2 \mathrm{yr}. \tag{2.29}$$

Stellar wind

Similarly to stellar radiation, stellar wind results in both a pressure force comparable to the radiation pressure and a drag force comparable to Poynting-Robertson drag. The momentum flux density of the solar wind has been measured to be approximately four orders of magnitude lower than that of the electromagnetic radiation (Burns et al. 1979; Gustafson 1994). Thus, stellar wind *pressure* can be neglected at least around Sun-like stars. In contrast, the stellar wind *drag* can have a significant contribution to the particle dynamics due to the low speed of the stellar wind (≈ 300 to $600\,\mathrm{km\,s^{-1}}$ in the Solar System; Schwenn & Marsch 1990) resulting in a much larger aberration angle for the corpuscular radiation than for the electromagnetic radiation. As both the Poynting-Robertson drag force and the stellar wind drag force can be described analogously, the stellar wind drag force can be expressed as a multiple of the Poynting-Robertson drag force, $\boldsymbol{F}_{\mathrm{SW}} = \zeta \boldsymbol{F}_{\mathrm{PR}}$ (Gustafson 1994). In the Solar System, a value of $\zeta \approx 0.35$ has been found for particles larger than $\sim 0.1\,\mu\mathrm{m}$ (Gustafson 1994; Holmes et al. 2003).

Other forces

The effect of *Lorentz force* on charged dust particles has been discussed, e.g., by Gustafson (1994), Holmes et al. (2003), and Rodmann (2006). Since the effect may cancel out, it is usually not considered in the particle dynamics in debris disks. The *Yarkovsky effect* only acts on large (meter-sized and larger), rotating bodies (Burns et al. 1979). Thus, it is not considered in the dust dynamics. The *interstellar medium flow* may significantly sculpt the dust distribution of a debris disk (e.g., Debes et al. 2009; Maness et al. 2009; Buenzli et al. 2010). Since only a small number of debris disks exhibit asymmetries that can clearly be ascribed to interstellar medium flow and since it can usually not be measured, this effect is neglected in most of the studies of debris disks.

2.2.2 Dynamical interaction with planets and large planetesimals in the disk

In addition to the stellar gravity and radiation, the gravitational interaction between dust particles and planets or large planetesimals in the system can have significant effect on the dust and planetesimal dynamics. The presence of large planetesimals in the disk results in higher dynamical excitation (self-stirring; e.g., Kenyon & Bromley 2004).

Being more massive but less frequent, planets may significantly sculpt the spatial distribution of the dust and planetesimals, trapping them into resonance, preventing dust grains from moving inwards due to Poynting-Robertson drag, and opening gaps or inner holes in the spatial distribution (e.g., Sicardy et al. 1993; Wyatt 2003). An important concept of the interaction of two bodies orbiting a central mass (e.g., a planet and a dust particle around a star) is the mean motion resonance. Let T_1 and T_2 be the orbital periods of two bodies orbiting a star. The mean angular velocities are then $n_{1,2} = 2\pi/T_{1,2}$. The two bodies are in mean motion resonance, if p and q are (small) integers in the following equation:

$$\frac{T_1}{T_2} = \frac{n_2}{n_1} = \frac{p}{p+q}, \tag{2.30}$$

(e.g., Murray & Dermott 1999). Body 1 completes $p + q$ orbits in the same time body 2 needs to complete p orbits. This results in periodic interaction. It is important to note that – in contrast to planets or planetesimals – for dust particles significantly affected by stellar radiation (Sect. 2.2.1), the angular velocity on a given orbit will not only depend on the central mass following Kepler's third law. This means that, e.g., a planet and a dust particle on the same orbit around a star will not have the same angular velocity and will, thus, not necessarily be in resonance.

2.2.3 Collisions between dust particles and planetesimals

As the term debris disk suggests, these objects are expected to mainly consist of collisional debris. Ongoing collisions are expected to play a major role in debris disk dynamics and temporal evolution. The reviews of Wyatt (2008) and Krivov (2010) give a broad overview of the collisional evolution of debris disks. Numeric approaches to simulate collisional processes in debris disks have been presented, e.g., by Kenyon & Bromley (2001), Thébault et al. (2003), and Löhne et al. (2008). The temporal evolution of the disk mass due to continuous destruction of large objects and removal of dust from the system has been described, e.g., by Wyatt (2008).

The collisional time scale in a debris disk can be estimated following Backman & Paresce (1993):

$$t_{\mathrm{coll}} \sim \frac{1}{\tau\omega}, \tag{2.31}$$

where τ is the vertical geometrical optical depth and ω is the angular velocity of a particle.

An analytical solution for the differential grain size distribution $dn(a)$ of the dust grains produced through collisions has been found by Dohnanyi (1969) under the assumptions of

an equilibrium collisional cascade:

- The range of grain sizes is infinite (grain sizes from 0 to ∞).
- The critical specific energy necessary to disrupt a particle is independent from the particle size.
- There are no additional forces acting on the dust particles (like radiation pressure or Poynting-Robertson drag).

The result is a power law dependence

$$dn(a) \propto a^{-3.5} da. \tag{2.32}$$

These assumptions are expected to result in a good approximation for very massive debris disks, where collisions dominate the dynamics of the dust. However, they are not necessarily satisfied for less massive disks. The effects of a blow-out size and significant Poynting-Robertson drag (Sect. 2.2.1) have been discussed by Krivov et al. (2006), Thébault & Augereau (2007), and Wyatt et al. (2011). Results are a wavy size distribution $dn(a)$ overlayed on the power-law found by Dohnanyi (1969) and a depletion of small grains ($\beta \sim 0.5$).

2.3 Chemical composition and physical shape of the dust

The chemical composition and physical shape of the dust in debris disks has significant effect on its scattering efficiency, temperature, thermal re-emission, and dynamics due to different optical properties and on its collisional evolution due to different material strength and shape. The composition of the interplanetary dust in the inner regions of our Solar System (zodiacal dust) has been studied directly (e.g., Grün et al. 2001; Yoneda et al. 1993) and through its spectral energy distribution (e.g., Reach 1997, 2010). Spectra of comets give insight into their composition (e.g., Crovisier et al. 1996; Wooden 2000) and observations of large bodies in the Kuiper belt help to constrain the composition of their surfaces (Brown et al. 1997, 2011). For debris disks, one can investigate the composition of the dust through spectroscopy of the prominent emission features in the near- to mid-infrared (e.g., silicate features like Olivine, Pyroxene at 10 μm to 30 μm), if there is dust that significantly emits in this wavelength regime. The results suggest a broad variety of crystalline and amorphous silicates, carbon, and also water ice to be present.

Since debris disks are a by product of star formation and the material processed there is the interstellar medium, one approach can be to assume the same chemical composition to be present. This composition has been studied, e.g., by Draine & Lee (1984), Draine (2003), and Draine & Fraisse (2009). The outcome of these studies is the so-called astronomical silicate (astrosil), a composite material that reproduces the features seen in the interstellar medium. However, since the dust is expected to be significantly processed during the disk evolution (Schmitt et al. 1997; Birnstiel et al. 2010; Oliveira et al. 2011), the assumption of the same chemical composition is not necessarily valid.

3 Observations of debris disks

In contrast to other fields of natural science, in astronomy it is usually not possible to study the objects through reproducible, influenceable experiments. Hence, astronomers are forced to study the processes going on in the cosmos through observations. The information one gets from the subjects of interest are nearly exclusively carried through electromagnetic radiation emitted or influenced by them. For debris disks, this is the radiation emitted by the star and scattered or absorbed and subsequently re-emitted by the dust grains. This radiation carries two basic types of information – spatial information and spectral information. Spatially resolved observations allow one to investigate the spatial distribution of the scattering/emitting dust. The spectral energy distribution (SED) of the radiation carries information about temperature (Wien's displacement law) and composition (emission features, $Q_\lambda^{\mathrm{abs}}(a)$) of the dust, while its temperature is again connected to its distance from the star. In the following, a general overview over the most important observational techniques relevant for observations of debris disks is given. In Sect. 3.2, the *Herschel* Open Time Key Program DUNES (DUst around NEarby Stars) is introduced, in the context of which parts of the present work are carried out. In Sect. 3.3, the general results from observations of debris disks and related research are summarized and our image of a "typical" debris disk is discussed.

3.1 Observational techniques

3.1.1 Observational basics and notations

The performance of astronomical instruments is limited by a number of physical and technical effects that degrade the outcome of an observation compared to a perfect image of the target:

- The Earth's turbulent atmosphere leads to *seeing*, i.e., diffraction of the light of a source on regions of different density in the sky. This results in a smearing of the obtained image for reasonably long exposures. Typical seeing is in the order of $1''$ at optical wavelengths. This is only relevant at optical to near-infrared wavelengths due to the high spatial resolution possible. Modern techniques like adaptive optics allow one to mitigate the effects of seeing.
- Neglecting the effect of seeing, the spatial resolution of a classical telescope will be *diffraction* limited. The image of a point source will be smeared out to a so-called point spread function (PSF, an Airy disk for an ideal, circular aperture). For two point

sources A and B that are to be separated clearly in an image, one usually wants the peak of source B to be at least in the first minimum of the Airy disk of source A. This results in the formal minimum angular resolution $\delta \approx 1.22\,\lambda/D$, where D is the diameter of the aperture. At far-infrared wavelengths or longer, the PSF is usually approximated by a Gaussian and called the beam of the telescope (resolution approximated by the full width at half maximum, FWHM, beam width). In particular at these wavelengths, a lot of extended targets like debris disks will be only marginally resolved, which means that the disk is not extended enough to resolve its spatial structure, but the image is significantly extended compared to the FWHM of a point source.

- An important limiting factor on the sensitivity of observations is *noise*. The significance of a detection of a source is quantified by the signal-to-noise ratio (SNR). An SNR < 3 usually means no significant detection, while an SNR > 5 usually means a clear detection. However, if one wants to detect substructures in extended disks, a much higher SNR is desirable, since the detection of the structure above/below the average level of the disk has to be significant.
- In addition to noise, one has to consider *background confusion* (alignment with other sources). The probability of that is increasing with decreasing angular resolution (i.e., towards longer wavelengths) and is particularly critical at far-infrared to millimeter wavelengths. Here, galactic infrared cirrus as well as background galaxies (often only appearing at these wavelengths) might be confused with a debris disk around a star. Since the number of such detections is increasing with sensitivity of the observations, background confusion results in an absolute detection limit of debris disks. This can till now only be overcome by increasing the spatial resolution of the observations.
- The last limitation of observations of debris disks to be mentioned here is the *absolute photometric calibration*. For spatially unresolved observations, this places a limit on the detectability of a debris disk around a star, independent from the total brightness of the system. Typical photometric uncertainties for space-based infrared telescopes are in the order of few percent. Even if the stellar photospheric flux can be predicted accurately (which is an additional but minor source of uncertainty), it will not be possible to detect additional flux from a disk of the order of a few percent of the total flux.

3.1.2 Broad band photometry

The dust thermal re-emission usually peaks at far-infrared wavelengths, i.e., around 100 μm. In this wavelength range, the dust emission may exceed the stellar photospheric emission by few orders of magnitude (above-photospheric excess emission, excess). Only very few debris disk systems exhibit significant excess emission at wavelengths shorter than $\approx 20\,\mu$m accessible to ground-based infrared instruments. In the long wavelength mid-infrared and the far-infrared, the Earth's atmosphere is opaque to electromagnetic radiation. As a consequence, most debris disks have been discovered by space-based facilities, i.e., the

Infrared Astronomical Satellite (IRAS; e.g., Aumann 1985; Walker & Wolstencroft 1988) including the first ever detection of a debris disk around Vega (Aumann et al. 1984), the Infrared Space Observatory (ISO; de Muizon 2005), and the *Spitzer* Space Telescope (e.g., Beichman et al. 2005*b*; Meyer et al. 2006; Bryden et al. 2006; Hillenbrand et al. 2008). These facilities provided photometric measurements up to a wavelength of 160 μm. Since end of 2009, several Key Programs on the *Herschel* Space Observatory are dedicated to the study of debris disks in the wavelength range of 70 μm to 500 μm (e.g., Augereau et al. 2008; Eiroa et al. 2010; Matthews et al. 2010). At (sub-)mm wavelengths, a number of large single dish telescopes like the *James Clerk Maxwell* Telescope (JCMT), the IRAM 30 m Telescope, the Caltech Submillimeter Observatory (CSO), or the Atacama Pathfinder Experiment (APEX) provide sufficiently high sensitivity to perform (mostly spatially unresolved) photometry of the brightest debris disks (e.g., Najita & Williams 2005; Roccatagliata et al. 2009; Nilsson et al. 2010).

While the (sub-)mm observations as well as the pre-*Herschel* far-infrared observations are limited only by their sensitivity, mid-infrared observations and parts of the new *Herschel* far-infrared observations of the closest stars are sensitive enough to be limited by the photometric calibration. Furthermore, deep *Herschel* observations are affected by background confusion (e.g., Eiroa et al., in prep.). This suggests that spatially unresolved far-infrared observations of debris disks are now close to a quality that cannot be further increased by increasing the sensitivity of the instruments only.

3.1.3 Mid-infrared spectroscopy

Complementing the broad band photometry of debris disks described above, mid-infrared spectroscopy aboard ISO and *Spitzer* has proven to be successful to determine the properties of debris disks that significantly emit in this wavelength range (Beichman et al. 2005*a*; Backman et al. 2009; Weinberger et al. 2011). The presence and shape of spectral features helps to constrain the chemical composition of the dust as well as the dust grain size (Sect. 2.3). A broad wavelength coverage of the spectra allows to mitigate some of the deficiencies of pure photometry described above. The spectrum is often able to trace simultaneously a wavelength region where the flux from the system is mostly photospheric (determined by the slope of the spectrum) and a region where excess can be detected. If one only wants to detect debris disks, this will take the need for very accurate absolute photometry and prediction of the stellar photosphere. The determination of the shape of the SED in this wavelength range strongly constrains models of the disks (e.g., Backman et al. 2009; Ertel et al. 2011; Chapt. 6 of the present work).

3.1.4 Spatially resolved direct imaging of thermal re-emission

The above techniques do not allow to obtain direct information about the spatial distribution of the dust. The spectral energy distribution – measured through broad band photometry or spectroscopy – can give only limited, degenerate information about the radial dust distribution through the temperature information carried. Spatially resolved

direct imaging of the radial distribution of the dust can help to mitigate these degeneracies. This can be done in thermal re-emission for very extended (nearby) debris disks using large ground based single dish telescopes in the (sub-)mm (e.g., Greaves et al. 1998, 2005). The most extended disks could also be resolved with past mid-infrared to far-infrared space-based facilities (e.g., Stapelfeldt et al. 2004; Su et al. 2005; Backman et al. 2009). With its large 3.5 m primary mirror, *Herschel* allows one to image debris disks with unprecedented spatial resolution in the far-infrared (Liseau et al. 2010; Marshall et al. 2011).

3.1.5 Sub-millimeter to millimeter interferometry

In contrast to direct imaging which measures the spatial intensity distribution $I(x, y)$, interferometry samples the Fourier transformation $\hat{I}(u, v)$ of this distribution, i.e., the distribution of spatial frequencies. A detailed description of (sub-)mm interferometry has been presented by Haniff (2007). The u-v-plane is sampled in a discrete way by combinations of two telescopes with different distances (base lines) and relative positions. Only a complete coverage of the u-v-plane allows unambiguous image reconstruction. The less dense the sampling is the more artifacts are expected. A dense sampling can be reached by a large number of telescopes as well as by using different relative positions of the telescopes (e.g., by placing the telescopes at different positions or observing at different times with the object at different positions in the sky). While the first possibility allows efficient observations, but requires a large number of basically identical telescopes, the latter is limited by the total time one wants to spend on the observations of one target. A significant improvement is expected by the Atacama Large Millimeter/submillimeter Array (ALMA) that recently started Early Science observations (Chapts. 9, 10, and 11 of the present work). Once completed, it will provide a total of 50 12-m antennas with variable relative positions and a maximum base line of ≈ 16 km. It is expected to detect and spatially resolve most of the known (sub-)mm bright debris disks.

3.1.6 Direct imaging of scattered light

Scattering of stellar radiation dominates the dust emission at short wavelengths, where the thermal re-emission is negligible. This offers observational opportunities at optical to near-infrared wavelengths. Due to the short observing wavelength, one can achieve much higher spatial resolution compared to direct imaging of the thermal re-emission of the dust. On the other hand, only a small fraction of the stellar light is scattered by the dust resulting in the fact that the stellar PSF dominates the whole observations and has to be properly suppressed and/or subtracted.

The most common way to suppress the stellar PSF is to block the stellar light using a coronagraph and to subtract the residuals by subtraction of the PSF measured on a reference star (PSF subtraction; e.g., Ardila et al. 2004; Schneider et al. 2005; Boccaletti et al. 2009). The consequence is an inner region of the system ($1''$ to $2''$ in radius) made useless by the coronagraph and imperfect PSF subtraction. A detailed review of challenges and techniques of optical to near-infrared high contrast observation has been presented

by Oppenheimer & Hinkley (2009). Despite the observational challenges described above, scattered light imaging of bright debris disks gives important insights into the spatial distribution of the dust due to the high spatial resolution.

3.2 DUst around NEarby Stars (DUNES)

Parts of this work (Sect. 5.2.2, Chapts. 7 and 8) have been carried out in the context of the *Herschel* Open Time Key Program DUNES (Eiroa et al. 2010; Liseau et al. 2010; Marshall et al. 2011). It is a deep, systematic survey for cold, faint debris disks that will reveal the fractional incidence of planetesimal systems in the solar neighborhood. DUNES aims at detecting (and in part spatially resolving) debris disks with fractional luminosities similar to the Edgeworth-Kuiper Belt level ($L_{\rm d}/L_\star = 10^{-7}$ to 10^{-6}; Stern 1996; Vitense et al. 2010) around a volume limited sample ($d \leq 20\,{\rm pc}$) of Sun-like stars (spectral types F, G, and K). Some additional sources at $20\,{\rm pc} < d \leq 25\,{\rm pc}$ are included because of their known excesses previously detected with *Spitzer*, or because they are known exoplanet host stars. This results in a total of 133 stars observed. The stars surveyed cover ages of 0.1 Gyr to 10 Gyr. Due to the unprecedented sensitivity of *Herschel* and the ability to observe at longer wavelengths (with reasonable sensitivity) compared to earlier missions, this survey is able to extend the sample of known debris disks towards disks of lower mass (lower fractional luminosity) and towards colder disks (emitting at longer wavelengths). The DUNES sample will be combined with the sample of DEBRIS (Disc Emission via a Bias-free Reconnaissance in the Infrared/Submillimetre, Matthews et al. 2010), another debris disk survey on *Herschel* which has complementary science goals to those of DUNES. This will result in an unbiased sample of debris disks around stars with masses ranging from $0.2\,M_\odot$ to $2\,M_\odot$ (spectral types M to A).

The observations are carried out using *Herschel*/PACS (Photodetector Array Camera and Spectrometer; Poglitsch et al. 2010) at 100 μm and 160 μm. Additional observations using *Herschel*/PACS at 70 μm and *Herschel*/SPIRE (Spectral and Photometric Image Receiver; Griffin et al. 2008) at 250 μm, 350 μm, and 500 μm are carried out for a subset of the sample, mostly as follow-up observations of detected debris disks.

3.3 A "typical" debris disk

The observational results on debris disks obtained in the last three decades and the results based on them are summarized in this section. This is done by drawing the image of a "typical" debris disk. The probability that such a disk is found around a Sun-like star is at least 30% in the solar neighbourhood (Eiroa et al., in prep.) with increasing probability from late type towards early type stars (Beichman et al. 2006; Su et al. 2006; Gautier et al. 2007; Trilling et al. 2008). It has a dust mass of $\sim 10^{-8}\,{\rm M}_\odot$, varying by several orders of magnitude and decreasing with the age of the system (Wyatt 2008). The dust is produced in a (more or less broad) ring of planetesimals (birth ring scenario, e.g., Krivov 2010). It

is distributed in a broad disk at a distance of several tens of AU from the star. The radial dust density distribution can be nearly arbitrary, including an outwards increasing density (Löhne et al. 2011; Chapt. 8 of the present work). Clumpy structures or asymmetries may be present in the disk (e.g., Greaves et al. 1998, 2005; Corder et al. 2009). Additional dust with significantly lower particle density can be found in the inner regions around the star ranging from the inner edge of the main disk to the sublimation radius of the dust (Absil et al. 2008, 2009; Backman et al. 2009; Ertel et al. 2011; Chapts. 6 and 12 of the present work). The vertical extent of the disk is narrow (few AU to few tens of AU, Fitzgerald et al. 2007; Golimowski et al. 2006; Thébault 2009). The chemical composition of the dust is similar to that of the dust in the interstellar medium, mainly consisting of crystalline and amorphous silicates, but also of carbon and water ice. The dust grain size distribution follows in good approximation a power-law distribution from grains of the blow-out size (or a few times larger, e.g., Thébault et al. 2003; Krivov et al. 2006; Thébault & Augereau 2007; Krivov et al. 2008; Chapt. 6 of the present work) to very large grains and up to the planetesimals producing the dust through collisions. A more detailed view on the size distribution may yield a wavy distribution overlayed on the over-all power-law size distribution (Thébault et al. 2003; Krivov et al. 2006; Thébault & Augereau 2007; Krivov et al. 2008).

4 Modeling of debris disks

While observations of debris disks give us a raw view of the disk properties and allow us to draw statistical conclusions from large samples of debris disks, only detailed modeling can result in a complete image and comprehensive understanding of single systems. The information one is interested in and one may want to better constrain through modeling than it would be possible through observations alone are:

- The spatial distribution of the dust,
- The chemical composition and physical shape of the dust grains,
- The grain size distribution, the evolutionary/collisional connection between small and large grains, and the dynamics, collisional state, and origin of the dust,
- The spatial distribution and dynamical and collisional state of the planetesimals that are expected to produce the dust through collisions,
- The properties of possible planets in the system and the dynamical and evolutionary state of the planetary/planetesimal system.

Some of these information are only accessible in a limited way through observations (e.g., due to limited spatial resolution), while others are not even expected to produce observable features in the disk directly and are, thus, only accessible through detailed, physical modeling. As can be seen from the mere quantity of the above information, the complexity of models can be enormous. Furthermore, the information provided by single data sets is limited. In particular, studying the SED of the dust grains alone usually provides only weak, ambiguous constraints to their properties such as chemical composition, grain size, and spatial distribution (Wolf & Hillenbrand 2003). For example, the location of the inner edge of the dust distribution is strongly degenerate with the lower limit of the grain size distribution. Hence, efficient ways of modeling and of comparing the models to multiple data sets have to be found to break these degeneracies. To extract the most complete set of information about a debris disk, there are a number of complementary modeling approaches the most important of which are summarized in the following. In the last section of this chapter, an approximation of the flux neglected by adopting an upper cut-off size of the dust is given. It is shown that this common simplification leads to significant errors and solutions for this problem are suggested.

4.1 Analytical model fitting

An important method to sharpen our view of a debris disk beyond the possibilities of observations alone is analytical modeling (e.g., Augereau et al. 1999; Wolf & Hillenbrand 2003; Backman et al. 2009; Ertel et al. 2011; Chapts. 6, 7 and 8 of the present work). It employs analytical functions (e.g., parameterized power-law distributions) to describe the disk properties such as radial distribution of the dust or grain size distribution to create simulated observations of the disk. The parameters of these functions can be varied and the simulated observations can be compared to real observations. The use of power-law distributions is particularly motivated by analytical solutions for the radial dust distribution and the grain size distribution under certain simplifications (Briggs 1962; Dohnanyi 1969). This has a number of advantages:

- Simulated observations can be computed from the models very quickly due to their analytical nature, which allows the exploration of a large, complex parameter space.
- Arbitrary data can be simulated from the models, which allows simultaneous multi-wavelength fitting to SED and spatially resolved data to break modeling degeneracies produced by single data sets (e.g., Chapt. 6 of the present work).
- No or very limited constraints are necessary on the expected or unknown physical processes taking place in the system, since they are not required in the simple analytic models.

These advantages are to the cost of the fact that the models derived have no direct physical value. While they help us to sharpen our image of the system, any physical conclusions on the processes taking place require further interpretation of the modeling results.

4.2 Collisional modeling

In this statistical approach, the dust properties are simulated "from the source" (Wyatt 2003, 2006; Löhne et al. 2008; Stark & Kuchner 2009; Krivov 2010). This means that initial distribution, dynamical state, and physical properties (i.e., material strength) of planetesimals are parameterized and collisions between them are modeled statistically. If one finds a configuration reproducing the whole set of observations, one will be able to draw conclusions on the possible processes taking place from the modeling results directly. However, this goes to the cost of computational speed. No real fitting or exploration of a large parameter space is possible. Thus, this approach is better suited to theoretical and parameter studies (Löhne et al. 2008), although it has also been proven to be successful in modeling of real sources (Löhne et al. 2011).

4.3 Dynamical modeling

An approach to access the spatial distribution of dust and planetesimals, in particular under the influence of planets present, is dynamical modeling (e.g., Kenyon & Bromley 2001; Rodmann 2006; Chapt. 10 of the present work). Performing N-body simulations and considering the effects of Poynting-Robertson drag and radiation pressure blow-out, one can model the spatial distribution of dust grains of different size to produce images of this distribution. In this way one can study the structures produced in debris disks by planet-disk interaction and constrain the masses and orbital elements of possible planets in systems with observed structures (Chapt. 10 of the present work). Like collisional modeling, such simulations are limited by the long simulation times and the limited computational power of present computers.

4.4 The impact of an upper cut-off grain size

As the dust in debris disks is produced in a collisional cascade from planetesimal-sized objects, all sizes from microns to meters (and larger) should be present. However, for modeling of the thermal reemission of the dust (independent from the approach used to simulate the radial and grain size distribution), usually an upper cut-off grain size of a few millimeters is used. The reasons are: *(1)* Mie calculations of very large grains (large size parameters, Eq. 2.2) are very time consuming. *(2)* It is usually assumed that the large grains have negligible effect on the thermal emission due to their low abundance in a sufficiently steep size distribution (i.e., a power-law with an exponent of ~ -3.5). In this section, it will be shown that this assumption results in large errors in the order of $> 10\%$ even at short far-infrared wavelengths. This may significantly affect the results in a systematic way when fitting a thermal reemission model to observations.

To estimate the effect of neglecting large grains, the absorption efficiency $Q_\lambda^{\mathrm{abs}}(a)$ can be parameterized. For typical chemical compositions like astronomical silicate, $Q_\lambda^{\mathrm{abs}}(a)$ follows a well determined behaviour (Fig. 4.1). It approximately equals one for $\lambda \leq 2\pi a$. At this wavelength, $Q_\lambda^{\mathrm{abs}}(a)$ exhibits a sharp break and drops towards longer wavelengths with $\sim \lambda^{-2}$. Thus, $Q_\lambda^{\mathrm{abs}}(a)$ can be parameterized as follows:

$$Q_\lambda^{\mathrm{abs}}(a) = \begin{cases} 1 & \forall\ \lambda \leq 2\pi a \\ \left(\frac{2\pi a}{\lambda}\right)^2 & \forall\ \lambda > 2\pi a \end{cases} . \tag{4.1}$$

In the following, a_{min} denotes the real lower grain size (e.g., the blow-out size in the system), a_{max} denotes the real upper grain size (e.g., ∞), a_{cut} denotes the adopted upper cut-off size (e.g., 1 mm), and $a_{\mathrm{crit}} = \lambda/2\pi$, i.e., the size at which $Q_\lambda^{\mathrm{abs}}(a)$ exhibits the break for a given wavelength λ. Furthermore, $a_{\mathrm{cut}} > a_{\mathrm{crit}}$ is assumed.

Following Eq. 2.6, one can compute the ratio V_λ between the power emitted by grains larger than a_{cut} and the power emitted by all grains (i.e., the fraction of power neglected

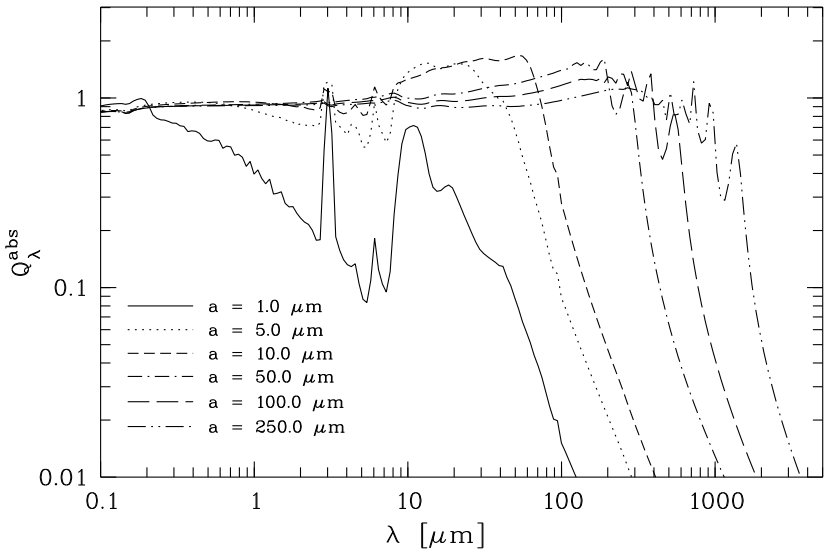

Fig. 4.1: Absorption efficiency Q_λ^{abs} of astronomical silicate (Draine 2003) of different grain radii a.

when adopting any a_{cut}):

$$V_\lambda = \frac{\int_{a_{\mathrm{cut}}}^{a_{\mathrm{max}}} n(a) W_\lambda^{\mathrm{emi}}\, da}{\int_{a_{\mathrm{min}}}^{a_{\mathrm{max}}} n(a) W_\lambda^{\mathrm{emi}}\, da}, \tag{4.2}$$

where $n(a)$ describes the relative abundance of grains of different size. Assuming all grains at a given distance form the star to have the same temperature (which is a valid simplification, since the relevant grain sizes are in the order of few tens of micron and larger and the temperature variations with grain size are small for these grains), assuming a power-law distribution $dn(a) \propto a^\gamma\, da$ of the grain size, and using the parameterization in Eq. 4.1, one can compute V to

$$\begin{aligned} V_\lambda &= \frac{\int_{a_{\mathrm{cut}}}^{a_{\mathrm{max}}} a^{\gamma+2}\, da}{(2\pi/\lambda)^2 \int_{a_{\mathrm{min}}}^{a_{\mathrm{crit}}} a^{\gamma+4}\, da + \int_{a_{\mathrm{crit}}}^{a_{\mathrm{max}}} a^{\gamma+2}\, da} \\ &= \frac{\frac{1}{\gamma+3}\left(a_{\mathrm{max}}^{\gamma+3} - a_{\mathrm{cut}}^{\gamma+3}\right)}{(2\pi/\lambda)^2 \frac{1}{\gamma+5}\left(a_{\mathrm{crit}}^{\gamma+5} - a_{\mathrm{min}}^{\gamma+5}\right) + \frac{1}{\gamma+3}\left(a_{\mathrm{max}}^{\gamma+3} - a_{\mathrm{crit}}^{\gamma+3}\right)}. \end{aligned} \tag{4.3}$$

For $\gamma = -3.5$ this results in

$$V_\lambda = \frac{a_{\mathrm{cut}}^{-0.5} - a_{\mathrm{max}}^{-0.5}}{\frac{4\pi^2}{3\lambda^2}\left(a_{\mathrm{crit}}^{1.5} - a_{\mathrm{min}}^{1.5}\right) + a_{\mathrm{crit}}^{-0.5} - a_{\mathrm{max}}^{-0.5}}. \tag{4.4}$$

Neglecting the small grains ($a < a_{\mathrm{crit}}$) the emission of which falls off with λ^{-2}, V_λ simplifies to

$$V_\lambda \approx \frac{a_{\mathrm{cut}}^{-0.5} - a_{\mathrm{max}}^{-0.5}}{a_{\mathrm{crit}}^{-0.5} - a_{\mathrm{max}}^{-0.5}} \tag{4.5}$$

Table 4.1: Ratio V_λ of neglected to total flux of a system using an upper cut-off grain size for selected wavelengths, and upper cut-off grain sizes for $a_{\max} \to \infty$ and $a_{\min} = 0.5\,\mu$m.

λ \ $a_{\rm cut}$	1 mm	2 mm	3 mm	1 cm
100 μm	9.5	6.7	5.5	3.0
350 μm	17.7	12.5	10.2	5.6
850 μm	27.6	19.5	15.9	8.7
1300 μm	34.1	24.1	19.7	10.8
3100 μm	52.7	37.2	30.4	16.6

and with $a_{\max} \to \infty$ to

$$V_\lambda \approx \sqrt{\frac{a_{\rm crit}}{a_{\rm cut}}}. \tag{4.6}$$

Values of V_λ for different wavelengths and upper cut-off grain sizes are given in Table 4.1 for $a_{\max} \to \infty$ and $a_{\min} = 0.5\,\mu$m (i.e., the typical blow-out size around a solar-type star). For reasonable values of λ and $a_{\rm cut}$, the error amounts up to 30%. It needs to be evaluated in the near future how significant this is compared to photometric uncertainties, simplifications of the models and modeling uncertainties. Since in particular ALMA will significantly decrease the photometric uncertainties of available data in the (sub-)mm and will provide spatially resolved data breaking modeling degeneracies, the problem described above will gain significance in the near future.

To avoid the simplification of an upper cut-off size without the need of time consuming Mie calculations, one can approximate the very large grains ($a > a_{\rm cut}$) through black body grains ($Q_\lambda^{\rm abs}(a) = 1$). In a logarithmical sampling of the size distribution, adding a few size bins should allow one to sufficiently increase the range of sizes covered. Alternatively, Eq. 4.3 gives a relation to correct for the neglected flux in already computed SEDs (i.e., old models or on the fly correction during model fitting) by multiplying the model SED by a wavelength dependent factor $(1 - V_\lambda)^{-1}$.

5 The tool box used in this work

In the previous chapter, the different approaches to model debris disks have been summarized. In the present work, new tools have been developed for the interpretation of results from the dynamical approach and for analytical modeling and model fitting to raise to the challenges of the available high quality data to be modeled. Furthermore, a number of tools have been used that are available through collaborations. These codes are described in the present chapter.

5.1 Available tools

In this section, the tools available prior to the present work are described briefly. For a detailed description of these tools, see the corresponding publications.

To calculate optical properties of dust grains like $Q_\lambda^{\rm abs}(a)$ or $Q_\lambda^{\rm sca}(a)$ from Mie theory (Sect. 2.1.1), the code `miex` (Wolf & Voshchinnikov 2004) is used. It is designed to handle large size parameters. The code is used as stand-alone version (with modified output) for several applications. Furthermore, it is included in other tools directly to use it most efficiently.

The Debris Disk Radiative Transfer Simulation Tool (`DDS`; Wolf & Hillenbrand 2005) is used in the context of the present work to simulate SEDs of debris disks and for qualitative comparison of the simulated data with observations.

`MODUST` (Rodmann 2006) is an N-body code to accurately follow the orbits of a large number of massless test particles under the influence of the gravitation and radiation of a central star and the gravitation of one or more planets. The orbits of the dust particles as well as of the planets are integrated using a fourth-order Hermite scheme (Makino 1991; Makino & Aarseth 1992). The code is used in the context of the present work to model the structures induced in debris disks due to planet-disk interaction.

5.2 Newly developed tools

In the following, the codes that have been developed in the context of the present work are described. A detailed description of the input and output of each tool is available with the source code.

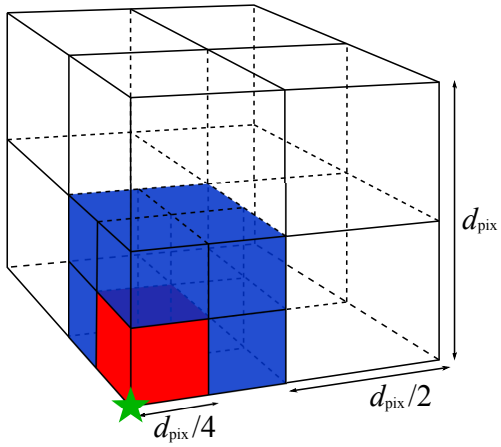

Fig. 5.1: Sketch to illustrate the dynamical sampling in `debris`. In this example, only the edge marked by the green star does not satisfy the termination criteria described in Sect. 5.2.1. The original, three-dimensional pixel (with size d_{pix}) is shown after two iterations performed. In the second iteration, only the blue sub-pixel is segmented and in the next iteration, only the red one will be segmented.

5.2.1 `debris` – Efficient calculations of high accuracy images from analytical disk models

Overview

The tool `debris` has been created in the context of this work to compute images (i.e., a Cartesian grid of pixels each of which has been assigned an intensity value) of analytically defined disk models with high accuracy and with high efficiency. To accurately sample on such a grid an analytical disk model usually defined in polar coordinates bears a number of challenges:

- In general, a low sampling rate means a low spatial resolution, while a high sampling rate means large computational effort (three-dimensional structure to be sampled).
- The spatial resolution has to be high to accurately compute the pixel values in regions where the intensity distribution is changing significantly on small spatial scales (temperature of the dust rapidly changing with radial distance or sharp break of the analytical density distribution like inner disk edge).
- Often, a rather low spatial resolution is sufficient to compare the modeled data with observations of similar resolution.

To raise to these challenges, a dynamic sampling is used in `debris` that allows high sampling rates without increasing the over-all spatial resolution (pixel number). The thermal reemission as well as the stellar light scattered by the star is computed following Eqs. 2.5, 2.6, 2.9, and 2.13. The optical properties of the dust are computed using `miex`, which

is directly included in `debris`. Radial dust distribution and grain size distribution are parameterized using analytical functions.

Dynamic sampling

The dust emission is sampled on a three-dimensional, Cartesian grid. The initial spatial resolution (pixel size), a maximum temperature difference within one pixel, and a maximum number of segmentations of one three-dimensional pixel are specified as input parameters. The pixel is divided iteratively in 8 sub-pixels covering the original pixel (Fig. 5.1) until one of the following criteria is met:

- The maximum temperature difference at the edges of one pixel is smaller than the maximum difference specified to be acceptable and the edges of the pixel are all inside or all outside the region where the density distribution is defined.
- The maximum number of segmentations (iterations) of one pixel has been performed.

The scattered and re-emitted flux at the center of each sub-pixel for which the iteration has stopped is computed and summed over all sub-pixels corresponding to one pixel. To compute an image, the three-dimensional spatial flux distribution is integrated (summed) along the line of sight.

Tests

The tool has passed a number of tests that are described in the following. Errors in all tests are in the order of 0.5% to 2% for reasonable sampling parameters. The typical parameter space relevant for debris disks has been explored (r of few AU to few 100 AU, a of few 100 nm to few mm, T of few K to several 100 K).

- The radial temperature distribution as well as the SED for different stellar emission spectra (black body and model spectra) and disk models have been tested against the `DDS`.
- The spatially resolved thermal emission of the disk has been computed for single grain sizes and a face-on oriented, narrow disks following Eq. 2.6. The total thermal emission of the disk for different inclinations has to be the same.
- The total scattered light emission for a radially thin, spherical shell around the star composed of grains of one single size has been computed by hand following Eq. 2.10 (in this case, the angular dependence of the scattering matrix averages to 1). The results for different viewing angles have to be the same.
- The angle dependent, spatially resolved scattered light emission of the disk has been computed for single grain sizes and an arbitrarily inclined (but not edge-on), narrow disk following Eqs. 2.13 (total flux) and 2.14 (polarized fraction)

5.2.2 SAnD – Model fitting to spatially resolved data of thermal reemission using simulated annealing

Overview

The **S**imulated **An**nealing **D**ebris Disk Fitting Tool (SAnD) has been created in the context of this work to fit spatially resolved thermal reemission data of debris disks obtained by *Herschel*/DUNES (Sect. 3.2). It allows one to fit SED data and radial profiles simultaneously using a simulated annealing approach (Press et al. 1992) on a grid of possible values in the parameter space. The thermal reemission of the dust is computed following Eqs. 2.5, 2.6, and 2.9. An analytical model is used for the radial density distribution (azimuthally symmetrical) as well as for the grain size distribution. Radial profiles are extracted along the major and/or minor axis of resolved images simulated with sufficient resolution, convolved with the telescope PSF, and scaled by a factor x_i to minimize the $\chi^2_{i,\mathrm{prof}}$ (Eq. 5.3). Due to the scaling, only the shape of the radial profiles is fitted. Otherwise, flux calibration uncertainties that have to be considered only once per wavelength would be included for each data point in the radial profiles. Furthermore, deficits of the models to reproduce the absolute flux at wavelengths at which also radial profiles are fitted (e.g., due to uncertainties in the optical properties of the dust) would be over-weighted. Simulated and observed SED and profiles are compared using the following reduced χ^2:

$$\chi^2_{\mathrm{red}} = \frac{N_{\mathrm{tot}} \left(\sum_{i=0}^{M} w_i\right)^{-1}}{N_{\mathrm{tot}} - N_{\mathrm{free}}} \left(w_0 \frac{\chi^2_{\mathrm{SED}}}{N_0} + \sum_{i=1}^{M} w_i \frac{\chi^2_{i,\mathrm{prof}}}{N_{i,1} + N_{i,2}} \right), \tag{5.1}$$

$$\text{with} \quad \chi^2_{\mathrm{SED}} = \sum_{k=1}^{N_0} \left(\frac{F_k - \tilde{F}_k}{\sigma_k} \right)^2, \tag{5.2}$$

$$\text{and} \quad \chi^2_{i,\mathrm{prof}} = \sum_{j=1}^{2} \sum_{k=1}^{N_{i,j}} \left(\frac{x_i S_{i,j,k} - \tilde{S}_{i,j,k}}{\sigma_{i,j,k}} \right)^2, \tag{5.3}$$

where $i = 0$ refers to the SED and $i \geq 1$ refers to the profiles, $j = 1$ to major axis and $j = 2$ to minor axis of a profile. In Eqs. 5.1 to 5.3, the notations used are:

- M, N_0 – number of images, number of SED data points,
- $N_{i,1}$, $N_{i,2}$ – number of profile data points along major axis (1) and minor axis (2),
- N_{tot}, N_{free} – total number of data points $N_0 + \sum_{i=1}^{M} \sum_{j=1}^{2} N_{i,j}$, number of free parameters,
- F_k, $\tilde{F}_k$ – modeled and observed SED,
- $S_{i,j,k}$, $\tilde{S}_{i,j,k}$ – modeled and observed surface brightness profiles,
- σ_k, $\sigma_{i,j,k}$ – uncertainties (SED and profiles),
- x_i – surface brightness profile scaling factor,

- w_i – weight, used to weight profiles among each other and against the SED.

The simulated annealing approach

The simulated annealing approach enables one to handle a very large, high dimensional parameter space without sampling the whole range of parameters. Therefore, a random walk on the grid of possible parameters is performed. A Boltzmann distribution of the probability p to go a certain step is used:

$$p = \begin{cases} 1 & \forall\ \chi_0^2 \geq \chi_1^2 \text{ (fit becomes better)} \\ \exp\left[-\frac{\chi_1^2 - \chi_0^2}{T}\right] & \forall\ \chi_0^2 < \chi_1^2 \text{ (fit becomes worse)} \end{cases}, \tag{5.4}$$

where χ_1^2 belongs to the actual and χ_0^2 to the previous step. T is a parameter comparable to the temperature of an annealing physical system and controls the ability to reach areas in the parameter space that give worse fits. T is chosen to be a large value at the beginning of a run and is lowered with each successful step of the random walk. The width of each step is chosen from a probability distribution that prefers short steps. The probability to go long steps is lowered with each successful step. With this approach, the code is able to reach each position in the parameter space, but prefers regions with low χ^2. The run stops, if a position in the parameter space with the following properties is reached:

- The code was not able to leave the position after computing 500 further models.
- The actual χ^2 is lower than or equal to the best reached χ^2 during the whole run.
- The actual χ^2 is lower than or equal to a maximum χ^2 specified.

A set of model parameters that satisfies all of these conditions is considered as likely a global fit. If only the first, but not all of these termination criteria are satisfied, the value of T is increased and the random walk is continued. As a feature of the simulated annealing approach, the time it takes to find a best-fit does not vary much with the number of free parameters or the total size of the parameter space to be searched, but depends on the shape of the χ^2 distribution. Weak variations of the χ^2 over a broad range of the parameters as well as very degenerate fitting problems require more time (i.e., more models to be computed).

Error estimates are done in the context of the simulated annealing approach by starting a new random walk at the best-fit position with a fixed value of T (usually 10% of the best-fit χ^2) and counting how often each value of a parameter is reached. This way, the projection of the probability distribution of the random walk (Eq. 5.4) on the axis of each parameter is sampled. With the knowledge of the value of T, one can then compute the probability distribution

$$p' = \exp\left[-\left(\chi^2 - \chi^2_{\text{best}}\right)\right] \tag{5.5}$$

and corresponding levels of confidence.

Tests

SAnD has been tested successfully through its output and performance as follows:

- The images and SEDs produced have been compared to results produced by DDS and debris. Profiles have been compared to results obtained with debris. The results are consistent within an uncertainty of 5%.
- The profiles and SEDs, the found best-fit parameters, and the χ^2 values of fits performed in the context of *Herschel*/DUNES have been compared to those obtained with the tool GRaTeR (Augereau et al. 1999) that performs a grid search in the parameter space. These results are consistent within the uncertainties of the fitted parameters computed by SAnD (see Chapt. 8 for an example).

5.2.3 MODIM – Creating images form the data produced by MODUST.

Overview

The **MOD**UST **IM**ager (MODIM) has been developed to simulate images and SEDs in scattered light and thermal reemission of spatial dust distributions produced by MODUST. Like in debris, the thermal reemission as well as the stellar light scattered by the dust is computed following Eqs. 2.5, 2.6, 2.9, and 2.13 and the optical properties of the dust are computed using miex included directly in MODIM. Because each particle is used directly to compute its emission, the sampling is given by the position of the particles and no dynamical sampling like in debris is necessary. To create images from the dust distributions derived from MODUST, the thermal reemission and the scattered stellar light at a set of observing wavelengths is computed for each dust particle. The emitted and scattered flux on the line of sight is then summed for all particles in one pixel of the final image. This can be done for arbitrary orientations of the disk (assuming an optically thin debris disk).

Tests

MODIM has been tested successfully through comparison of the results to results produced by debris for comparable dust distributions (azimuthally symmetrical disk with a radial density distribution following a power-law). The same parameter space as for debris has been explored. Systematic deviations are in the order of few percent.

6 Multi-wavelength modeling of the spatially resolved debris disk of HD 107146

In the previous chapters, the stage for detailed modeling of debris disks has been set by introducing the physics necessary, describing the challenges, uncertainties, and the potential of the data available, and by introducing the tools developed to raise to these challenges. In the next three chapters, this is applied to the modeling of high quality data of several debris disks, starting in the present chapter with the disk around HD 107146.

HD 107146 is a well studied system around a young, solar-type star (G2 V), 28.5 ± 0.7 pc from the Sun (Perryman et al. 1997). The stellar luminosity and effective temperature are $1.1\,L_\odot$ (Ardila et al. 2004) and 5924 K, respectively. Its estimated age ranges from 80 to 320 Myr (Williams et al. 2004; Moór et al. 2006; Roccatagliata et al. 2009). HD 107146 has been spatially resolved in optical to near-infrared scattered light with the *Hubble* Space Telescope (HST/ASC, Ardila et al. 2004, 2005 and HST/NICMOS, Ertel et al. 2011) and at (sub-)mm wavelengths with CARMA (Combined Array for Research in Millimeter-Wave Astronomy; Corder et al. 2009) and the SMA (Submillimeter Array; Hughes et al. 2011). It has been studied in the context of the *Spitzer* Legacy Science Program FEPS (Formation and Evolution of Planetary Systems; Meyer et al. 2006) resulting in a broad variety of photometric measurements as well as spectra of the system (e.g., Hillenbrand et al. 2008). Further broad band photometric measurements are available in the literature (Table 6.1). The debris disk around HD 107146 is remarkable in many respects. Due to its near to face-on orientation ($25° \pm 5°$ from face-on) and its large inner hole of ~ 60 AU, corresponding to $2''$ (Ardila et al. 2004), it can be imaged using coronagraphy without masking large parts of the disk. Its particularly high scattered light surface brightness enables high SNR imaging (Ardila et al. 2004). Furthermore, the radial surface brightness distribution can be observed without strong projection effects which would occur in an edge-on case.

In the context of the present work, combined multi-wavelength modeling of the system has been carried out, mostly based on the HST/ACS data, the SED data and the CARMA 1.3 mm data. An analytical modeling approach has been used. The work presented in this chapter has been published by Ertel et al. (2011). The HST/NICMOS observations in the F110W filter ($\lambda_c = 1.1\,\mu$m) presented there and included in the modeling have been obtained as part of a larger circumstellar disk imaging survey (HST GO/10177; PI: Schneider[1]) and have been provided for the modeling and for being published along with

[1] http://nicmosis.as.arizona.edu:8000/POSTERS/AAS_JAN_2006_GO10177.pdf

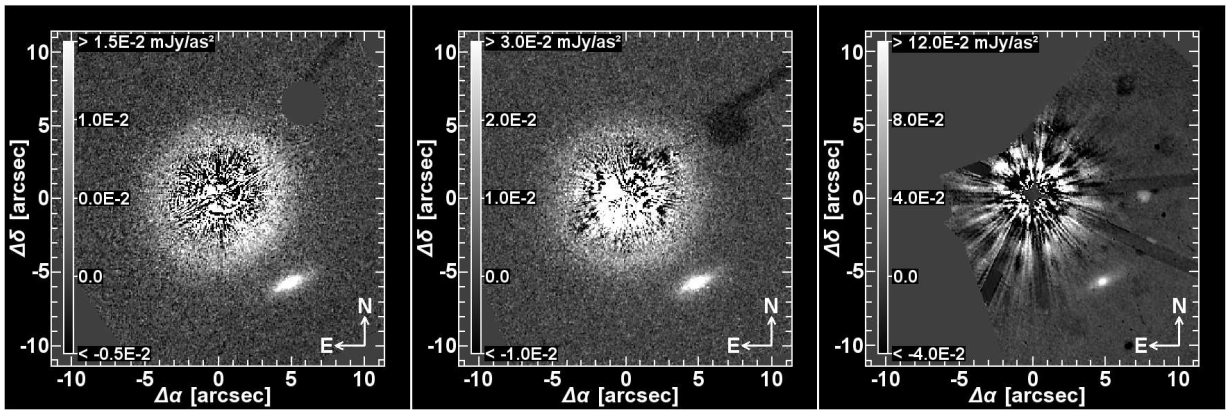

Fig. 6.1: HST/ACS images at 0.6 μm (left) and at 0.8 μm (center) and the HST/NICMOS image at 1.1 μm (right). The HST/ACS images are rebinned to the HST/NICMOS pixel scale (0.″076 /pix). Note the different flux scales in mJy/as^2 and the fact that the stellar PSF residuals are heavily truncated in these scales. The object in the SW is a background galaxy.

the modeling results. For a description of these observations and the data obtained, see Ertel et al. (2011). The data and previous work on HD 107146 available from the literature have been summarized in this paper as well. In the present chapter, the modeling of the data and the interpretation of the results are described. A brief, qualitative discussion of the radial surface brightness distribution in the HST/ACS images to infer the general disk morphology is presented in Chapt. 6.1. Details about the applied model and the modeling approach developed – in particular, the order in which the available data are included and the information extracted in each step, respectively – can be found in Sect. 6.2. The results are presented and discussed in detail in Sect. 6.3. A possible extension of the model in order to account for modeling deficiency found is presented there as well. Conclusions are given in Sect. 6.4.

6.1 Qualitative discussion of the HST/ACS data

Ardila et al. (2004) resolved the disk using HST/ACS PSF subtracted coronagraphic observations in the F606W (broad V, $\lambda_c \approx 0.6\,\mu$m) and F814W (broad I, $\lambda_c \approx 0.8\,\mu$m) filters (Fig. 6.1). These data are the basis for the resolved modeling of the debris disk in the present work. A broad ring with maximum vertical optical depth at 130 AU from the star and an FWHM of 85 AU was found. They fitted elliptical isophotes to the disk images and derived an inclination of $25° \pm 5°$ from face-on with the disk minor axis at a celestial position angle (east of north) of $58° \pm 5°$. Ardila et al. (2004) also pointed out that the debris disk exhibits a surface brightness asymmetry in their ACS data, consistent with forward scattering of the star light by micron-sized dust grains given the inferred disk inclination.

The HST images are shown in Fig. 6.1. For the two HST/ACS images, Ardila et al.

Table 6.1: Photometric data of the HD 107146 system.

Wavelength [μm]	Flux [mJy]	Error ($1\,\sigma$) [mJy]	Reference
3.6	1711.3	36.7	1
4.5	1074.8	24.7	1
8.0	384.4	8.2	1
10.3	247.0	22.0	2
11.7	175.0	10.0	3
13.0	138.9	8.5	1
17.8	85.0	8.0	3
24.0	59.8	2.5	1
33.0	86.7	5.7	1
60.0	705.0	56.0	4
70.0	669.1	47.8	1
100.0	910.0	155.0	4
350.0	319.0	45.0	5
450.0	130.0	12.0	6
850.0	20.0	3.2	6
880.0	36.0	1.0	7
1300.0	10.4	1.5	5
3100.0	1.42	0.25	8

References. (1) Hillenbrand et al. (2008); (2) Metchev et al. (2004); (3) Williams et al. (2004); (4) Moór et al. (2006); (5) Corder et al. (2009); (6) Najita & Williams (2005); (7) Hughes et al. (2011) (8) Carpenter et al. (2005)

Notes. The 880 μm flux measurement has been published after the publication of the modeling presented in this chapter and is, thus, not considered in the present work. Uncertainties on this measurement do not take into account uncertainties from photometric calibration.

(2004) found that the artifacts from the PSF subtraction dominate the scattered light within $\approx 2''$ from the star. For a detailed discussion of the errors in these images, see Ardila et al. (2004). Sky-plane deprojected (i.e., if seen face-on and assuming $i = 25°$), azimuthally medianed radial surface brightness profiles of the disk are obtained from these two images following Weinberger et al. (1999). The results are shown in Fig. 6.2. In the F110W image large PSF subtraction residuals do not allow to derive a reliable profile.

The disk surface brightness derived from the two HST/ACS images decreases with increasing radius for $r > 130$ AU. A similar behaviour can also be seen qualitatively in the HST/NICMOS image. Within a radius of 130 AU from the star, the two HST/ACS surface brightness profiles flatten significantly. Inwards of ≈ 100 AU, the surface brightness obtained from the F814W image exhibits a steep increase. This is attributed to well char-

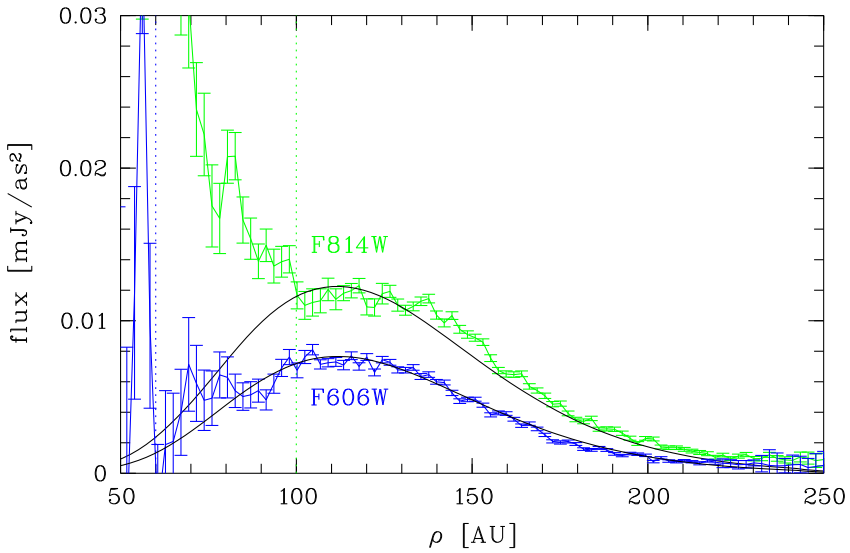

Fig. 6.2: Azimuthally medianed (one pixel wide annular zones) surface brightness profiles derived from the HST/ACS scattered light images after deprojection. Note that the F606W radial brightness profile is reliable only for $\rho > 60$ AU and the F814W profile is reliable only for $\rho > 100$ AU (dotted, vertical lines). An additional error of $\approx 5\%$ due to uncertainties in stellar PSF subtraction is not included in the plotted error bars. The black, solid lines represent the profiles derived from the final model of the disk (Sect. 6.2).

acterized technical artifacts and residuals from imperfect PSF subtraction in these data (ACS Instrument Handbook, Version 8.0, Boffi et al. 2007, Sects. 5.6.5, 6.2.9, and 9.3.2 and Version 10.0, Maybhate et al. 2010, Sect. 5.6.5). The (more reliable) F606W image exhibits a decrease with decreasing surface brightness in this region.

6.2 Combined multi-wavelength modeling of the data

For the analysis of the debris disk, simulated data produced with `debris` and `DDS` are compared to the available spectral energy distribution and multi-wavelength imaging data.

6.2.1 Model description

The stellar emission of HD 107146 is estimated by fitting a Kurucz (1969) model to the $0.4-2.5\,\mu$m stellar SED. The fit gives $T_{\rm eff} = 5924$ K and $\log g = 4.48$. A distance of the star from the Sun of 28.5 pc is adopted for the simulations. The derived uncertainties on the model parameters of the disk represent only the formal errors from the fitting. They do not include uncertainties in the distance of the star or the stellar properties. For the current simulations of the disk, an analytical, rotationally symmetrical density distribution $n(r)$

is employed. A single component model (no multi-ring structure) is employed to minimize the modeling degeneracies. There is no obvious evidence for a multi-ring structure at this stage of the work. A possible extension of this model is discussed in Sect. 6.3.2.

Employed density distribution

The simplest approach for the radial dust distribution is a power-law distribution $n(r) \propto r^{-\alpha}$ with inner radius $r_{\rm in}$ and outer radius $r_{\rm out}$. However, the above discussed surface brightness profiles are inconsistent with such a distribution (shallow decrease of the surface brightness inwards and outwards of the peak position). In the following, the employed density distribution is motivated and described.

A simple analytical function which closely reproduces the disk density profile using a minimum of free parameters is in demand. Such a distribution allows one simultaneous fitting of all parameters and can easily be compared to any distribution found in other studies. The actual distribution will be better described by a large number of physical parameters, reflecting all physical processes being responsible for it (e.g., the distribution of the planetesimals producing the dust, the effect of radiation pressure and Poynting-Robertson drag on the dust, masses and orbits of possible planets influencing the distribution by gravitational interaction). The empirical approximation found will at least be very similar to this distribution.

As described above, the observed surface brightness profile can be described as an increase followed by a decrease with increasing distance from the star. In addition, the position of the peak and the width of the distribution have to be parameterized. Not limiting on functions with (known) physical interpretation, one may consider the following candidate density distributions that might be able to reproduce the described behaviour of the surface brightness:

- A product of two power-laws, one with positive and one with negative exponent: In such a distribution, there is a strong correlation between the single parameters, making the fitting complicated and potentially resulting in very extreme, not physically interpretable values for all parameters.
- A product of a Gaussian distribution and a power-law: Due to the symmetrical Gaussian dominating the behaviour of the function, distributions with strong asymmetries around the peak distance can only be achieved by a very extreme index of the power-law part. Moreover, the parameters in this distribution are heavily correlated making fitting complicated.
- A product of a power-law and an exponential function (analogous to Planck's law): As shown below, the number of parameters and correlations between them can be reduced to a minimum for this distribution.

Based on the above discussion, the first two candidate distributions are rejected and the last one is adopted being most convenient for the purpose of the present study. From an

ad hoc point of view, the following distribution can be employed:

$$n'(r) = \begin{cases} 0 & \forall\ r < s \ \vee \ r < r_{\mathrm{sub}} \\ n'_0 \left(\frac{r-s}{r_0}\right)^{\alpha_1} \cdot \exp\left[-\alpha_2 \left(\frac{r-s}{r_0}\right)\right] & \forall\ r \geq s \ \wedge \ r \geq r_{\mathrm{sub}} \end{cases} . \tag{6.1}$$

In this equation, the quantity r_{sub} is the sublimation radius of the dust, r_0 is a scale length stretching the distribution along r, s is a characteristic length shifting the distribution along r, and α_1 and α_2 are parameters describing the slopes of the dust distribution in the inner and outer region, respectively. In this equation, one can express the quantity r_0 through the peak radius r_{p} of the distribution using the following condition:

$$\left.\frac{dn'(r)}{dr}\right|_{r=r_{\mathrm{p}}} = 0 \ ; \quad r_{\mathrm{p}} > s. \tag{6.2}$$

Defining a new density distribution $n(r)$ normalized to $n(r_{\mathrm{p}}) = 1$, one can eliminate the parameter α_2:

$$n(r) = \begin{cases} 0 & \forall\ r < s \ \vee \ r < r_{\mathrm{sub}} \\ n'_0 \left(\frac{r-s}{r_{\mathrm{p}}-s}\right)^{\alpha_1} \cdot \exp\left[\alpha_1 \left(1 - \frac{r-s}{r_{\mathrm{p}}-s}\right)\right] & \forall\ r \geq s \ \wedge \ r \geq r_{\mathrm{sub}} \end{cases} . \tag{6.3}$$

In the resulting density distribution, there are only three free parameters, s, r_{p}, and α_1, describing the inner increase and the outer decrease of the density as well as its width and peak position. It is important to note that the number of free parameters is still the same as for the power-law distribution (α, r_{in}, and r_{out}), despite an apparently much more complex shape of the distribution. Furthermore, only two parameters, s and α_1, are significantly correlated (see discussion in Sect. 6.2.3), while even in the case of a simple power-law α, r_{in}, and r_{out} are strongly correlated because of the poor fit to the observed data. Due to the particular shape of this distribution, there will usually be no need for an inner cut off r_{in}, which is essential for the power-law distribution.

An outer radius of the disk is usually needed to limit the extent of the disk for a power-law distribution that falls to negligible low values very slowly. The exponential decay reaches such values much earlier. If there is no real, physical break observed in the surface brightness profile (as it is the case for HD 107146), the outermost radius will just be larger than the sensitivity limited extent of the disk observed and is only used to limit the extent of the simulated images. Thus, in this study the outermost radius of the disk is set to $r_{\mathrm{out}} = 500\,\mathrm{AU}$. In contrast to the power-law distribution with the two cut-off radii, the new distribution is continuous and continuously differentiable. Due to its analytical character, it can easily be compared to any distribution found in other studies.

Additionally, a constant opening angle of the disk of 10° is employed to define the vertical extent of the disk. This simplification is chosen because of the nearly face-on orientation of the disk and allows one to compute the surface density distribution $\Sigma(\rho)$ from the radial density distribution $n(r)$ very easily:

$$\Sigma(\rho) \propto n(r = \rho) \cdot \rho. \tag{6.4}$$

Here, the quantity ρ is the distance from the star projected on the mid plane of the disk.

Employed dust grain properties

The only available data that could inform about the mineralogy of the dust grains is the *Spitzer* spectrum. Since this spectrum does not exhibit any significant features, astronomical silicate with a bulk density of $2.7\,\mathrm{g/cm^3}$ (Draine & Lee 1984; Weingartner & Draine 2001) is employed for the grain composition. The grain size distribution follows a power-law

$$dn(a) = \begin{cases} 0 & \forall\ a < a_{\min}\ \vee\ a > a_{\max} \\ n_0 a^{-\gamma}\ da & \text{else} \end{cases} . \tag{6.5}$$

It is assumed to be the same at all distances, so that one can compute the abundance $n(r, a)$ of a certain grain size at a certain position in the disk through

$$n(r, a) \propto n(r) \cdot n(a). \tag{6.6}$$

This assumption is necessary to limit the complexity of the employed model. As the disk is expected to be collision dominated (Sect. 6.2.3), one may assume that grain segregation due to Poynting-Robertson drag and radiation pressure has no significant effect.

In the grain size distribution employed, $a_{\min}$ and γ are free parameters, but $a_{\max}$ is fixed to 1 mm. Thus, the dust masses derived in this work represent the mass in particles smaller than 1 mm in radius only. The effect of the error introduced by an upper cut-off grain size (Sect. 4.4) is discussed with the other deficiencies of the modeling in Sect. 6.3.

6.2.2 General guideline

In order to efficiently break the modeling degeneracies, one has to understand the information that can be extracted from the observations and how to combine the ancillary data. In the following, the general guideline used to reduce the number of free parameters to a minimum in each step of the modeling is presented. The described approach leads to a complete set of model parameters for one unified model of the disk, consistent as far as possible with all data included.

Radial dust distribution from high resolution images

Having high resolution scattered light images of a radially symmetrical, optically thin debris disk seen near to face-on, the surface number density profile $\Sigma(\rho)$ of the disk is correlated with the face-on surface brightness profile $\varphi(\rho)$ as follows:

$$\Sigma(\rho) \propto \rho^2 \cdot \varphi(\rho) \cdot \Phi(90°). \tag{6.7}$$

Because the scattering efficiency at a scattering angle of 90°, $\Phi(90°)$, of the dust is unknown at this point, one cannot derive the absolute value of the surface density. For detailed fitting, one has to make reasonable assumptions on certain dust properties (in the present case $a_{\min}$ and γ, see Sect. 6.2.3 for the assumptions made in the present work). This is possible, because these assumptions primarily affect the total brightness of the disk and,

thus, the resulting disk mass, but not the shape of the disk. The radial density distribution $n(r)$ can be found using Eq. 6.4. Because scattered light images trace particularly the smallest grains, the validity of the derived density distribution for all grain sizes has to be verified. Furthermore, for coronagraphic scattered light images the inner parts of the disk are hidden by the coronagraph or heavily affected by the residuals of stellar PSF subtraction. Both the validity of the distribution for larger grain sizes as well as in the inner region can be verified including spatially resolved observations at thermal re-emission wavelengths, e.g., from mid-infrared to millimeter.

Dust properties from SED modeling

Once the spatial distribution of the dust is constrained from modeling the scattered light images[2], the main degeneracy in SED fitting is broken. One can now derive properties of the dust grains – in the present case the lower grain size and the exponent of the grain size distribution – from fitting the SED. One then has to go back to the scattered light images and confirm the results for the density distribution using these dust properties instead of the assumptions made before. Eventually, this process requires several iterations.

A complete set of model parameters

With the final set of model parameters, one can obtain independent mass estimates from all images as well as from the SED. These masses should be consistent. In the case of a slightly inclined disk and scattered light data available, one can further verify the fit and break potential remaining degeneracies quantifying how well the scattering asymmetry is reproduced by the model.

6.2.3 Modeling the Hubble scattered light images

Due to the high spatial resolution and the lower amplitude of the PSF subtraction residuals compared to the other scattered light images, the F606W image is the best choice for starting the modeling. To reduce the influence of PSF subtraction errors on the modeling, the inner $2''$ (≈ 60 AU) in radius around the center of the image mentioned by Ardila et al. (2004) are masked and neglected in the analysis. An error map for the PSF subtracted image is obtained from under- and over-subtractions of the PSF in each pixel derived from different PSF reference stars observed. The following equation is employed:

$$\sigma_i = \frac{1}{2} \left(\left| \, \mathrm{high}_i - \mathrm{low}_i \, \right| \right) + \mathrm{noise}. \tag{6.8}$$

In this equation i runs over all pixels and low_i and high_i are values obtained from the under- and over-subtraction (minimum and maximum value in one pixel subtracting the different PSF references). Additionally, the $1\,\sigma$ noise level is added, derived from pixel to pixel noise in regions of the original image far from the star where no signal is detected.

[2]Simplifying assumption: The density distribution is the same for all dust species (size, composition; see Sect. 6.2.1).

Table 6.2: Parameter space for modeling the HST/ACS F606W image (upper, middle) and the SED (lower).

Parameter	Grid	Range	Spacing
α_1	coarse	0.0 – 14.0	0.5
r_p [AU]		112.0 – 129.0	1.0
s [AU]		−10.0 – 60.0	1.0
α_1	fine	4.5 – 10.0	0.1
r_p [AU]		118.2 – 122.7	0.3
s [AU]		10.0 – 50.0	1.0
a_min [μm]	–	0.5 – 20	0.1
γ		2.0 – 5.0	0.1

To find the radial dust distribution, the parameters describing the grain size distribution are fixed and only the free parameters of the particle density distribution (α_1, r_p, and s) are varied. The parameters of the grain size distribution (a_min and γ) are fixed as follows:

- The value of a_min is fixed to 1.0 μm. The β ratio (Eq 2.21) for the employed dust around HD 107146 is computed. A blow-out size of 0.5 μm can be found. In contrast, the dust is scattering significantly red with respect to the stellar spectrum in the range of 0.6 μm to 1.1 μm (Fig. 6.1, 6.2), implying the absence of small, Rayleigh scattering dust grains. For the adopted dust properties, only a minimal grain size larger than $\approx$ 1.0 μm results in a red scattering disk in the observed range of wavelengths.
- A value of $\gamma = 3.5$ is chosen, being expected from an equilibrium collisional cascade. The Poynting-Robertson timescale t_PR for a particle with $a_\mathrm{min} = 1\,\mu$m to spiral onto the star from 100 AU is calculated (Eq. 2.29). A value of 1.7×10^7 years is found. Thébault & Augereau (2007) modeled collisional processes in debris disks and found collision time scales t_coll much smaller than 10^7 years for micron-sized particles, decreasing with increasing disk mass. Taking into account the high mass of the disk (Williams et al. 2004), the expected collision time scale is about two orders of magnitude lower, e.g. 10^5 years. One can conclude that collisions clearly dominate the evolution of the dust ($t_\mathrm{coll}/t_\mathrm{PR} < 6.0 \times 10^{-3}$).

For the adopted inclination of the disk of 25°, the adopted values of a_min, a_max, and γ produce a scattering phase asymmetry in the surface brightness that is in good agreement with the observed one.

To find the best-fit model, scattered light images for a grid of model parameters of the analytical density distribution (α_1, r_p, and s) are simulated. After a first, coarse search, a grid with smaller spacings centered on the best fit value of the coarse search is employed

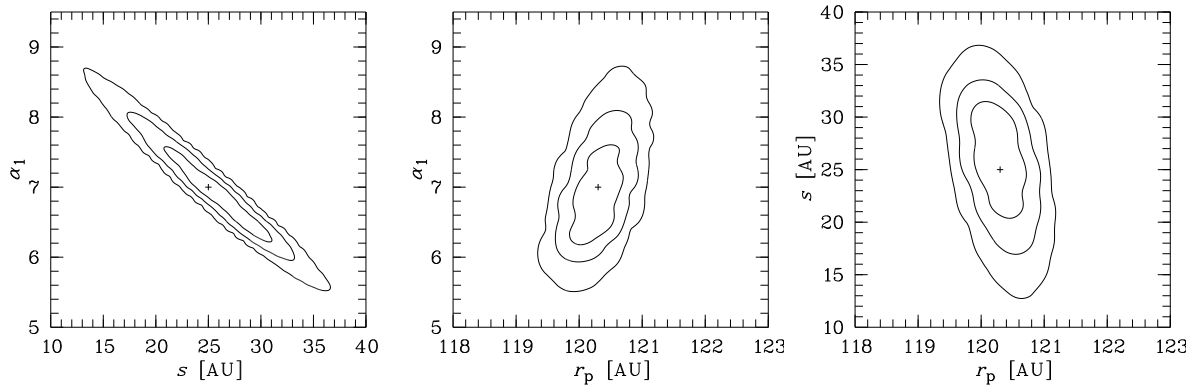

Fig. 6.3: Projection of the three dimensional ellipsoids of constant χ^2 on the r_p = const (*left*), s = const (*center*), and α_1 = const (*right*) planes from fitting the F606W image. The contour levels show 1 σ, 2 σ, and 3 σ levels of confidence, respectively. The cross indicates the position of the best-fit values. The plots illustrate very well the correlation between α_1 and s and the very weak correlations between these parameters and r_p, respectively.

for the final fitting (Table 6.2). Each simulated scattered light image is convolved with the corresponding PSF, derived with the Tiny Tim software[3] and is scaled to minimize the χ^2 derived from the observed and modeled image and the error map:

$$\chi^2 = \sum_i \left(\frac{\text{observation} - \text{model}}{\text{uncertainty}} \right)^2 . \tag{6.9}$$

In this equation, the sum runs over all pixels of the used images that have not been masked (Fig. 6.4).

The resulting best-fit parameters are listed in Table 6.3. Profiles derived from the best-fit model in the F606W and F814W filters are shown in Fig. 6.2. Confidence levels on the best-fit parameters derived from the distribution of χ^2 in the parameter space are plotted in Fig. 6.3. They are estimated by computing the values of χ^2 on a three dimensional grid in the parameter space and by estimating the probability p for each model j using the equation

$$p = \exp\left[-\left(\chi_j^2 - \chi_{\text{best}}^2 \right) \right] . \tag{6.10}$$

6.2.4 Deriving a_{min} and γ from the SED

In the previous section, the radial dust density distribution from the scattered light images has been derived. Under the conditions described in Sect. 6.2.3, the results of this approach are independent from the grain properties such as lower grain size and size distribution. Employing this density distribution and assuming that it is the same for all grain sizes, one

[3] http://www.stecf.org/instruments/TinyTim/tinytimweb

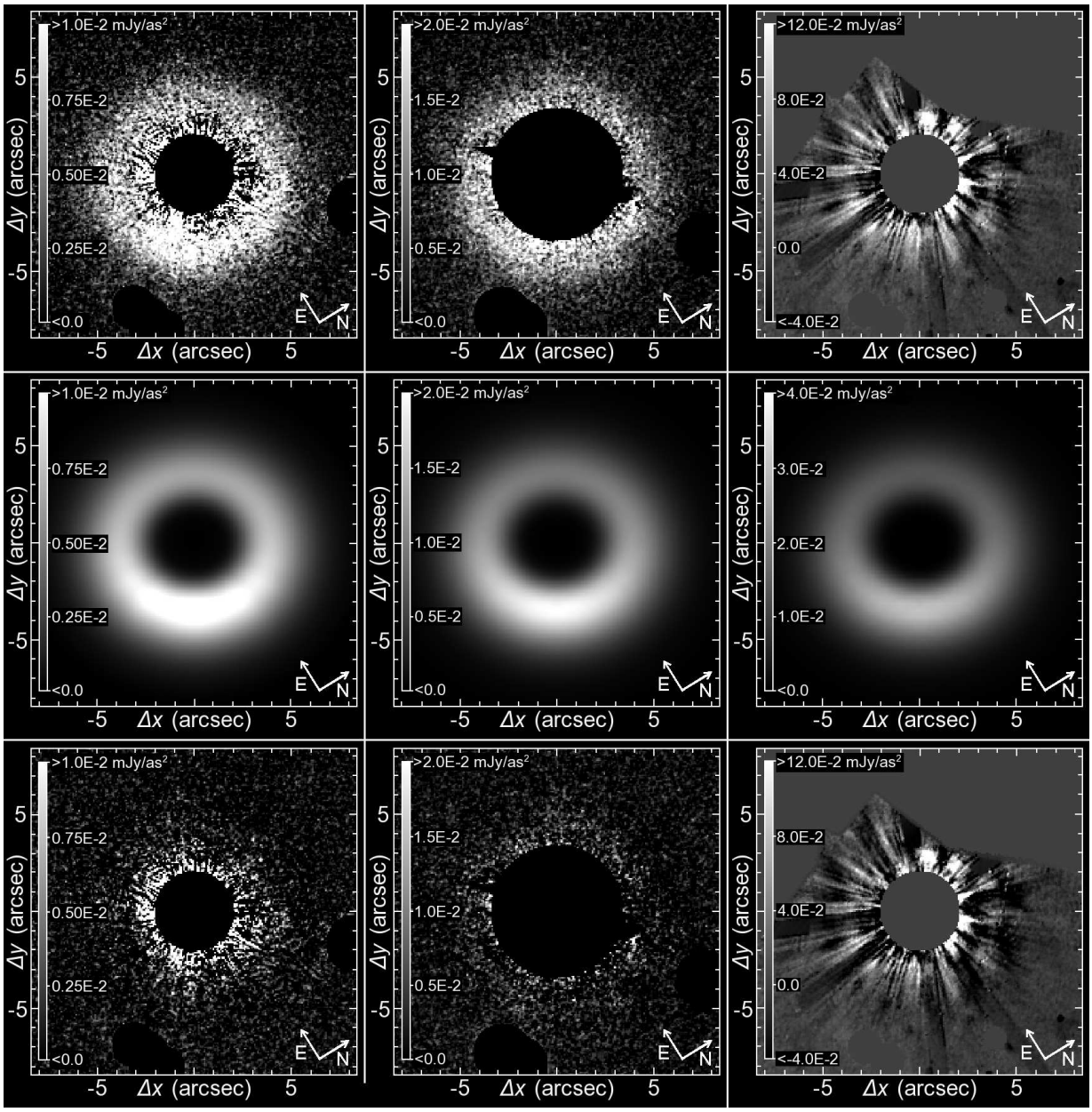

Fig. 6.4: Observed (*top*), modeled (*center*), and model subtracted images (*bottom*) in the F606W (*left*), the F814W (*center*), and the F110W (*right*) HST filters using the final model derived in this work. The images have been rotated, so that the major axis of the disk is oriented along the x-axis. Only the considered parts of the images are shown, while regions of large residuals from PSF subtraction or contaminated by other objects on the line of sight are masked. Note the different flux scales in different columns. The model image in the right column is displayed in a different way than the data and model subtracted data to better visualize the disk.

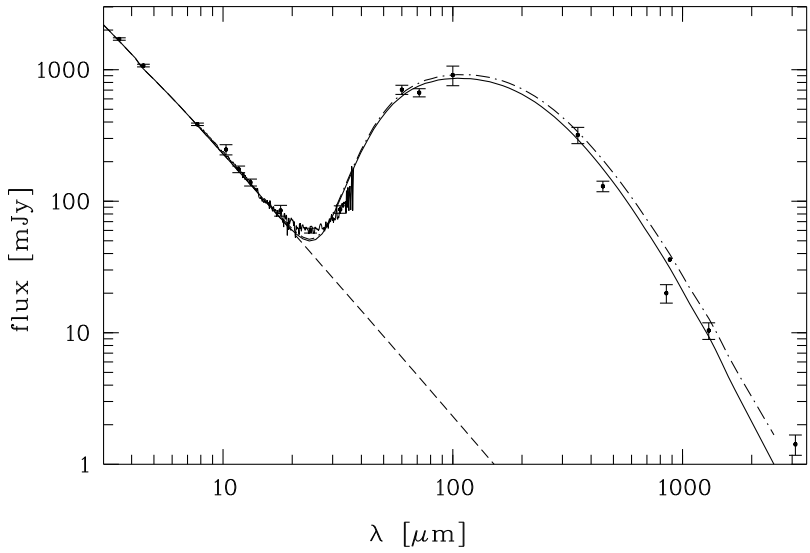

Fig. 6.5: Simulated SED from the single component best-fit model. The solid and dashed lines represent the modeled SED and the stellar photospheric flux, respectively. Photometric measurements in the plotted wavelength range with corresponding error bars and the considered *Spitzer* spectrum are plotted, too. The data point at 880 μm without error bar is taken from Hughes et al. (2011) and is not considered in the fit. The discrepancies, in particular with the *Spitzer* spectrum, are discussed in Sect. 6.3.2. The dot-dashed line represents the modeled SED corrected for the neglected large grains (Sect. 4.4) using Eq. 4.3 and an infinite real upper grain size.

can now simulate the SED of the debris disk to derive best-fit values for the parameters a_{min} and γ of the grain size distribution. The values assumed in Sect. 6.2.3 are used as starting values and the parameters are not limited on a certain range. However, since one does not expect values too far from what was assumed in Sect. 6.2.3, only the range of a_{min} and γ listed in Table 6.2 is searched effectively. For each fit, the corresponding disk mass is derived and compared to the mass derived from the F606W image using the same model parameters (dust composition and radial distribution).

No solution is found that results in total disk masses derived from SED and scattered light that differ by less than a factor of 1.4. The masses derived from scattered light are in any case larger than these derived from the SED. Taking into account that these mass estimates have been derived from observations which potentially trace different fractions of the dust distribution (i.e., grains of different size) and the uncertainties in flux scaling that arise from photometric calibration and stellar PSF subtraction, the resulting mass range is rather narrow and the derived masses are considered to be consistent. However, it is impossible to reach the initial goal to derive *one* mass value from all data sets to make it one final model parameter as it would have been from fully simultaneous modeling. This discrepancy is discussed in Sect. 6.3.2. For this reason, the SED is fitted employing the

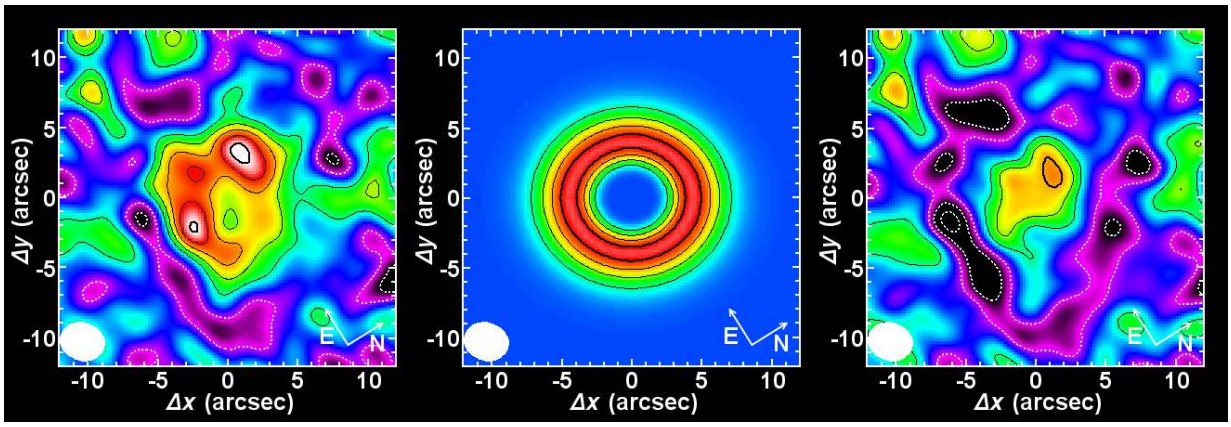

Fig. 6.6: Observed CARMA 1.3 mm map (*left*), modeled image (*center*), and model subtracted map (*right*). The contour levels have increments of $1\,\sigma$. White, dashed levels start at $-1\,\sigma$ and indicate negative values, while black, solid levels start at $1\,\sigma$ and indicate positive values, where $1\,\sigma = 0.35$ mJy/beam. A bold line is used to mark the maximum contour in each image. The FWHM of the synthesized beam ($3\farcs2 \times 2\farcs7$) is shown in the lower-left corner.

dust density distribution derived from the scattered light data, but without the constraint that the derived masses should be identical. Instead, independent disk masses are derived from each data set (scattered light data and SED) for the final, unified model with the radial dust distribution derived from the F606W image and the dust composition derived from the SED of the system through proper scaling of the simulated data.

Furthermore, it is not possible to reproduce the *Spitzer* spectrum and the other SED data simultaneously (Fig. 6.5). Thus, the *Spitzer* spectrum is only considered including the synthetic photometry derived from it at 13 μm and 33 μm (Hillenbrand et al. 2008). The discrepancies with the shape of the spectrum are discussed in Sect. 6.3.2.

Keeping in mind the above deficiencies, the fitting is continued with the approach described in Sect. 6.2.2. The best-fit values for the parameters describing the dust properties ($a_{\rm min}$ and γ) are listed in Table 6.3. The resulting model SED is shown in Fig. 6.5. Adopting these results for the grain properties instead of the assumptions made in Sect. 6.2.3, the results on the density distribution derived there are confirmed.

6.2.5 Verifying the model using the CARMA 1.3 mm map

As described before, the scattered light images do not allow to determine the dust distribution within the inner $2''$ (57 AU) from the star. Furthermore, the spatial dust distribution seen in scattered light is dominated by the distribution of the smallest grains. It can put only weak constraints on the distribution of grains with radii larger than $\sim 100\,\mu$m. To verify the spatial dust distribution derived from the scattered light images, one can use the CARMA 1.3 mm map (Fig. 6.6). However, in this image most of the disk is detected with an average surface brightness of only $\approx 3\,\sigma$, while there are two peaks reaching $\approx 5\,\sigma$. Due

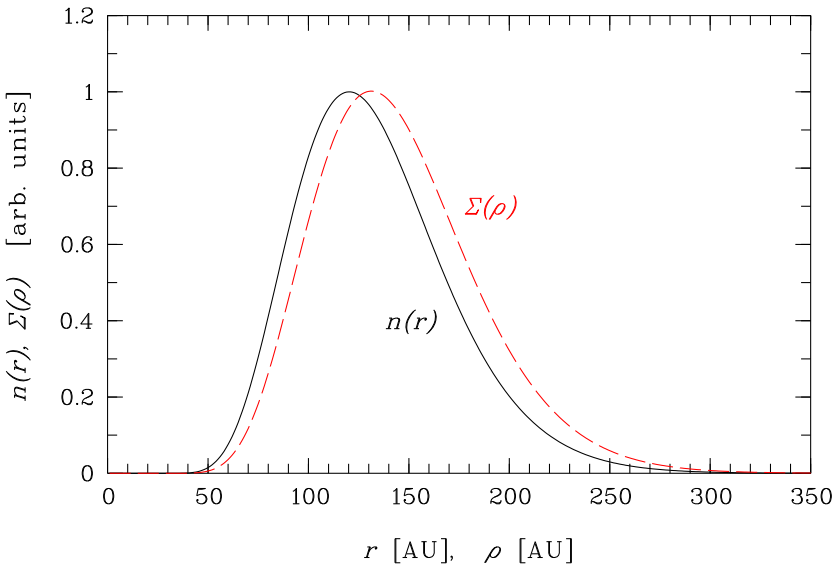

Fig. 6.7: Volume density distribution $n(r)$ over the radial distance r from the star and surface density distribution $\Sigma(\rho)$ over the distance ρ from the star projected on the disk mid plane for the best-fit model (parameters see Table 6.3). The analytical functions for $n(r)$ and $\Sigma(\rho)$ transform into each other following Eq. 6.4. Both distributions are displayed in arbitrary units and scaled to a peak height of one for each distribution, so that they can easily be compared. The peak particle density is $8.03 \times 10^{-6}\,\mathrm{m}^{-3}$, while the peak surface density amounts to $2.64 \times 10^{7}\,\mathrm{m}^{-2}$.

to its low SNR and the low angular resolution relative to the HST images, the 1.3 mm map is not used to fit model parameters. However, it can be verified that the model derived from the other data is consistent with the CARMA observations.

Therefore, images at 1.3 mm are simulated using the model derived above. Observations are simulated from the best-fit model image using the actual u-v spacings from the CARMA observations. These model u-v data points are subtracted from the observations and the residual image is reconstructed using the same image parameters as in Corder et al. (2009). To correctly scale the modeled data to the observed source flux, the remaining flux in the reconstructed, model subtracted image is minimized and a disk mass is derived (Table 6.3).

From the reconstructed, model subtracted image (Fig. 6.6), one finds that the model reproduces the global behaviour of the CARMA map, even though better results for slightly lower peak radii and/or a shallower decrease of the density distribution in the inner regions might be found. The remaining deficiencies are rated as insignificant ($< 3\,\sigma$). One can conclude that the density distribution derived from the scattered light data in combination with the grain size distribution derived from the SED data is consistent with the CARMA data, keeping in mind the large uncertainties. Furthermore, the two peaks visible in this image are subtracted very well by the radially symmetrical image and peak residuals are around $3\,\sigma$. This implies that these structures may be noise, rather than real structures in the disk induced by a massive planet orbiting the star within the inner edge of the disk as

Table 6.3: Derived model parameters.

Parameter	Derived Value	Uncertainty
α_1	7.0	6.2 ... 7.6
r_p [AU]	120.3	119.8 ... 120.7
s [AU]	25	21.0 ... 33.0
a_min [μm]	2.5	2.0 ... 3.0
a_max [μm]	1000.0	(fixed)
γ	3.6	3.5 ... 3.7
M_F606W [$\mathrm{M}_\odot$]	6.2×10^{-7}	–
M_F814W [$\mathrm{M}_\odot$]	6.5×10^{-7}	–
M_F110W [$\mathrm{M}_\odot$]	8.5×10^{-7}	–
M_CARMA [$\mathrm{M}_\odot$]	6.7×10^{-7}	–
M_SED [$\mathrm{M}_\odot$]	4.4×10^{-7}	–

Notes. The uncertainties are given as $1\,\sigma$ confidence levels. For details see Sects. 6.2.1, 6.2.3, and 6.2.4.

suggested by Corder et al. (2009). Furthermore, the complementary data obtained with a similar SNR by Hughes et al. (2011) at 880 μm show similar structures, but at significantly different positions in the disk. This cannot be explained by proper motion of clumps in the disk on the short time scales between the two observations[4], giving further evidence that the structures are artifacts of the image reconstruction.

At this part of the work, one can already conclude that the small particles seen in scattered light and the larger particles traced by the CARMA data are cospatial within the errors of the available data. This is important, since it supports the assumption made that particles of all sizes are distributed in the same way.

6.3 Discussion

6.3.1 Results

One model was used (with the total disk mass derived from the different data sets varying by a factor of ≈ 1.5) to reproduce the F606W and F814W images (Figs. 6.2 and 6.4), the CARMA 1.3 mm map (Fig. 6.6), and the SED of the HD 107146 system (Fig. 6.5). The disk is found to be a broad ring with a peak of the density distribution $n(r)$ at $120.3^{+0.4}_{-0.5}$ AU ($\widehat{=}$ $131.4^{+0.5}_{-0.6}$ AU for the surface density distribution $\Sigma(\rho)$ Fig. 6.7). This is in good agreement with the value derived by Ardila et al. (2004). A lower dust grain

[4]The CARMA observations were carried out in 2007 and 2008, while the SMA observations were carried out early 2009.

size of $2.5^{+0.5}_{-0.5}\,\mu$m is found, inconsistent with the blow-out size of the system of $0.5\,\mu$m. The exponent of the grain size distribution of $\gamma = 3.6^{+0.1}_{-0.1}$ is consistent with the value expected from an equilibrium collisional cascade. Table 6.3 summarizes the derived model parameters.

The available data are consistent with all dust in the system having the same radial distribution. This can be expected from a collision dominated disk (Wyatt 2005). From integrating the synthetic stellar spectrum and the modeled SED of the disk, a fractional luminosity $L_{\rm d}/L_\star = 1.07 \times 10^{-3}$ is found, which supports this scenario (Wyatt 2005). However, there are some data available that are reproduced by the above derived model only in an unsatisfactory way, in particular the shape of the *Spitzer*/IRS spectrum. These discrepancies are discussed in the following section.

6.3.2 Remaining discrepancies between the model and available data

The available data could be reproduced with only one global model of the disk. However, there remain some discrepancies the most important ones of which are discussed in this section:

- At wavelengths $\lambda < 40\,\mu$m, the modeled SED poorly reproduces the observed one sampled by the *Spitzer* spectrum (Fig. 6.5).
- A minimum grain size is found that is by a factor of 5 larger than the expected blow-out size.
- It was not possible to derive a unique value for the mass from all data sets. In contrast, the derived masses differ by a factor of up to 1.5.

While the model allows to reproduce the general structure of the disk very well, important insights may be gained from the remaining discrepancies. They may be ascribed to a number of deficiencies of the above model that only become relevant due to the large number of high quality complementary data:

- A discontinuity of the radial density distribution in the inner regions of the disk hidden by the coronagraph in the scattered light observations (e.g., an additional, inner disk component) would be able to significantly alter the shape of the SED at the short wavelength edge of the excess.
- The size distribution of the smallest grains may be only poorly described by a single power-law that describes the distribution of the larger grains very well. More detailed grain size distributions can be derived by dynamical and collisional modeling of debris disks (e.g., Thébault et al. 2003; Krivov et al. 2006; Thébault & Augereau 2007; Löhne et al. 2008). The results show a wavy distribution with an overdensity of small grains (approximately twice the expected blow-out size).
- The flux at long wavelengths neglected by adopting an upper cut-off grain size might result in a flatter best-fit grain size distribution than the real one. A steeper grain

size distribution might result in a larger amount of small grains. This would increase the scattering efficiency of the dust and, thus, might be able to make the dust masses derived from scattered light and thermal reemission data more consistent.

- A more complex chemical composition of the dust than the used astronomical silicate may be present.

In particular, the first two points might have a strong effect on the shape of the SED at the short wavelength edge of the excess making the model SED more consistent with the *Spitzer* spectrum. Hence, possible extensions of the model are discussed in the following to account for these deficiencies. Exploring the chemical composition of the dust, in particular the shape of the dust grains, requires significant additional computational effort and is beyond the scope of the present work.

Unsatisfactory fit to the Spitzer/IRS spectrum

The most obvious and significant discrepancy of the derived model with the data is the different shape of the modeled SED in the range of the *Spitzer*/IRS spectrum. As described above, this might be explained in different ways. An overabundance of small (warm) grains is expected to result in an increase of the simulated short-wavelength excess. In such a scenario, one would expect that the additional excess flux seen in the *Spitzer* spectrum originates from the same region of the disk as the long wavelength excess.

An alternative explanation is an additional, inner disk present in the system, such as discussed in the case of the ϵ Eridani debris disk (Backman et al. 2009). Such an additional, warm disk component would add excess flux at mid-infrared wavelengths. In this case, the long wavelength and short wavelength excess should originate from different regions in the disk.

None of the available, spatially resolved data allow to distinguish between the two scenarios directly. However, one can explore what one would have to add to reproduce the *Spitzer* spectrum using

(a) An additional grain size component to mimic a more complex grain size distribution. Here, the dust is spatially distributed the same way as the other dust (Sect. 6.2.3). The chemical composition of the dust is the same as before (astronomical silicate). Only one distinct grain size is used here, so this is the only additional free parameter.

(b) An additional, inner disk component. A disk model is used that is described by a power-law radial density distribution $n(a) \propto a^{\alpha^{\mathrm{add}}}$ with inner radius $r_{\mathrm{in}}^{\mathrm{add}}$, outer radius $r_{\mathrm{out}}^{\mathrm{add}}$, and fixed opening angle of 10°. The grain size distribution is described by $dn(a) \propto a^{-\gamma^{\mathrm{add}}}\, da$ with lower grain size $a_{\mathrm{min}}^{\mathrm{add}}$ and upper grain size of 1 mm (the same parameterization as in Sect. 6.2.1). The same chemical composition (astronomical silicate) as before is employed. There is a total of 5 free parameters, here. None of them can be fixed making simple physical assumptions. Thus, it is clear that this fit will be very degenerate. However, one will be able to evaluate, whether this scenario is able to reproduce the shape of the *Spitzer* spectrum at all. The explored parameter space for

Table 6.4: Parameter space explored and fitting results for modeling the remaining *Spitzer*/IRS flux by an additional, inner disk component.

Parameter	Range	Spacing	Best-fit	Uncertainty[(1)]
$r_{\rm in}^{\rm add}$ [AU]	0.2 – 250.0	temp[(2)]	0.2	0.2 ... 0.6
$r_{\rm out}^{\rm add}$ [AU]	2.0 – 250.0	temp[(2)]	42.2	6.0 ... 250
$\alpha^{\rm add}$	-5.0 – 5.0	0.1	0.8	-2.1 ... 1.1
$a_{\rm min}^{\rm add}$ [μm]	0.5 – 100	log[(3)]	3.3	0.8 ... 4.4
$\gamma^{\rm add}$	2.0 – 10.0	0.1	10.0	3.6 ... 10.0
$M^{\rm add}$ [$M_\odot$]	free	cont[(4)]	3.6×10^{-11}	...

Notes. [(1)] Confidence levels ($1\,\sigma$); [(2)] equally distributed in temperature of the dust species with the largest gradient of the radial temperature distribution (spacing = 2 K); [(3)] equally distributed in $\log(a)$ (100 size bins); [(4)] continuous – The fitting of this parameter has not been done on a grid, but a continuous, unlimited range of possible values has been used.

this fit is shown in Table 6.4.

To modify the model of the outer disk and to fit the properties of the additional disk component from approaches (a) and (b), the following strategy is used:

- The parameters of the (outer disk) model are changed so that the simulated flux of the system is smaller than the measured flux in the *Spitzer* spectrum, but is still consistent with the long wavelength SED observed. Since the radial density distribution derived from the scattered light data is still valid, one may only change the parameters of the grain size distribution. An increase of the lower grain size $a_{\rm min}$ to 3.5 μm and of the total disk mass derived from fitting the SED data to $4.8 \times 10^{-7}\,M_\odot$ is found to be well suited to reach this goal.
- The (modified) model SED of the system is subtracted from the *Spitzer* spectrum.
- The remaining excess flux is fitted by the two additional disk components, respectively, using `SAnD`.

The exact choice of $a_{\rm min}$ is rather arbitrary, since one is not able to distinguish between flux from the original disk model (with changed dust parameters) and the hypothetic, additional component. However, if one finds an additional component that is able to reproduce the *Spitzer*/IRS spectrum, then in this approach the value of $a_{\rm min} = 3.5\,\mu$m can be considered as a lower limit on the lower dust grain size of the original dust component. Smaller values would violate the constraint that the excess from this component shall be smaller than the excess measured by *Spitzer*/IRS. On the other hand, almost any value larger than $a_{\rm min} = 3.5\,\mu$m will be possible, since the missing flux at longer wavelengths can then be reproduced in a wide range by changing the parameters of the additional component.

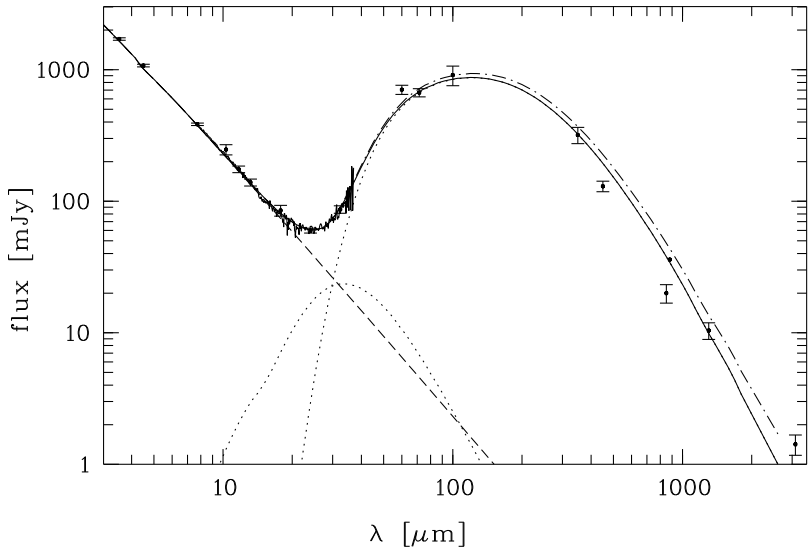

Fig. 6.8: SED fit with the modified dust composition in the outer disk and an additional, inner disk component (Sect. 6.3.2). The two dotted curves indicate the emission from the two dust components only. The dot-dashed line represents the modeled SED corrected for the neglected large grains (Sect. 4.4) using Eq. 4.3 and an infinite real upper grain size.

From approach (a), one finds that it is not possible to fit the shape of the *Spitzer* spectrum with an additional grain size component (with the radial density distribution derived in Sect. 6.2.3). Furthermore, this would add significant flux at longer wavelengths. In any case, the dust is too cold (too far from the star) in this approach.

In contrast, with approach (b) one is able to significantly improve the fit on the *Spitzer* spectrum without lowering the quality of the fit on the other SED data (Table 6.4). Fig. 6.8 shows the new best-fit SED from this approach. The result is a disk that is extended from the inner rim of the outer disk to very close to the star. A nearly constant radial surface density distribution is found. The lower dust grain size (3.3 μm) is very close to the lower grain size of the outer disk in this approach (3.5 μm). However, one finds a very large exponent of the grain size distribution (best-fit: $\gamma^{\mathrm{add}} = 10$), i.e., a very narrow size distribution around the lowest grain size. The disk mass for this inner component then results to $3.6 \times 10^{-11}\,\mathrm{M}_{\odot}$. From this model, total scattered light fluxes from the inner disk component of 0.037 mJy and 0.052 mJy are predicted at 0.6 μm and 0.8 μm. The total re-emitted flux from this component is plotted in Fig. 6.8 as a function of the wavelength.

The result suggests that the inner disk component in this scenario is produced by collisions close to the inner rim of the outer disk and is then dragged inwards towards the star by Poynting-Robertson drag (spatial distribution of the dust, steep grain size distribution, lower grain size consistent with that in the outer disk). This scenario has proven successful to explain the origin of the dust in the habitable zone of ϵ Eridani (Reidemeister et al. 2011).

However, with the large uncertainties on these best-fit values, it is not possible to draw strong conclusions from the resulting model. An additional, inner ring of planetesimals producing new dust through collisions (power-law exponent of the grain size distribution of 3.6) would also be possible within the $1\,\sigma$ uncertainties of the fit.

Different disk masses derived from different data sets

While it was possible to reproduce most of the available data using one model of the disk, it was not possible to derive a unique disk mass (Sect. 6.2.4).

Again, a more complex grain size distribution than the employed one is one possible explanation. A different slope of the grain size distribution for the smallest grains present in the system would result in a different surface brightness at scattered light wavelengths, since these observations are very sensitive to the smallest grains. A derived disk mass from scattered light data that is too large (as it is the case for the present results) would mean a too low surface brightness of the modeled data at these wavelengths. An underabundance of the smallest grains in the model seems to be obvious. However, it is found in Sect. 6.3.2 that adding an additional grain size component is not able to solve the discrepancy with the *Spitzer* spectrum. Thus, a different chemical dust composition or, alternatively, a different structure of the grains is the most plausible explanation. A different chemical composition can increase the scattering efficiency of the dust. The presence of fluffy, porous grains might alter the absorption efficiency and scattering efficiency and the wavelength dependence of these quantities independently (e.g., Voshchinnikov et al. 2006; Voshchinnikov & Henning 2008).

A large lower dust grain size

The lower grain size from dynamical and collisional models of debris disks is in any case consistent with the expected blow-out size, while there is an overdensity of particles with approximately twice the blow-out size (e.g., Thébault et al. 2003). In contrast, for HD 107146 one finds a lower grain size of ≈ 5 times the expected blow-out size for the original model and even larger for the model with the additional inner disk component. While the lower grain size a_{min} is usually heavily degenerate with the spatial dust distribution in pure SED modeling, this is well constrained in the present work by the scattered light images.

To lower the value of a_{min} in the derived solution, one can solely change the chemical composition or shape of the dust grains to get in general cooler dust. The inclusion of water ice has been successful to solve this problem (Augereau et al., in prep.). A different chemical dust composition or shape might also increase the value of β of the dust and, thus, increase the expected blow-out size to a level more consistent with the findings of the present modeling. Again, a different structure of the grains might have a very similar effect.

6.3.3 Is the HD 107146 debris disk unusually massive for its age?

Compared to other stars harboring debris disks, HD 107146 is of an intermediate age of 100 Myr to 150 Myr. It is harboring a very massive debris disk. Spatially resolved debris disks with comparable dust masses are, e.g., β Pic (Zuckerman & Becklin 1993), HD 99803B (Wyatt et al. 2003), HR 4796 (Sheret et al. 2004), and HR 8799 (Su et al. 2009). All these stars are A type stars. Of these stars, HD 99803B and HR 8799 might have a comparable age to HD 107146, while the two other ones are significantly younger. The dust mass in debris disks is expected to decline with age trough well explored depletion mechanisms (e.g., Silverstone 2000; Löhne et al. 2008; Wyatt 2008; Roccatagliata et al. 2009) and towards later spectral types due to lower initial disk mass. In contrast, HD 107146 is an intermediate age G type star harboring a disk with a mass comparable to the mass of disks around young A-type stars. This suggests that the HD 107146 disk is special among the known, spatially resolved debris disks. Its high age and high dust mass may imply that the system is undergoing a delayed stirring (Dominik & Decin 2003) analog to the Late Heavy Bombardment in our own Solar System (Tera et al. 1974; Kring & Cohen 2002; Gomes et al. 2005) as also suggested for HR 8799 (Su et al. 2009).

6.3.4 The origin of the disk shape

The shape of the HD 107146 debris disk is similar to that of Fomalhaut (HD 216956), an A3V star of 200 Myr (Habing et al. 2001), although with $6.2 \times 10^{-8}\,M_{\odot}$ (Sheret et al. 2004), Fomalhaut's debris disk has a lower mass by one order of magnitude. Both stars have comparable ages. The similar shape of the two disks and the fact that the shape of the Fomalhaut disk seems to be induced by the planet Fomalhaut b orbiting the Star (Kalas et al. 2008) raises the question if a planet is embedded also in the disk of HD 107146. However, while the inner edge of Fomalhaut's debris disk represents a sharp break in particle density, the inner edge of the HD 107146 debris disk seems to be a shallow decrease. Furthermore, the Fomalhaut disk is off-centered from the stellar position, which is interpreted as a result of the planet-disk interaction. There is no evidence in the data that the HD 107146 disk is off-centered in a similar way. Alternatively, a birth ring scenario of a collision dominated disk (as it is expected for the HD 107146 debris disk) is also able to explain inner gaps in debris disks without the need of a massive, interior planet (Krivov 2010).

6.4 Conclusions

A detailed model of the debris disk around HD 107146 has been created and fitted to all available data using the approach developed in the present chapter. A broad range of resolved data from optical scattered light data to millimeter data as well as the SED have been reproduced by a single radial density profile. All model parameters have been fixed without remaining degeneracies using only one scattered light image and the well-sampled SED of the disk in this particular case (Sect. 6.2). The disk is found to be a broad ring

of dust with smooth inner and outer boundaries and with a peak position from the star and FWHM of the surface density of 131 AU and 91 AU, respectively. It is concluded from the modeling results that the disk is heavily collision dominated. Discrepancies of the modeling are discussed. From these discrepancies, one finds strong evidence for an additional, inner disk component, possibly near the habitable zone of the star and for a different chemical composition or shape of the dust grains. It is found to be likely that the additional inner disk component is predominantly composed of small grains and the results from the modeling are consistent with these grains being released at the inner edge of the outer disk and dragged inwards due to Poynting-Robertson drag. Only detailed, combined modeling of the large amount of available high quality, complementary data was able to reveal these signposts. No evidence of an orbiting planet is found from the available data and a birth ring scenario is found likely to be responsible for the ring-like shape of the disk.

7 Steep SEDs from Herschel/DUNES

In the previous section, a comprehensive model of a debris disk has been derived through detailed multi-wavelength modeling of a large amount of complementary data available. As described in Chap. 4, pure SED fitting of debris disks is usually very degenerate. However, the grain size distribution can be described by a power-law and the power-law exponent derived from pure SED fitting is usually well constrained and consistent with the analytical value of -3.5 expected from an equilibrium collisional cascade (Sect. 2.2.3). In this chapter, the potential *Herschel*/DUNES discovery of an unusually steep decrease of the SEDs of three spatially unresolved debris disks around Sun-like stars, HIP 103389 (HD 199260), HIP 107350 (HN Peg, HD 206860), and HIP 114948 (HD 219482), is presented[1]. The steep decrease occurs in the range of 70 μm to 160 μm, inconsistent with a dust grain size following a power-law distribution derived from an equilibrium collisional cascade. Results from detailed SED modeling including additional photometric data from the literature are presented. Furthermore, it is demonstrated on the example of the three targets that the analysis of data of faint point sources obtained with *Herschel* depends very much on the photometric calibration and the exact determination of the uncertainties. For *Herschel*, the data reduction pipeline HIPE (Ott et al. 2010) is provided. However, it is still under development and different versions of the pipeline give very different results. Thus, no conclusive statement can be made whether the discovery of these sources is real or a result of the still incomplete understanding of the data obtained.

Observations and data reduction as well as a detailed re-analysis of the stellar properties including new observations are carried out within DUNES and the results have been provided for the present work. A detailed description of this work for the whole DUNES sample can be found in Eiroa et al. (in prep.). In the present chapter, only a brief summary of the relevant parts of this work is presented (Sect. 7.1). The basic observational results are summarized in Sect. 7.1 as well. A theoretical discussion of how steep the decrease of the SED of a debris disk towards longer wavelengths is expected to be and a characterization of unusually steep SED sources are given in Sect 7.2. A detailed description of the modeling of the systems can be found in Sect. 7.3 and results are discussed in Sect. 7.4. Conclusions are given in Sect. 7.6.

[1]Two of the sources, HIP 103389 and HIP 107350, are shared targets between the DUNES survey in the context of which the analysis is carried out and the DEBRIS survey (Matthews et al. 2010; Phillips et al. 2010).

Table 7.1: Observational results obtained by *Herschel*/DUNES for the steep SED sources[(a)].

Source	HIP 103389		HIP 107350		HIP 114948	
	HIPE 4.2	HIPE 7.2	HIPE 4.2	HIPE 7.2	HIPE 4.2	HIPE 7.2
$F_{\mathrm{PACS\,70}}$	47.4 ± 2.7	44.0 ± 2.3	...	...	...	...
$F_{\mathrm{MIPS\,70}}$	46.6 ± 3.8		28.4 ± 2.5		68.7 ± 3.0	
$F_{\mathrm{PACS\,100}}$	23.7 ± 1.4	26.3 ± 1.7	11.0 ± 0.9	15.1 ± 1.3	42.5 ± 2.2	40.8 ± 1.6
$F_{\mathrm{PACS\,160}}$	5.0 ± 1.3	7.7 ± 2.5	4.4 ± 1.5	4.4 ± 2.3	12.7 ± 1.9	13.3 ± 2.2
$F_{\star,70\,\mu\mathrm{m}}$[(b)]	13.8		13.4		15.0	
$F_{\star,100\,\mu\mathrm{m}}$[(b)]	6.8		6.6		7.3	
$F_{\star,160\,\mu\mathrm{m}}$[(b)]	2.7		2.6		2.9	
$\Delta_{100,70}$	1.94 ± 0.32	1.44 ± 0.33	2.66 ± 0.45	1.77 ± 0.49	1.35 ± 0.26	1.46 ± 0.23
$\Delta_{160,100}$	3.31 ± 0.69	2.61 ± 0.82	1.95 ± 0.88	2.62 ± 1.30	2.57 ± 0.44	2.38 ± 0.43
$\Delta_{160,70}$	2.72 ± 0.39	2.11 ± 0.46	2.25 ± 0.53	2.26 ± 0.74	2.04 ± 0.22	1.99 ± 0.25
FWHM[(c)]	$6\farcs8 \times 7\farcs1$		$7\farcs1 \times 6\farcs0$		$7\farcs2 \times 7\farcs2$	

Notes. Fluxes are given in mJy. Uncertainties on the flux measurements are total uncertainties including sky noise and calibration uncertainties. Δ_{ν_1,ν_2} is the spectral index measured from ν_1 and ν_2 (Sect 7.2), identified with the corresponding PACS bands.
[(a)] The *Spitzer*/MIPS 70 μm photometry is also listed, since these data complement the *Herschel* observations and are important to illustrate the unusual behaviour of the SEDs. These data are published by Beichman et al. (2006; HIP 103389 and HIP 114948) and Bryden et al. (2006; HIP 107350) and have been re-reduced in the context of DUNES (Eiroa et al., in prep.). [(b)] Predicted stellar photosphere using a PHOENIX/GAIA synthetic stellar model (Eiroa et al., in prep.). [(c)] FWHM as measured from the PACS images at 100 μm using a 2-D Gaussian fit.

7.1 Observations & data reduction

Two *Herschel*/PACS mini-scan map observations of each target were taken with the 100/160 channel combination[2] at array orientation angles of 70° and 110° (total on source integration time 1440 s) providing scan and cross-scan coverage to assist in the removal of noise artifacts from the final composite mosaic. In addition, two scan map observations of HIP 103389 were taken with the 70/160 channel combination with the same array orientations (total on source integration time 180 s). Each scan map consists of 10 legs of 3′ length, with a 4″ separation between legs, at the medium slew speed (20″ per second). In this way a region of ≈ 1 square arc minute around the source position was covered to uniform depth in the resulting mosaic.

PACS data reduction was carried out in version 4.2 (reduction 1) and 7.2 (reduction 2) of HIPE (Ott et al. 2010) starting from the level 0 products using the standard reduction

[2]The numbers give the central wavelengths of the channels in μm.

Table 7.2: Physical properties of the three stars considered in this chapter (for details see Eiroa et al., in prep.).

Star	HIP 103389	HIP 107350	HIP 114948
Distance [pc]	21.97	17.88	20.54
Spectral type	F7 V	G0 V	F7 V
$L_\star$ [$L_\odot$]	2.03	1.09	1.87
$T_{\rm eff}$ [K]	6257	5952	6240
$M_\star$ [$M_\odot$]	1.28	0.98	1.02
Age [Myr]	412^{+340}_{-230}	328^{+202}_{-166}	250^{+135}_{-135}

script (provided within HIPE). Two different reductions have been carried out, because changes in the still developing pipeline of HIPE may significantly affect the results. It is demonstrated that the results indeed do differ significantly and that the results from the new (but not necessarily better) version alter the results of the discussion (Table 7.1). PACS fluxes and sky noise were measured by aperture photometry using a custom script based on the IDL APER routine that is employing the DAOPHOT aperture photometry routines.

The data obtained in this work for the three sources as well as the predicted photospheric fluxes are listed in Table 7.1. Table 7.2 lists the main stellar parameters of HIP 103389, HIP 107350, and HIP 114948 (Eiroa et al., in prep.). The stellar contribution to the total SED of each star is estimated using a PHOENIX/GAIA synthetic stellar model (Brott & Hauschildt 2005). All three sources are found to have significant excess ($\geq 3\,\sigma$) at 70 μm and 100 μm. HIP 114948 also has significant excess at 160 μm. HIP 103389 and HIP 107350 have excesses at 160 μm of 1.8 σ and 1.2 σ. Offsets between optical positions and positions in the PACS 70 μm images are below 1 σ of the *Herschel* pointing accuracy. In each case, the observed excess is attributed to the presence of a debris disk associated with the star. The measured FWHM of the sources (derived from a 2-D Gaussian fit) are consistent with unresolved objects. One can therefore constrain the extension of the emitting area (adopting the distance of the objects listed in Table 7.2) to a diameter of less than 7.″1 (156 AU) for HIP 103389, 7.″1 (126 AU) for HIP107350, and 7.″2 (148 AU) for HIP 114948.

The SEDs of all three sources are found to exhibit an unusually steep decrease at the wavelength range of 70 μm to 160 μm (steeper than a black body radiator in the Rayleigh-Jeans regime) from the results of reduction 1, but this steepness is not significant using the results from reduction 2. It is based on the spectral index of the SEDs between two different wavelengths being larger than two (see Sect. 7.2 for a detailed description). The significance of this steepness is evaluated using error propagation. The results are listed in Table 7.1.

7.2 What is an unusually steep SED?

In this section, a qualitative discussion is given of how steep the SED of a debris disk is expected to be. First, the shape of the excess is investigated treating both the star and the disk as single temperature black body radiators. Later, the effects of a more realistic disk model, i.e., allowing for a range of temperatures and more realistic grain properties, are discussed.

7.2.1 Treating the dust as a single temperature black body

The spectral index Δ of an SED is defined as

$$\Delta = \frac{\partial \log F_\nu}{\partial \log \nu}, \tag{7.1}$$

where F_ν is the total flux of the object at the frequency ν. It is typically measured as the slope of the SED between two data points available, i.e.,

$$\Delta_{\nu_1,\nu_2} = \frac{\log F_{\nu_2} - \log F_{\nu_1}}{\log \nu_2 - \log \nu_1}. \tag{7.2}$$

The two frequencies ν_1 and ν_2 are further identified with their corresponding PACS wave bands (e.g., $\Delta_{100,70}$). It is well known that the spectral index of a black body radiator is $\Delta = 2$ in the Rayleigh-Jeans regime. It is decreasing towards shorter wavelengths, where the Rayleigh-Jeans approximation is not valid. A spectral index of $\Delta > 2$ means that the SED falls off towards longer wavelengths steeper than a single temperature black body. In the wavelength range where dust reemission is observed, the star will only contribute as an additional component with a spectral index of $\Delta = 2$. Thus, the contribution of the star does not alter the above discussion.

7.2.2 More exact treatment of the disk

The first step to expand the above discussion can be to allow for different dust temperatures, while the dust is still treated as a number of single temperature black bodies (i.e., a radially extended disk). A two component black body has been used successfully to model SEDs of debris disks (e.g., Hillenbrand et al. 2008). This results in a flatter SED ($\Delta_{\nu_1,\nu_2} < 2$) in the long wavelength regime than in the above case, since the flux of the colder dust component will contribute additional flux in the long wavelength regime of the warmer dust component. Thus, using several components with different temperatures one can only reach $\Delta_{\nu_1,\nu_2} = 2$ in the long wavelength regime of the coldest dust component (i.e., at even longer wavelengths compared to the single black body case above).

Using Mie theory, one can derive absorption efficiencies $Q_\lambda^{\mathrm{abs}}(a)$ for more realistic dust grains. The emission of a dust grain is then described following Eq. 2.6. The shape of the simple black body SED is modified by the function $Q_\lambda^{\mathrm{abs}}(a)$, which will result in a steeper decrease with wavelength in the Rayleigh-Jeans regime of the black body, if $Q_\lambda^{\mathrm{abs}}(a)$ is

decreasing with wavelength. Fig. 4.1 shows $Q_\lambda^{\rm abs}(a)$ for astronomical silicate (Draine 2003) and different grain radii a. $Q_\lambda^{\rm abs}(a)$ is close to 1 at short wavelengths, while it indeed exhibits a break at $\lambda \approx 2\pi a$ and then decreases towards longer wavelengths with λ^{-2} (or ν^2). This is analogous to the discussion of the opacity index, e.g., by Draine (2006). An SED of a dust disk that is steeper in the long wavelength regime than a black body is obviously possible. In any case, Δ can never be > 4 due to the slope of $Q_\lambda^{\rm abs}(a)$ of small grains at long wavelengths for the considered compositions (Eq. 4.1). However, debris disks are usually expected to be radially extended and to contain particles of different size. This suggests a broad range of dust temperatures to be present resulting in a flattening of the SED. In addition, the grain size dependence of the break in $Q_\lambda^{\rm abs}(a)$ means that the grains dominating the emission have to be smaller than $\approx \lambda/2\pi$ to result in an SED that falls off steeper than a black body (Draine 2006). This suggests grains smaller than $\sim 15\,\mu$m for the three disks presented in this chapter (Table 7.1). Thus, one qualitatively expects a narrow dust belt composed of small grains to be present. While a spectral slope steeper than 2 is common for debris disks at (sub-)mm wavelengths, such a behaviour is very unusual in the range of $\approx 100\,\mu$m (e.g., Liu et al. 2004; Hillenbrand et al. 2008; Roccatagliata et al. 2009). For the debris disks considered there, typical values of Δ at wavelengths around $100\,\mu$m are in the range of 0 to 2. On the other hand, previous observations had a much lower sensitivity at (sub-)mm wavelengths and, thus, only disks with reasonably large (sub-)mm excess could be detected resulting in an observational bias.

An unusually steep SED is defined in the present work to be an SED that exhibits a $\Delta_{\nu_1,\nu_2} > 2$ in at least one of the PACS band combinations of $70\,\mu$m, $100\,\mu$m, and $160\,\mu$m and for which a $\Delta_{\nu_1,\nu_2} = 2$ would not be possible within the $1\,\sigma$ uncertainties. These criteria are met by the three debris disks presented in this chapter, if one considers the results from reduction 1.

7.3 SED modeling

In this section, detailed analytical model fitting to the observed SED data is performed to explore quantitatively the conclusions on the disk properties derived in the above qualitative discussion. This is done using the results from reduction 1, since these results give the steep SEDs. The fitting results are expected to differ less significantly from standard solutions using the photometric data from reduction 2. For modeling of the three sources, `SAnD` (Sect 5.2.2) is employed. The stellar properties listed in Table 7.2 are used.

Only selected data points are used. This results in a total of 8 data points included in the fitting for each source. The SEDs of the sources can be seen in Fig. 7.1. The references for all photometric data points available for the three sources can be found in Eiroa et al. (in prep.). The selection is done by the following criteria:

- All flux measurements at wavelengths $> 10\,\mu$m are considered, but no upper limits, since they do not give significant additional information in the present case. Measurements at these wavelengths are also included, if they are photospheric, because they exclude

significant emission from the disk at these wavelengths.

- Measurements at wavelengths $< 10\,\mu$m are not included, since they are at much shorter wavelengths than the shortest wavelength at which excess is detected ($24\,\mu\text{m} \ldots 32\,\mu\text{m}$).
- To account for the *Spitzer*/IRS spectrum in a consistent way, an additional photometric point at $\lambda = 32\,\mu$m is extracted from these data following Hillenbrand et al. (2008) and is fitted along with the other photometric values. This will prove to be sufficient to get the whole *Spitzer*/IRS spectrum properly reproduced by all the best-fit models.

For the extraction of the synthetic photometry from the *Spitzer* spectrum, 10 consecutive data points centered at $\lambda = 32\,\mu$m are averaged. The uncertainty is computed by adding in quadrature the standard deviation of these data points and a 5% calibration uncertainty (*Spitzer*/IRS instrument handbook v4.0; Teplitz et al. 2011).

The capabilities of `SAnD` are used to explore a very broad range of parameters. The following model is employed:

- Radial surface density distribution $\Sigma(r) \propto r^{-\alpha}$ with inner and outer cut-off radii r_{in} and r_{out},
- Differential grain size distribution $dn(a) \propto a^{-3.5}da$ with lower and upper cut-off size a_{min} and a_{max},
- Two possible grain compositions – pure astronomical silicate (Draine 2003) and a 1:1 mixture of astronomical silicate and ice (Löhne et al. 2011; Augereau et al., in prep.) – to explore the possibility that water ice that might be a significant constituent of debris disk dust is responsible for the peculiar shape of the SEDs.

Since the number of free parameters in the fitting is close to the number of data points used, the fitting is expected to be very degenerate. For the reduced χ^2 (Eq. 5.2), a value of 1.0 is in general desirable in the fitting, if N_{dof} is large. However, in the present case N_{dof} ranges from 1 to 3, where the reduced χ^2 is rather desirable to be as small as possible. Different approaches are used to explore the parameter space in an efficient way and to find parameters that can be fixed, because they have a unique best-fit result or they have no significant effect on the fitting at all. The parameter space explored for each approach is listed in Table 7.3. The fitting results are compiled in Table 7.4. Simulated SEDs from the best-fit models are shown in Fig. 7.1 (final models) and Fig. 7.2 (comparison of the best-fit results for the different approaches). The parameter space explored and the parameters fixed in each approach are motivated by the results of the previous approaches as described in the following.

Approach 1: Exploring the parameter space

In a first approach, a range of free parameters is considered that includes most of the known debris disks. An upper grain size of 1 mm is chosen, large enough to consider any effect of large grains on the fluxes at all wavelengths observed. In any case, if a steep grain size distribution is found (as expected), the flux from even larger grains would only further

Table 7.3: Explored parameter space for the SED fitting (for details see Sect. 7.3).

	Approach 1		Approach 2		
Parameter	Range	# values	Range	# values	distribution
$r_{\rm in}$ [AU]	3 – 100	817	3 – 100	817	temp
$r_{\rm out}$ [AU]	5 – 300	671	5 – 300	671	temp
α	−2.0 – 3.5	56	fixed	1	linear
$a_{\rm min}$ [μm]	0.2 – 20.0	448	0.2 – 20.0	448	logarithmic
$a_{\rm max}$ [μm]	fixed	1	fixed	1	logarithmic
γ	2.0 – 5.0	31	2.0 – 10.0	81	linear
$M_{\rm dust}$ [$M_\odot$]	free	...	free	...	continuous
Composition	0%, 50% ice	2	0%, 50% ice	2	...

	Approach 3		Approach 4		
Parameter	Range	# values	Range	# values	distribution
$r_{\rm in}$ [AU]	3 – 100	817	3 – 100	817	temp
$r_{\rm out}$ [AU]	5 – 300	671	5 – 300	671	temp
α	fixed	1	fixed	1	linear
$a_{\rm min}$ [μm]	0.2 – 20.0	448	0.2 – 20.0	448	logarithmic
$a_{\rm max}$ [μm]	fixed	1	1.0 – 1000.0	674	logarithmic
γ	fixed	1	fixed	1	linear
$M_{\rm dust}$ [$M_\odot$]	free	...	free	...	continuous
Composition	0%, 50% ice	2	0%, 50% ice	2	...

Notes. The abbreviations *temp* for the distribution of values means distributed with equal steps of the dust temperature of the component with the steepest temperature gradient.

increase this slope (Sect. 4.4).

In this approach, 7 free parameters are used ($r_{\rm in}$, $r_{\rm out}$, α, $a_{\rm min}$, γ, $M_{\rm dust}$, and dust chemical composition). This is the largest number possible considering a total of 8 SED measurements. Although strong degeneracies are expected, this approach is used to explore the parameter space without strong initial constraints that might bias the results. Parameters that have a unique solution or that have no significant effect on the fit can be fixed in subsequent approaches.

A very narrow ring structure is found to be the best-fit for all three disks, although the parameters describing the spatial dust distribution are not constrained very well. Furthermore, a very steep grain size distribution with a value for the exponent γ very close to the edge of the explored parameter space (5.0) is found as best-fit for all three SEDs. In the following, it is referred to this as an underabundance of large grains. Since this is an

atypical, but not unexpected result (Sect. 7.2), more effort is put on the evaluation of the significance of this result in the subsequent approaches. As the radial extent of the disks has been found to be narrow, the exponent of the radial surface density distribution is fixed in the further fits to $\alpha = 0.0$ (constant surface density), decreasing the explored parameter space by one dimension. In a narrow ring, this will not have any effect on the SED.

Approach 2: A larger range of possible values for γ

Now, the aim is to obtain a best-fit value for γ that is included in the considered parameter space. A range of possible values for γ of 2.0 to 10.0 is explored. All other parameters (beside α which is now fixed as described above) have the same ranges as in Approach 1. This results in a total of 6 free parameters.

For HIP 107350, the range of explored values of γ seems to be still too small. This is ignored, since such a large very value is not significant (confidence levels: 5.9 ... 10.0). For the other two objects, the value of γ is well within the explored range. The confidence levels of the inner and outer radius suggest that the ring-like shape of the disk is not very significant, even for a constant surface density.

Approach 3: Fixing γ to 3.5

Fixing the value of γ to 3.5 and having a fixed upper grain size of $a_{\max} = 1.0\,\mathrm{mm}$, one can force a fit where the parameters of the grain size distribution are consistent with an equilibrium collisional cascade. The explored ranges of all other parameters are unchanged compared to Approach 2. This results in a total of 5 free parameters.

The resulting χ^2 is much worse (by a factor of 2.5 to 12.6) compared to the results from Approach 2. The changes of the radial position of the dust ring are in line with the expectations from the much lower abundance of small (warm) particles.

Approach 4: Fixed value of $\gamma = 3.5$, but free upper grain size

Another possibility to produce an underabundance of large grains in the model is to let the upper grain size be a free parameter. Since a very steep size distribution and a small upper grain size have comparable results (removing large grains from the model), one can fix the value of γ to 3.5 to be consistent with an equilibrium collisional cascade. The resulting upper grain size is expected to be sufficiently small. This results in a total of 6 free parameters.

This approach gives in general the best χ^2. Upper grain sizes of few tens of micron are found. The low radial extend of the debris ring is again not very significant, but still the best-fit.

Table 7.4: Results from the SED fitting (for details see Sect. 7.3). Confidence levels correspond to $3\,\sigma$ uncertainties of the fitting (Sect. 5.2.2).

Parameter	Best-fit value [$3\,\sigma$ confidence levels]							
	HIP 103389							
	Approach 1		Approach 2		Approach 3		Approach 4	
	Silicate	Mixture	Silicate	Mixture	Silicate	Mixture	Silicate	Mixture
$r_{\rm in}$ [AU]	20.7 [8.5 – 32.2]	20.8 [9.1 – 35.9]	18.2 [7.9 – 24.5]	20.9 [8.0 – 26.6]	11.9 [4.2 – 16.0]	13.6 [4.4 – 19.1]	42.3 [12.9 – 63.3]	22.5 [8.6 – 43.0]
$r_{\rm out}$ [AU]	20.7 [15.3 – 53.1]	20.9 [15.4 – 123.3]	20.0 [16.3 – 65.1]	20.9 [17.3 – 77.3]	12.0 [8.8 – 37.4]	13.6 [10.2 – 38.5]	46.0 [21.3 – 138.5]	22.5 [17.9 – 110.9]
α	0.1 [−2.0 – 3.5]	2.6 [−2.0 – 3.5]	0.0 (fixed)	0.0 (fixed)	0.0 (fixed)	0.0 (fixed)	0.0 (fixed)	0.0 (fixed)
$a_{\rm min}$ [μm]	6.6 [4.7 – 8.6]	9.2 [4.4 – 11.4]	9.5 [7.8 – 10.4]	12.8 [10.7 – 13.6]	6.1 [2.8 – 9.8]	6.6 [2.6 – 12.0]	4.2 [3.1 – 7.8]	9.3 [3.7 – 14.9]
$a_{\rm max}$ [μm]	1000.0 (fixed)	1000.0 (fixed)	1000.0 (fixed)	1000.0 (fixed)	1000.0 (fixed)	1000.0 (fixed)	14.3 [12.7 – 18.1]	22.7 [14.3 – 28.5]
γ	5.0 [4.6 – 5.0]	5.0 [4.5 – 5.0]	7.4 [6.3 – 10.0]	9.0 [6.5 – 10.0]	3.5 (fixed)	3.5 (fixed)	3.5 (fixed)	3.5 (fixed)
$M_{\rm dust}$ [$M_\odot$]	5.95e-11	5.02e-11	3.90e-11	3.87e-11	1.41e-10	1.21e-10	1.46e-10	4.36e-11
$\chi^2_{\rm red}$	4.112	3.664	0.816	0.776	10.277	8.488	0.628	0.760
	HIP 107350							
	Approach 1		Approach 2		Approach 3		Approach 4	
	Silicate	Mixture	Silicate	Mixture	Silicate	Mixture	Silicate	Mixture
$r_{\rm in}$ [AU]	15.3 [3.8 – 28.5]	21.5 [7.4 – 93.0]	29.1 [7.9 – 47.2]	30.6 [5.6 – 44.1]	9.6 [3.0 – 15.6]	10.9 [3.0 – 16.5]	37.1 [4.3 – 54.4]	35.2 [7.2 – 54.2]
$r_{\rm out}$ [AU]	15.9 [9.3 – 227.3]	21.8 [10.3 – 276.6]	31.3 [13.9 – 113.9]	32.3 [16.0 – 138.5]	9.6 [5.8 – 33.0]	11.0 [9.1 – 35.7]	37.4 [19.2 – 187.5]	35.2 [17.4 – 145.3]
α	−0.9 [−2.0 – 3.5]	1.4 [−2.0 – 3.5]	0.0 (fixed)	0.0 (fixed)	0.0 (fixed)	0.0 (fixed)	0.0 (fixed)	0.0 (fixed)
$a_{\rm min}$ [μm]	5.9 [4.7 – 9.0]	5.9 [4.3 – 9.1]	6.9 [2.7 – 10.9]	8.2 [3.6 – 10.7]	5.7 [4.8 – 11.0]	5.8 [4.9 – 11.7]	7.8 [1.6 – 10.4]	9.6 [2.2 – 13.5]
$a_{\rm max}$ [μm]	1000.0 (fixed)	1000.0 (fixed)	1000.0 (fixed)	1000.0 (fixed)	1000.0 (fixed)	1000.0 (fixed)	7.8 [6.3 – 13.3]	9.6 [6.4 – 17.4]
γ	5.0 [4.0 – 5.0]	5.0 [4.0 – 5.0]	10.0 [6.0 – 10.0]	10.0 [5.9 – 10.0]	3.5 (fixed)	3.5 (fixed)	3.5 (fixed)	3.5 (fixed)
$M_{\rm dust}$ [$M_\odot$]	1.37e-11	1.81e-11	3.33e-11	2.79e-11	3.15e-11	2.73e-11	4.63e-11	3.24e-11
$\chi^2_{\rm red}$	7.048	5.672	1.652	1.568	4.229	3.869	1.528	1.488
	HIP 114948							
	Approach 1		Approach 2		Approach 3		Approach 4	
	Silicate	Mixture	Silicate	Mixture	Silicate	Mixture	Silicate	Mixture
$r_{\rm in}$ [AU]	12.8 [6.8 – 13.9]	13.6 [6.8 – 14.5]	12.8 [7.1 – 13.7]	13.5 [7.8 – 14.9]	12.7 [5.5 – 16.6]	14.0 [7.9 – 19.1]	32.5 [9.0 – 40.1]	13.3 [8.4 – 14.5]
$r_{\rm out}$ [AU]	12.8 [12.1 – 39.8]	13.8 [12.9 – 34.7]	12.8 [12.1 – 23.2]	13.8 [12.9 – 24.9]	12.7 [10.5 – 25.6]	14.1 [11.0 – 30.8]	34.5 [26.9 – 81.4]	13.8 [12.9 – 22.9]
α	2.9 [−2.0 – 3.5]	0.0 [−2.0 – 3.5]	0.0 (fixed)	0.0 (fixed)	0.0 (fixed)	0.0 (fixed)	0.0 (fixed)	0.0 (fixed)
$a_{\rm min}$ [μm]	9.6 [8.9 – 10.2]	12.9 [11.9 – 13.8]	9.6 [8.9 – 10.2]	12.9 [11.9 – 13.8]	6.4 [3.6 – 9.9]	7.4 [3.0 – 11.7]	3.2 [2.6 – 4.6]	11.8 [10.7 – 13.1]
$a_{\rm max}$ [μm]	1000.0 (fixed)	1000.0 (fixed)	1000.0 (fixed)	1000.0 (fixed)	1000.0 (fixed)	1000.0 (fixed)	24.2 [10.0 – 27.3]	43.8 [10.0 – 53.2]
γ	4.7 [4.5 – 5.0]	4.7 [4.4 – 5.0]	4.7 [4.4 – 5.2]	4.7 [4.4 – 5.1]	3.5 (fixed)	3.5 (fixed)	3.5 (fixed)	3.5 (fixed)
$M_{\rm dust}$ [$M_\odot$]	6.58e-11	6.49e-11	6.57e-11	6.49e-11	2.64e-10	2.21e-10	1.78e-10	4.83e-11
$\chi^2_{\rm red}$	0.568	0.464	0.284	0.232	3.291	2.333	0.132	0.232

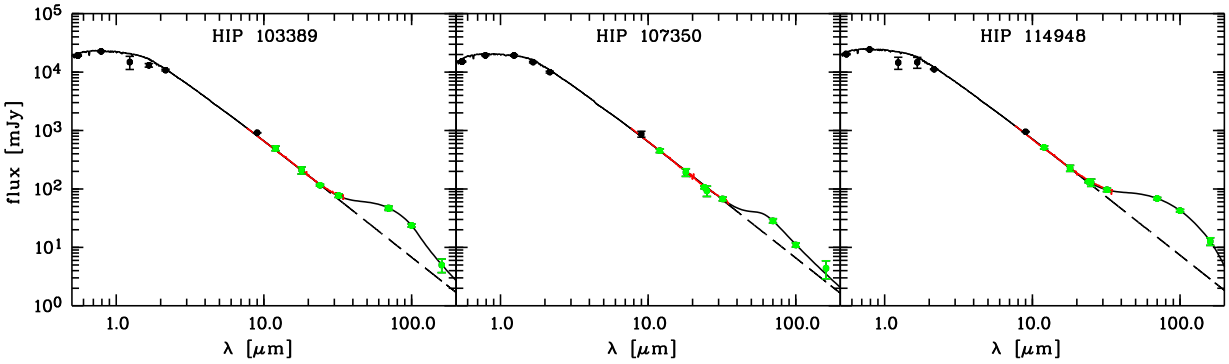

Fig. 7.1: Final models from the SED fitting. The modeled SEDs for the three disks are computed from the results of Approach 4 using pure astronomical silicate (Sect. 7.4).

7.4 Results

The general results and conclusions that can be drawn from the fitting approaches are summarized as follows:

- Values of $\gamma = 4.7$ to 10.0 or a small upper grain size are found rather than the expected value of $\gamma \approx 3.5$ and a reasonably large $a_{\max}$. Models with $\gamma = 3.5$ do not reproduce the observed SEDs in a reasonable way. It is not reasonably affected by any modeling degeneracies found (that are included in the estimate of the uncertainties).
- Evidence is found for a large lower grain size of the dust compared to the expected blow-out size of the systems (0.5 μm to 0.9 μm). However, the lower grain size depends very much on the approach used. Earlier studies of debris disk SEDs had similar results (e.g., HD 107146; Roccatagliata et al. 2009) that have been at least mitigated and partially

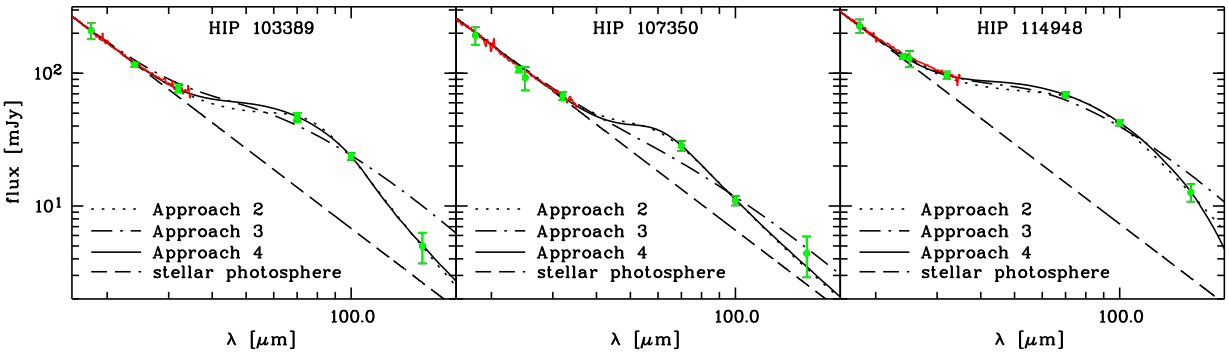

Fig. 7.2: Comparison between the best-fit results from the different approaches. The SEDs are modeled from the best-fit result of each approach using pure astronomical silicate, since no evidence for ice inclusion is found. The results from Approach 1 are not included, since the best-fit results are found not to be in the explored range of parameters in this approach.

attributed to modeling degeneracies in pure SED fitting after including resolved data in the fitting process (Ertel et al. 2011; Chapt. 6 of the present work). Thus, this result has to be treated with caution.

- The dust in all three disks must be located at a distance from the star of no more than a few tens of AU as can be concluded from the modeling results and the fact that the disks are spatially unresolved in the PACS images. Stronger constraints on this value are not possible due to degeneracies in the modeling.
- The disks appear to be narrow rings. However, the uncertainties – in particular of the outer disk radius – are very large and also very broad disks can result in fits on the SED that fall within the derived $3\,\sigma$ confidence levels. This can only partly be excluded by the additional constraint that the disks are spatially unresolved.

Each approach presented results in a different set of best-fit parameters and a different χ^2, while the results can be interpreted in a consistent way. To find from the fitting results a final model of each disk, the following selection is applied:

- Approach 1 has to be ruled out, because the best-fit parameters from this approach are close to the edge of the explored parameter space.
- In general, the SEDs cannot be fitted by a grain size distribution that includes a significant amount of large grains (Approach 3).
- The results from Approach 2 (free γ, $a_{\mathrm{max}} = 1.0\,\mathrm{mm}$) and Approach 4 (free a_{max}, $\gamma = 3.5$) are consistent, while the results from Approach 4 and pure silicate represent in general the best fit to the data. Thus, these results are considered as the best-fit models from the fitting.

From these final models, one finds dominating dust temperatures (the temperature of the smallest grains that dominate the emission) of 63 K, 50 K, and 73 K for HIP 103389, HIP 107350, and HIP 114948.

7.5 Discussion

7.5.1 The origin of the dust

From the modeling, one finds strong evidence for an underabundance of large grains expected to be present in the disk from common scenarios for the dust production. These are the first debris disks discovered that exhibit such a peculiar shape of the SED in the wavelength regime of $70\,\mu\mathrm{m}$ to $160\,\mu\mathrm{m}$. All this suggests that these objects are exceptions from the common understanding of dust creation in debris disks. On the other hand, six more disks with a similar shape of the SED have recently been identified in the ongoing DUNES survey, which might suggest that this phenomenon is common among low-mass debris disks. The fact that the disks are very faint (Table 7.5) might imply that we are faced with a new class of debris disks not revealed earlier due to limited sensitivity in the

relevant wavelength range. In the following, scenarios are discussed that might be capable to explain the steep decrease of the three SEDs.

Scenario 1: Significant deviation from the conditions required for an equilibrium collisional cascade

For the equilibrium collisional cascade, a number of assumptions are made that are not necessarily valid in debris disks due to the effects of radiation pressure and Poynting-Robertson drag (Wyatt et al. 2011; Sect. 2.2.3 of the present work). For the massive debris disks known so far, this is expected to be negligible (Wyatt 2005). One can estimate the ratio between collisional time scale and Poynting-Robertson time scale (Eqs. 2.31 and 2.29) for the three disks to $10^{-2} \ldots 10^{-3}$. However, the disk models used (best-fit from Approach 4, pure silicate) represent very narrow rings, which is not a significant fitting result. Assuming a ring with a width of 10 AU starting at the inner radius found from the fitting, one finds $t_{\mathrm{coll}}/t_{\mathrm{PR}} = 3 \times 10^{-2} \ldots 5 \times 10^{-2}$. It is not possible to put strong constraints on the dust dynamics due to the crude estimate of the time scales and the fact that the disks are in a critical regime of $t_{\mathrm{coll}}/t_{\mathrm{PR}} \sim 1$, but it is expected that transport mechanisms are not negligible in the dust dynamics of these disks.

Scenario 2: Different chemical composition or physical shape of the dust grains than the assumed one

One might imagine a dust composition emitting significantly more efficiently than astronomical silicate or ice in the wavelength range of 70 μm to 100 μm compared to longer wavelengths. Therefore, one would need grains with a break in $Q_{\lambda}^{\mathrm{abs}}(a)$ (Sect. 7.2) at shorter wavelengths (in particular for large grains). Also, if the large grains were significantly colder than expected, their emission would be reduced. This would both allow a significantly larger amount of large grains to be present in the systems than modeled.

Voshchinnikov et al. (2006) simulated the effect of porosity on the absorption efficiency of dust grains. They found that the temperature of dust grains at a given distance from a star decreases significantly with increasing porosity. If one now has small, compact grains and larger, porous grains, the difference in temperatures of the smaller and larger grains can be increased significantly. This would be the case, if the large grains producing the smaller ones through collisions were porous, composed of smaller, compact units in the order of the lower grain size derived from the modeling of the three systems (i.e., 5 μm to 10 μm). Smaller grains produced through collisions would then be compact. This might also be able to explain why the derived lower grain size is significantly larger than the blow-out size. Small, compact grains are expected to be more robust against destruction through collisions. Thus, fewer even smaller particles would be produced resulting in a break in the grain size distribution.

Table 7.5: Simulated observational properties of the disks derived from the final models.

Source	$L_{\rm dust}/L_\star$	$(F_{\rm dust}/F_\star)_{0.6\,\mu{\rm m}}$		$(F_{\rm dust}/F_\star)_{1.1\,\mu{\rm m}}$	
		face-on	edge-on	face-on	edge-on
HIP 103389	1.5×10^{-5}	1.1×10^{-6}	1.9×10^{-4}	1.3×10^{-6}	1.8×10^{-4}
HIP 107350	0.6×10^{-5}	4.9×10^{-7}	7.4×10^{-6}	5.5×10^{-7}	1.3×10^{-5}
HIP 114948	2.5×10^{-5}	2.1×10^{-6}	3.4×10^{-4}	2.6×10^{-6}	3.3×10^{-4}

Scenario 3: A shepherding planet

As described in Sect. 2.2.2, planets can trap dust particles into mean-motion resonances. This results in a barrier against particles moving inwards due to Poynting-Robertson drag. This barrier is less efficient for very small grains for which Poynting-Robertson drag is very strong (Reidemeister et al. 2011). On the other hand, very large grains and planetesimals (very small β) are not significantly affected by Poynting-Robertson drag (Eq. 2.29).

The dust seen in these disks might be produced in a faint, transport dominated debris disk further away from the star, too faint and too cold to be detected in the available data. The small particles (few tens of micron and smaller) would then be dragged inwards by Poynting-Robertson drag. A possible planet present further inwards in the system should trap the particles into resonance. This would result in an accumulation of particles with a very distinct range of sizes, which would explain both the lack of large grains (at least in an abundance and at a position where they would be detectable) and the lack of small grains. Such a "dust trail" has been observed, e.g., to be associated with our Earth and has been modeled to predominantly consist of grains of $\approx 12\,\mu$m and larger (Dermott et al. 1994). This scenario will have to be investigated through detailed collisional and dynamical modeling (e.g., Reidemeister et al. 2011).

7.5.2 Observational perspectives

With the present data, it is not possible to put strong constraints on most of the disk properties, in particular the radial distribution of the dust. Thus, the conclusions from these data are very limited. Further observations with present and near future instruments can help to reasonably increase our understanding of these peculiar debris disks. In the following, the potential of different observational techniques for giving further constraints on the three disks is discussed briefly. For a description of the techniques see Chapt. 3.

- Since the most extended models of the three disks predict radial extents of only $\approx 2\farcs2$, these objects are at the edge of what is resolvable with *coronagraphy*. Furthermore, the disks are very faint in scattered light (Table 7.5). It is important to note that in the case of edge-on orientation most of the flux comes from forward scattering and will then

be concentrated close to the star (projected physical separation) with no contribution to the signal in coronagraphic observations. A contrast ratio of $< 10^{-6}$ is not accessible to present instruments.

- Successful *optical/near-infrared imaging of planetary companions* would give strong evidence that Scenario 3 (shepherding planet) is responsible for the peculiar shape of the disk. Determining the position of this planet would also help to further constrain the position of the dust in this scenario. The youth of the stars means good chances to directly image giant planets at separations of $\geqslant 1''$ from the star with present methods (e.g., Marois et al. 2010). A search for Jupiter mass companions around the three stars (PI: A. Bayo) has been proposed for the next ESO observing period (P89, Apr. 1st 2012 to Sept. 30th 2012).
- The predicted extents of the disks are in a range easily resolvable with *ALMA*. However, the disks are already very faint at PACS wavelengths and the expected surface brightness is decreasing particularly steep towards wavelengths accessible with ALMA. It is not clear, whether ALMA observations are sensitive enough to detect these disks. On the other hand, even upper limits on the disk flux at (sub-)mm wavelengths in the sensitivity range reachable are expected to provide useful further constraints on the shape of the SEDs.
- Further *photometry and spectroscopy in thermal reemission* would help to constrain the radial distribution of the dust and the size distribution of the small grains (wavelengths between $40\,\mu$m and $70\,\mu$m) and the steep slope and the shape of the SEDs at longer wavelengths ($\lambda > 70\,\mu$m). *Herschel*/SPIRE is not sensitive enough to detect the disks at $\lambda = 250\,\mu$m or longer. PACS spectroscopy in the range of $50\,\mu\text{m} < \lambda < 200\,\mu$m requires integrations in the order of few hours to detect the disks with sufficient SNR. The Stratospheric Observatory for Infrared Astronomy (SOFIA) is most promising to provide observational capabilities in the relevant wavelength regime in the near future.

7.6 Conclusions

The first data at wavelengths $> 70\,\mu$m for the three debris disks discussed in this chapter have been presented and modeled. All three sources potentially exhibit an unusually steep decrease of the SED in the wavelength range between $70\,\mu$m and $160\,\mu$m. In a general discussion, it has been shown that this peculiar shape of the SED is an indicator for a deviation from the case of an equilibrium collisional cascade. Modeling implies that the thermal emission from these disks is dominated by a very distinct grain size regime of several micron to few tens of micron. The disks have been modeled as narrow rings with a significant underabundance of large grains. A number of explanations for the unusually steep shape of the SEDs have been discussed. However, it has also been shown that the understanding of faint source photometry obtained with *Herschel* is still incomplete and that the results presented here depend very much on the actual version of the data reduction pipeline. Six more candidates for this new class of debris disks have been identified so far

from the ongoing DUNES survey. This is the first published discovery of debris disks that exhibit such a peculiar shape of the SED in this wavelength regime.

8 Herschel/DUNES modeling of spatially resolved debris disks

One of the most important advancements of *Herschel* compared to previous space-based far infrared facilities is its high spatial resolution. In this chapter, the modeling of spatially resolved *Herschel* data of two debris disks around solar-type stars, q^1 Eridani and HD 207129, obtained in the context of DUNES are presented. Strong emphasis is put on the modeling carried out in the context of the present work. For details about the observations, data reduction and analysis, as well as modeling provided by other groups within the DUNES team, see the corresponding publications (q^1 Eri: Liseau et al. 2010; Löhne et al. 2011; HD 207129: Marshall et al. 2011; Augereau et al., in prep.).

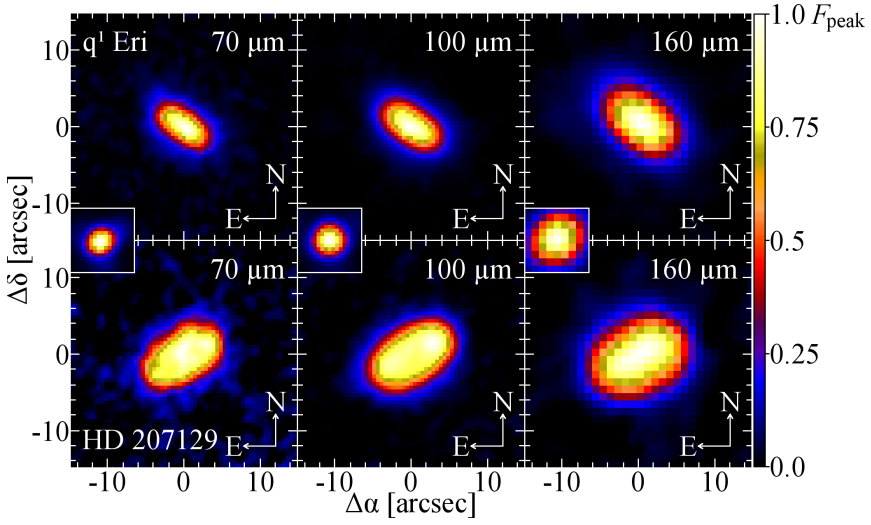

Fig. 8.1: *Herschel*/PACS images of q^1 Eri (*top*) and HD 207129 (*bottom*). Corresponding PACS scan map PSFs are shown between the images of the two sources to illustrate the spatial resolution. The 70 μm chop-nod PSF (for the q^1 Eri image at this wavelength) does not differ significantly from the scan map PSF in the scale shown. Pixel scales are 1″ at 70 μm and 100 μm and 2″ at 160 μm. All images are displayed in a linear stretch from 0 to peak height. See Fig. 8.2 for radial profiles with absolute flux numbers.

Table 8.1: Observational results for q^1 Eri and HD 207129.

Source	q^1 Eri	HD 207129
Spectral Type	F8 V	G2 V
Teff [K]	6155	5912
$L_\star$ $[L_\odot]$	1.57	1.26
Distance d [pc]	17.4	16.0
Age estimates (range) [Gyr]	0.3 . . . 6.3	1.5 . . . 3.2
HIPE version	4.2	2.0.0_RC3
$F_{70\,\mu m}$	828 ± 83	288 ± 28
$F_{100\,\mu m}$	810 ± 81	311 ± 36
$F_{160\,\mu m}$	537 ± 107	211 ± 42
$F_{250\,\mu m}$	324 ± 97	113 ± 18
$F_{350\,\mu m}$	143 ± 43	44 ± 9
$F_{500\,\mu m}$	59 ± 18	26 ± 8
$\mathrm{FWHM}_{100\,\mu m}$ [″]	15.1×8.8	29.6×17.0
i_{min} [°]	54	53
$\mathrm{PA}_{100\,\mu m}$ [°]	56	122

Notes. The uncertainties on the photometry include both measurement and calibration uncertainties. The FWHM and PA (major axis, East of North) at 100 μm are given as a reference. The quantity i_{min} is the lower limit on the inclination from face-on as derived from the FWHM ratio at 100 μm. For details and references see Liseau et al. (2010); Marshall et al. (2011); Löhne et al. (2011).

8.1 Summary of data reduction and analysis

The observations of both q^1 Eri and HD 207129 are carried out with *Herschel*/PACS in mini-scan map mode and with *Herschel*/SPIRE in small map mode (beside the 70 μm observations of q^1 Eri carried out in chop-nod mode). This results in a wavelength coverage of *Herschel* observations of the two targets ranging from 70 μm to 500 μm. The resulting *Herschel*/PACS images of both targets are shown in Fig. 8.1. The sources are clearly detected in all images. Data reduction is done in HIPE (Ott et al. 2010). Stellar properties are estimated using a PHOENIX/GAIA synthetic stellar model (Brott & Hauschildt 2005). The stellar properties and observational results for the two targets are summarized in Table 8.1.

The disk center and position angle are derived fitting rotated ellipses on the images. With these information known, one can extract radial profiles. Therefore, the images are rebinned by a factor of 10 via a cubic convolution interpolation. The profiles are then extracted along the axes of the disk with a step width of one native pixel (10 sub-pixel) by averaging over two 11×11 sub-pixel wide boxes (one for each side at the same distance

from the disk center). The standard deviation of these sub-pixels is computed and added quadratically to the background fluctuation in the images to derive the uncertainty of each measurement. Profiles of the PSF are derived from images of a PSF reference star (α Boo, scaled to the flux of q^1 Eri and HD 207129, respectively) via azimuthal averaging. Uncertainties of these profiles are negligible due to the much higher SNR compared to the observations of the science targets. The SEDs and radial profiles together with the best-fit models on the data (see below) are shown in Fig. 8.2.

8.2 Modeling

Compared to the modeling of HD 107146 (Chapt. 6), there are a number of significant differences due to the different nature of the spatially resolved data available (thermal reemission in the present chapter, scattered light for HD 107146):

- The spatial resolution of the data considered in the present chapter is significantly lower. Thus, these data put significantly weaker constraints on the radial dust distribution than the scattered light data in Chapt. 6.
- In thermal reemission, the surface brightness profile depends on the radial temperature profile and, thus, on the grain properties (not only proportional to the distance from the star like in scattered light). Thus, a separation of the fitting problem like in Chapt. 6 is not possible. This results in a larger, more complex parameter space to be searched.
- The same process (thermal re-emission) is responsible for the emission observed in the spatially resolved data and the SED considered in the present chapter. This allows one completely simultaneous model fitting.

As a consequence, the approach developed in Chapter 6 cannot be employed, but `SAnD` (Sect. 5.2.2) can be used for simultaneous model fitting to the data (SED and radial profiles).

The same model for the radial density distribution and grain size distribution as in the previous chapter (Sect. 7.3) is used, but other ranges of the parameters are explored (Table 8.2). The best-fit parameters and uncertainties are listed in Table 8.3. Both disks are additionally modeled with `GRaTeR` (Augereau et al. 1999) using a grid search method. This is done within the DUNES team (J.-C. Augereau, personal communication) and is not part of the present thesis. However, the results are listed in Table 8.3 along with the `SAnD` results for comparison. While for HD 207129 a unique solution is found, two distinct solutions are found for q^1 Eri – one with outwards increasing and one with outwards decreasing surface density – both of which result in comparably good χ^2 (Table 8.3). The solution with outwards decreasing surface density gives a slightly worse χ^2 and is not found as a fit in most of the `SAnD` runs. Thus, two different kinds of runs (with different parameter spaces searched) are employed. While a first sequence (Seq. 1) of runs considers a very large range of parameters, an outwards decreasing surface density is enforced in a second sequence (Seq. 2) to enforce the solution in this range of the parameter space (Table 8.2).

Table 8.2: Explored parameter space for q^1 Eri and HD 207129 using SAnD.

	q^1 Eri			HD 207129		
Parameter	Range 1	Range 2	#	Range	#	distribution
$r_{\rm in}$ [AU]	3 – 70	10 – 100	695/350	40 – 150	120	temp
$r_{\rm out}$ [AU]	150 – 350	600	75/fixed	70 – 500	115	temp
α	−2.0 – 2.5	4.5 – 0.0	46	−4.5 – −1.5	56	lin
$a_{\rm min}$ [μm]	0.5 – 20.0	0.5 – 20.0	360	0.5 –10.0	292	log
$a_{\rm max}$ [μm]	1000	1000	fixed	1000	fixed	log
γ	2.5 – 4.5	2.5 – 4.5	21	2.5 – 4.5	21	lin
$M_{\rm dust}$	free	free	...	free	...	cont
$V_{\rm ice}/(V)$ [%]	0, 50	0, 50	2	0, 50	2	...
i [°]	65 – 90	65 – 90	21	0 –90	21	cos

Notes. Range 1 and Range 2 refer to the two different fits on q^1 Eri (Seq. 1 and Seq. 2, see Sect. 8.2 for details). # means the number of values used to sample the range of parameters explored. Abbreviations for the distribution of values are: *temp* – distributed with equal steps of the dust temperature of the component with the steepest temperature gradient, *lin* – linearly distributed, *log* – logarithmically distributed, *cont* – continuous, *cos* – equally distributed in cos(i).

8.2.1 Results

The fitting results are listed in Table 8.3. Differences in the results from SAnD and GRaTeR can be attributed to differences in the fitting approaches (Löhne et al. 2011; Augereau et al., in prep.). Both disks are found to be significantly extended radially. While for q^1 Eri the exponent of the grain size distribution is consistent with an equilibrium collisional cascade, the distribution for HD 207129 is slightly steeper. For HD 207129, the lower grain size is found to be slightly larger than the expected blow-out size of the system for compact dust grains (0.5 μm to 1.0 μm, depending on the chemical composition of the dust). The values for q^1 Eri are consistent with the expected blow-out size.

8.3 Discussion

The fitting of both disks gives a rather surprising result: an outwards increasing surface density. While for HD 207129 this result is unique, for q^1 Eri a second result, more in line with the expectations is found to have only slightly worse χ^2.

The solution for HD 207129 is consistent with the available HST scattered light data (Krist et al. 2010; Löhne et al. 2011), but only the *Herschel* data reveal the unusual surface density profiles. The outwards increasing surface density as well as the large lower grain size in this disk can be explained through collisional modeling (Löhne et al. 2011). A low

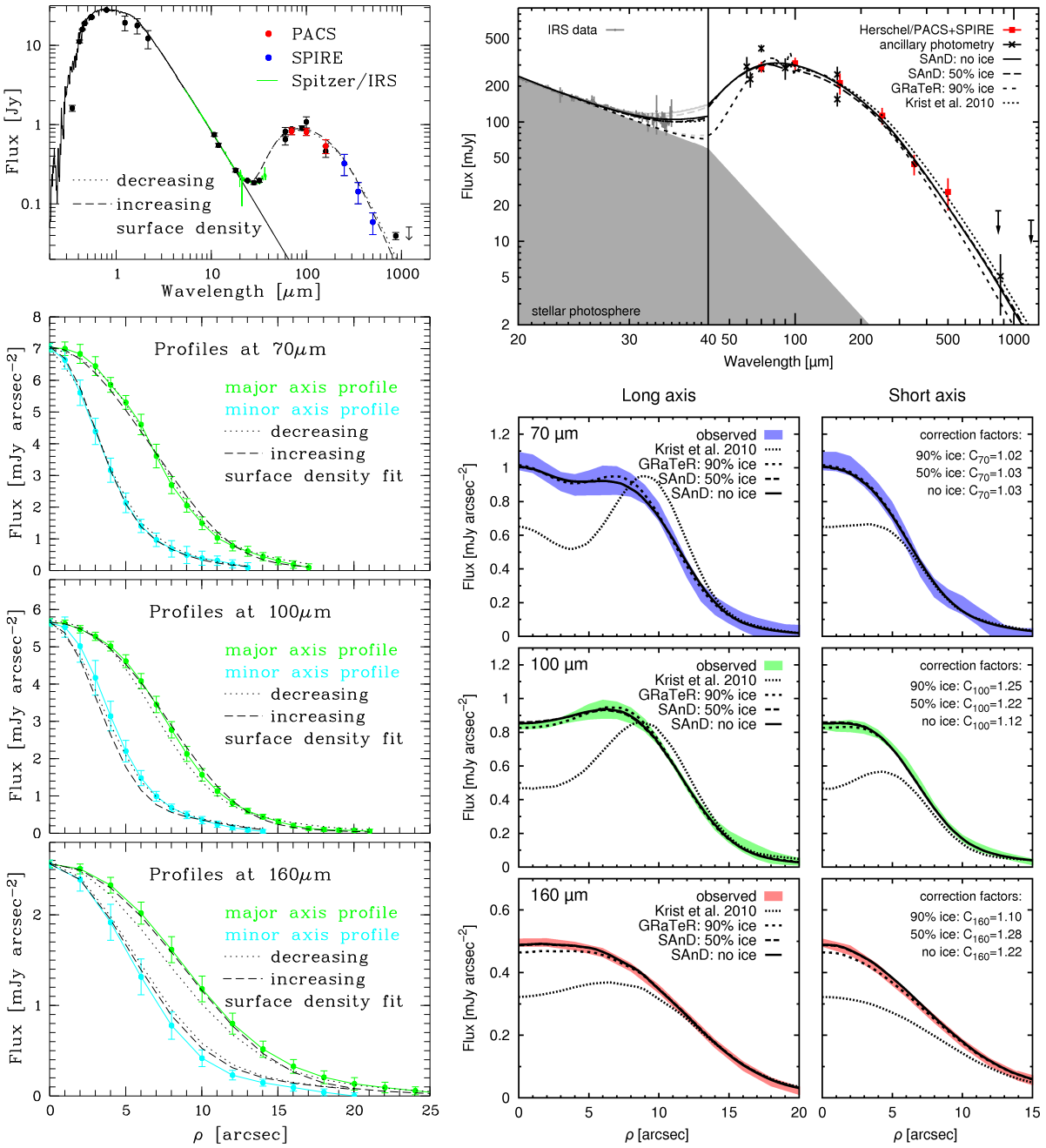

Fig. 8.2: SED, radial profiles, and best-fit models for q[1] Eri (*left*) and HD 207129 (*right*). Radial distances in AU and arcseconds can be converted into each other using the distances of the systems (Table 8.1). For q[1] Eri, the best fit models for outwards increasing (Seq. 1) and outwards decreasing (Seq. 2) surface density are shown (see Sect. 8.2.1 for details). For HD 207129, different results from `SAnD` and `GRaTeR` are shown. Furthermore, the best-fit to the HST data and the SED from Krist et al. (2010) is shown for comparison. Parts of the HD 207129 disk were not covered by the slit of *Spitzer*/IRS (too extended), resulting in some missing flux in the spectrum. Thus, in the range of this spectrum the total model flux (light gray) and the flux corrected for the slit width (black) are shown in the SED. The plots for HD 207129 are taken from Löhne et al. (2011).

Table 8.3: Fitting results for q^1 Eri and HD 207129.

	q^1 Eri			HD 207129	
Parameter	SAnD (Seq. 1)	SAnD (Seq. 2)	GRaTeR	SAnD	GRaTeR
$r_{\rm in}$ [AU]	$3.9^{+4.1}_{-0.9}$	$53.2^{+27.9}_{-1.0}$	$75.9^{+1.3}_{-1.6}$	$57.3^{+39.4}_{-17.0}$	$r_{\rm sub}{}^{(1)}$
$r_{\rm out}$ [AU]	$183.5^{+16.5}_{-22.4}$	$600^{(2)}$	$600^{(2)}$	$193.6^{+71.2}_{-30.7}$	$166.0^{+17.0}_{-13.0}$
α	$-1.2^{+0.2}_{-0.5}$	$1.8^{+0.7}_{-0.7}$	$2.5^{+0.2}_{-0.3}$	$-2.2^{+2.7}_{-2.0}$	$-3.5^{+0.5}_{-0.3}$
$a_{\rm min}$ [μm]	$1.8^{+0.8}_{-0.7}$	$1.0^{+0.2}_{-0.8}$	$1.3^{+0.2}_{-0.2}$	$2.8^{+3.8}_{-1.3}$	$7.5^{+1.3}_{-2.8}$
γ	$3.5^{+0.1}_{-0.2}$	$3.4^{+0.2}_{-0.1}$	$3.5^{+0.1}_{-0.1}$	$3.8^{+0.4}_{-0.5}$	$4.2^{+0.2}_{-0.2}$
$M_{\rm dust}$ [$M_\odot$]	8.7×10^{-8}	1.2×10^{-7}	9.9×10^{-8}	2.2×10^{-8}	2.6×10^{-8}
$V_{\rm ice}/(V)$ [%]	50^{+0}_{-50}	50^{+0}_{-50}	40^{+7}_{-6}	50^{+0}_{-50}	90^{+0}_{-4}
i [°]	$82.2^{+2.3}_{-10.7}$	$85.4^{+4.6}_{-1.1}$	71^{+1}_{-3}	$56.6^{+9.8}_{-7.1}$	$60^{(2)}$
$\chi^2_{\rm red}$	1.24	1.60	1.44	0.77	1.26

Notes. The GRaTeR results are shown for comparison. Uncertainties for the SAnD results correspond to $3\,\sigma$ as described in Sect. 5.2.2. Uncertainties for the GRaTeR results correspond to $1\,\sigma$ derived from a Bayesian analysis (Löhne et al. 2011; Augereau et al., in prep.). $^{(1)}$ Parameter fixed to sublimation radius. $^{(2)}$ Fixed value.

dynamical excitation of the dust and planetesimals is found to allow one to reproduce the observed and modeled appearance of the disk. As a consequence, collisions are found to be less effective and to play a smaller role in this disk compared to other known debris disks of similar mass and brightness. Transport mechanisms due to Poynting-Robertson drag are expected to significantly contribute to the dust dynamics in this disk.

For q^1 Eri, the solution with an outwards increasing surface density is inconsistent with the scattered light data (unpublished, K. Stapelfeldt, personal communication). As a consequence, the "classical" result with an outwards decreasing surface density but a slightly worse χ^2 is the preferable model for this disk. The most likely explanation for two results such different but with comparable quality of the fit is a more complex system present than can be described well by the simple power-law approach. A broad ring with a significant amount of dust inside and outside the peak of the radial surface density distribution, or a multi-ring structure with an inner dust ring of low mass (similar to HD 107146, Chapt. 6; also similar to our Solar System) might be fitted equally well by an outwards increasing (inner regions) and an outwards decreasing power-law (outer regions). Only future, high spatial resolution observations as possible with ALMA can clearly reveal such a structure in the q^1 Eri disk. ALMA observations for this disk have been simulated, but the limited sensitivity of ALMA during Early Science observations[1] is found to be too low to detect the disk at reasonable SNR.

[1] http://almascience.eso.org/call-for-proposals

9 Detectability of debris disks with ALMA

Detailed modeling of available data of debris disks has been carried out in the previous chapters. While important new insights in the disks modeled are gained, it is also demonstrated that only high spatial resolution imaging of the dust distribution can result in a comprehensive model of a debris disk. In particular at (sub-)mm wavelengths, such observations were only possible for a very limited number of bright, nearby debris disks. In the near future, the Atacama Large Millimeter/submillimeter Array (ALMA) will become available, which is expected to significantly increase sensitivity and spatial resolution of the data in this wavelength range. ALMA recently started Early Science observations with a limited number of antennas and array configurations. Once finished, this interferometer will be composed of 50 12-m antennas in an array with maximum baselines of $\approx 16\,\mathrm{km}$. In addition, 12 7-m antennas form the Atacama Compact Array (ACA) will be used to enhance imaging capabilities for extended sources. ALMA is a very complex instrument, providing the user with multiple options that allow one to optimize the instrument set up for the planned observations. A detailed study of the performance of each configuration is necessary to optimize the observational outcome and efficiency. Such a study in the context of spatially resolved observations of debris disk is described in the present chapter. The model and approach used to produce simulated images of debris disks are presented in Sect. 9.1. The simulation of ALMA observations and the estimation of sensitivity from the simulated images are described in Sect. 9.2 and results and conclusions are presented in Sect. 9.3.

9.1 Model description

All simulations are carried out for a debris disk around a solar-type star (realized as a black body radiator with $R_\star = R_\odot$, $L_\star = L_\odot$, $T_\mathrm{eff} = 5778\,\mathrm{K}$). A simple, analytical disk model is used to keep the results as general as possible. It consists of a circular ring ($r_\mathrm{out} = 1.1\,r_\mathrm{in}$) of dust with constant surface density[1] and an opening angle of 10°. Astronomical silicate with a bulk density of $2.7\,\mathrm{g/cm^3}$ (Draine & Lee 1984; Weingartner & Draine 2001) is employed for the chemical composition of the dust. The grain size distribution follows a power-law distribution with lower cut-off size $a_\mathrm{min} = 0.45\,\mu\mathrm{m}$ (i.e., the blow-out size of the system)

[1] This is similar to the width of a ring of dust particles on orbits with identical major axis and eccentricity of 0.1, if the directions of the major axes of the orbits are distributed randomly within the plane of the disk.

and upper cut-off size $a_{\max} = 2\,\mathrm{mm}$. An upper cut-off size is chosen being faced with the problem described in Sect. 4.4, since this is a common approach in the literature and, thus, the results are better comparable to the disk models produced by other groups. Furthermore, Eq. 4.3 can be used to correct for the errors introduced or to convert the results to any different upper cut-off size. The inner disk radius is set to 5 AU, 50 AU, and 100 AU in different runs. This covers a variety of known debris disks, e.g., our Solar System, ϵ Eri (Greaves et al. 1998; Backman et al. 2009), HD 107146 (Ardila et al. 2004; Corder et al. 2009; Ertel et al. 2011; Chapt. 6 of the present work), Fomalhaut (Kalas et al. 2005), and AU Mic (Augereau & Beust 2006). The dust mass of the disk is set to $10^{-8}\,M_\odot$ for simulating the model images and scaled to different masses later (assuming an optically thin debris disk) to evaluate the sensitivity. These masses can be converted into fractional luminosities following the equation[2]:

$$\frac{L_\mathrm{d}}{L_\star} = 4.5 \times 10^7 \left(\frac{r}{\mathrm{AU}}\right)^{-2} \left(\frac{M_\mathrm{dust}}{M_\odot}\right), \tag{9.1}$$

i.e., the dust luminosity for a given dust mass and stellar luminosity scales with r^{-2} and is proportional to the dust mass, where 4.5×10^7 is the factor for $r = 1\,\mathrm{AU}$ given the above model of the system (stellar properties and disk properties). The resulting in factors are 1.8×10^6, 1.8×10^4, and 4.5×10^3 for the disk models with $r_\mathrm{in} = 5\,\mathrm{AU}$, 50 AU, and 100 AU.

The tool `debris` is used to simulate images from the above disk model. Simulations are performed for face-on and edge-on orientation of the disk. The images have an extent of 303 pixel in both directions. The disk is centered on the image, with a total extent ($2\,r_\mathrm{out}$) of 101 pixel. The pixel resolution of the images in AU can then be computed as $2\,r_\mathrm{out}/101$ and in arcseconds by dividing the result by the distance of the system in pc. Different distances are assumed to simulate observations, see Sect. 9.2). In cases where the total extent of the images as described above is smaller than five times the resolution element (FWHM) of the observations (in particular for the models with $r_\mathrm{in} = 5\,\mathrm{AU}$ at large distance and small array extent), the background fluctuation cannot be quantified in a reliable way. Thus, the resolution of the images is lowered in these cases and the empty region around the disk image is increased. This is done dynamically, so that the pixel resolution is 1/20 of the FWHM and the total extent of the images is 200 pixel ($10 \times$ FWHM of each observation).

9.2 Simulation of observations

The procedure `simdata` of the CASA ALMA simulator[3] is used to simulate observations on the model images. For a detailed explanation of all parameters used in this procedure

[2] In addition to the square of the distance from the star (i.e., the intercepted stellar power per cross section), the total luminosity of a given dust species only depends on the stellar spectrum, the total surface of the dust ($\propto$ dust mass), and its absorption efficiency, assuming thermal equilibrium (no information about the wavelength range is carried in which the majority of this luminosity is emitted, i.e., about the dust temperature).

[3] http://casa.nrao.edu/

see the corresponding manuals[4]. The simulations are done using the configurations of the ALMA array in full operations provided by the CASA simulator (using only every second configuration from configurations 01 to 27). These array configurations contain 50 12-m antennas each. The baseline ranges of the array configurations used are listed in Table 9.1. Bands 10, 7, 6, and 5 (central wavelengths of 350 μm, 950 um, 1250 μm, and 1600 μm)[5] are used. The exact central wavelength of each bandpass is chosen to avoid strong atmospheric absorption bands. The band width used is 7.5 GHz for all simulations following the ALMA Cycle 0 Technical handbook[5]. The objects are placed at an optimal position in the sky reaching the zenith during observations (RA = 18^{h}, DEC = $-23°$). Total observing time is 8 h, while the single integration time is 60 s. Thermal noise and phase noise are added to the simulated visibilities. Good, but realistic weather conditions are assumed (precipitable water vapor = 0.65 mm, ground temperature = 269 K). For image reconstruction, natural weighting of the visibilities is applied. Deconvolution is performed with 500 iterations and a threshold of 0.01 mJy/beam. Single pointing observations are simulated rather than mosaicking, since most of the simulated images fit into one field of view of a single pointing observation. Mosaicking would require significantly more observing time increasing the total time on target to an unrealistic amount considering the high pressure on ALMA expected.

For the simulated observations of the model images, the disks are placed at 11 different distances from Earth distributed logarithmically from 10 pc to 100 pc. The dust mass ($\propto$ total disk flux) is scaled to different values assuming an optically thin disk. The SNR is estimated as the ratio between peak flux in the simulated observations of a target and the background fluctuation. A linear fit is performed on the distribution of SNR over disk mass considering only data with SNR > 20. From this fit, the disk mass needed to reach an SNR of 10 is computed. This is considered to be a robust detection of the disk.

9.3 Results

To properly interpret the results, one has to consider a number of specifics of an interferometric observation that are summarized in the following:

- The field of view of an interferometric observation using one single pointing is limited by the FWHM of an observation with one antenna (the primary beam). For the 12-m antennas of ALMA, this is $\lambda/12$ m.
- The spatial resolution δ_{min} of an observation (the FWHM of the synthesized beam) is determined by the maximum baseline B_{max} following $\delta_{\mathrm{min}} = \lambda/B_{\mathrm{max}}$.
- The largest angular scale δ_{max} of a target that will not be filtered out (resolved out) by the interferometric observations is determined by the minimum baseline B_{min} following $\delta_{\mathrm{max}} \approx 0.6\lambda/B_{\mathrm{min}}$[6].

[4] See, e.g., http://casaguides.nrao.edu/index.php?title=Simulating_Observations_in_CASA
[5] http://almascience.eso.org/document-and-tools
[6] ALMA Cycle 0 Proposers Guide, http://almascience.eso.org/document-and-tools

Table 9.1: Largest baseline $B_{\max}$, smallest baseline $B_{\min}$, and resolution characteristics of the array configurations used for the simulations.

			Band 10		Band 7		Band 6		Band 5	
Array number	$B_{\min}$ [m]	$B_{\max}$ [m]	$\delta_{\min}$ [″]	$\delta_{\max}$ [″]	$\delta_{\min}$ [″]	$\delta_{\max}$ [″]	$\delta_{\min}$ [″]	$\delta_{\max}$ [″]	$\delta_{\min}$ [″]	$\delta_{\max}$ [″]
01	15	161	0.45	4.8	1.22	13.1	1.60	17.2	2.05	22.0
03	15	260	0.28	4.8	0.75	13.1	0.99	17.2	1.27	22.0
05	15	390	0.19	4.8	0.50	13.1	0.66	17.2	0.85	22.0
07	15	538	0.13	4.8	0.36	13.1	0.48	17.2	0.61	22.0
09	15	703	0.10	4.8	0.28	13.1	0.37	17.2	0.47	22.0
11	15	1038	0.07	4.8	0.19	13.1	0.25	17.2	0.32	22.0
13	24	1440	0.05	3.0	0.14	8.2	0.18	10.7	0.23	13.8
15	24	1811	0.040	3.0	0.108	8.2	0.140	10.7	0.180	13.8
17	49	2297	0.031	1.5	0.085	4.0	0.112	5.3	0.144	6.7
19	49	3105	0.023	1.5	0.063	4.0	0.083	5.3	0.106	6.7
21	79	6068	0.012	0.9	0.032	2.5	0.042	3.3	0.054	4.2
23	79	11457	0.006	0.9	0.017	2.5	0.022	3.3	0.029	4.2
25, 27	79	14444	0.005	0.9	0.014	2.5	0.018	3.3	0.023	4.2

The derived values of $B_{\min}$ and $B_{\max}$ as well as the resolution characteristics $\delta_{\min}$ and $\delta_{\max}$ for the different array configurations and bands considered are listed in Table. 9.1. With the derived values one can now explain the features seen in the sensitivity maps that are shown in Figs. 9.1 and 9.2. First, there are a number of configurations in the explored parameter space that cannot be observed with the strategy assumed or where the approach used to estimate the sensitivity produces erroneous results:

- In particular for very extended, nearby disks, it is not possible to observe them without mosaicking at short wavelengths, since the spatial extent of the disks is larger than the field of view of the observations. The configurations where this is the case are marked by a black cross in an empty (white) pixel in Figs. 9.1 and 9.2.
- For the highest resolution (most extended arrays), in particular nearby, extended disks are resolved out. These regions are marked in Fig. 9.1 and 9.2 by an "x".
- For high spatial resolution, the FWHM of the synthesized beam is similar to or smaller than the pixel size of the synthetic images. This results in heavy residuals from image reconstruction and does not allow to proper quantify the SNR in the simulated maps. Note that this is a limitation of the approach used, not a real limitation of ALMA. However, at such high resolution, the disks would have to be extremely massive (bright) to be detected at all (see the discussion of the sensitivity below).

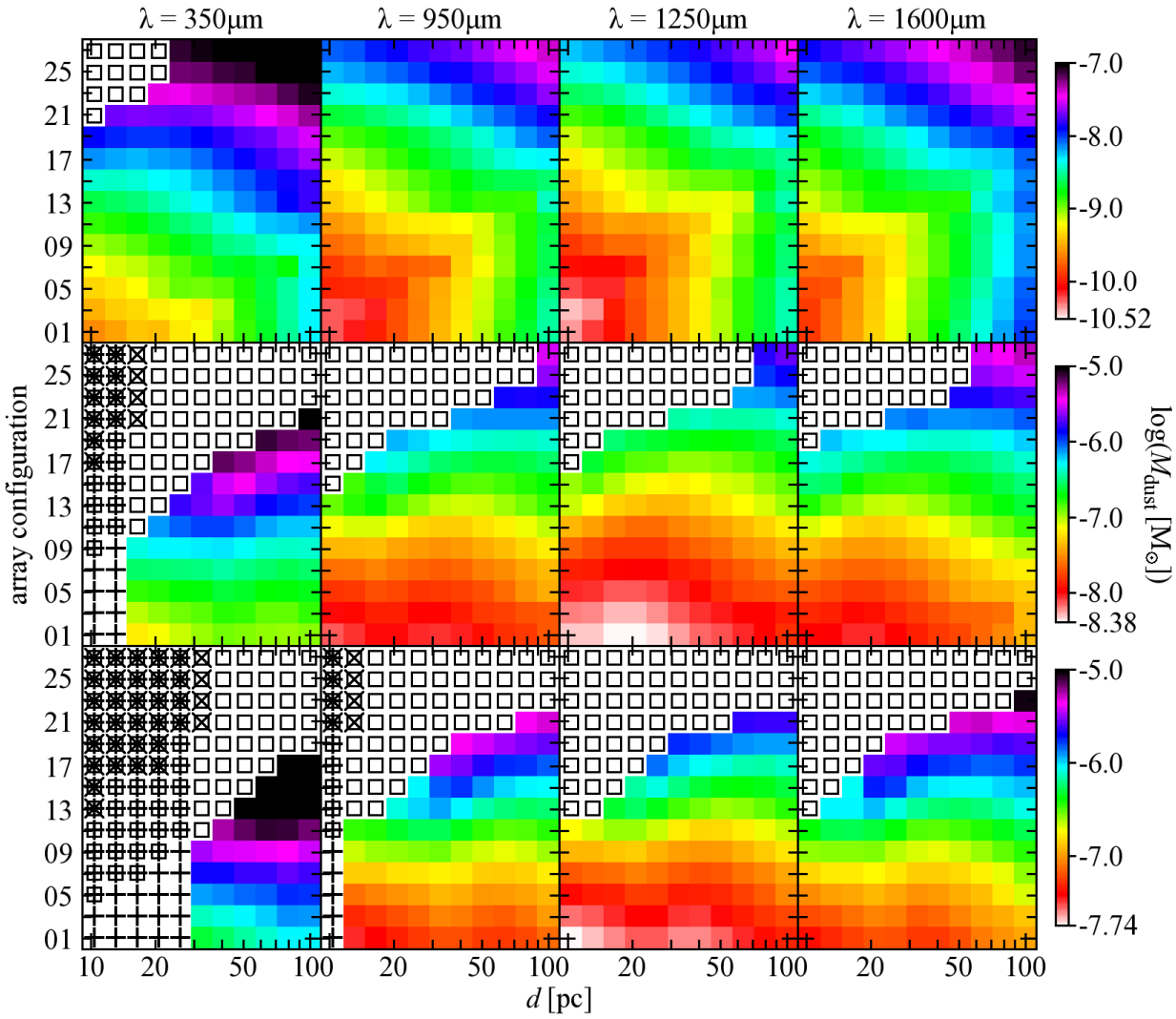

Fig. 9.1: Maps of the $10\,\sigma$ sensitivity of ALMA to face-on seen debris disks of different mass for different distance of the disk and array configuration and at different wavelength of observations. The three rows refer to different disk extends given by $r_{\rm in}$ of 5 AU (*top*), 50 AU (*middle*), and 100 AU (*bottom*). Disk mass can be converted into fractional luminosity following Eq. 9.1. For details about the model images used and about the simulation of observations see Sects. 9.1 and 9.2. White pixels with symbols mark positions where the simulations failed or observations are impossible due to different reasons denoted by the symbols as follows (see Sect. 9.3 for more details): *cross* – The spatial extent of the disk is larger than the field of view of a single pointing, *x* – the disk is "resolved out" (the radial width of the ring is larger than the largest scale detectable), *open square* – artifacts of the image reconstruction due to deficiencies of the model image dominate the simulated observations.

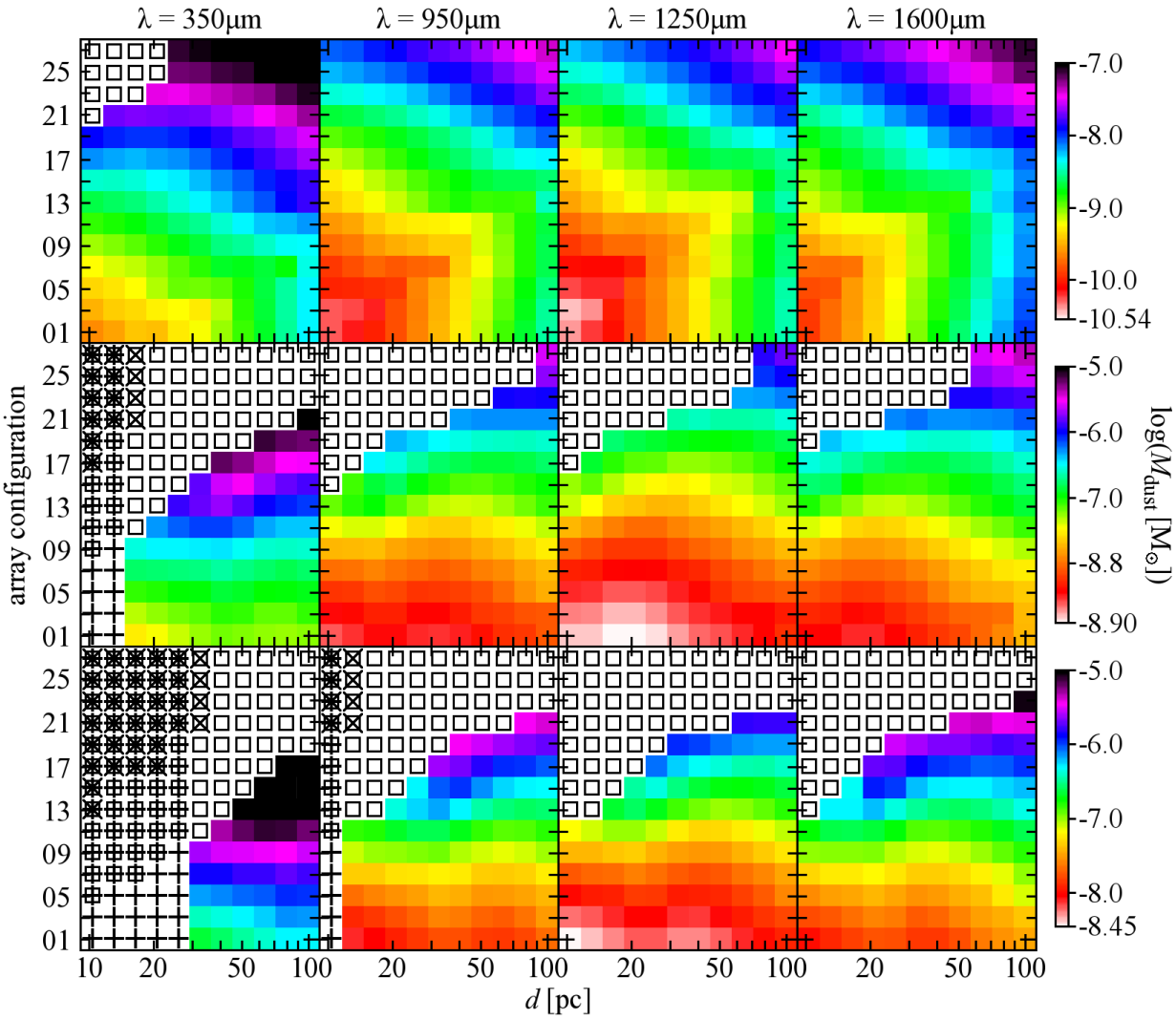

Fig. 9.2: Same as Fig. 9.1, but for edge-on orientation of the disk.

In the regions of the parameter space where the simulations are not affected by the above limitations, one can evaluate the sensitivity. The following behaviour in the parameter space can be found:

- In general, the highest sensitivity is reached in band 6 (central wavelength 1250 μm).
- For a given spatial resolution, the sensitivity is only slightly decreasing with increasing distance as long as the disk is spatially resolved (FWHM $\leq 2\,r_{\rm out}$). This can be explained by the fact that the surface brightness of the disk (e.g., in mJy/arcsec^2) is decreasing with the distance squared, but the beam covers an increasing area of the disk, depending on the scales of the dominating structures of the disk.
- For a given distance, the SNR is increasing with decreasing spatial resolution as long as the disk is spatially resolved. This is because the beam covers a larger area of the disk

at very similar sensitivity (e.g., in mJy/beam). As long as the FWHM is smaller than the dominating structure of the disk (e.g., the ring width), the sensitivity is increasing with the square of the FWHM.

- As soon as the disk is spatially unresolved, the sensitivity drops with the distance squared for a given spatial resolution.
- In general, edge-on seen disks have a higher surface brightness. Thus, spatially resolved observations of an edge-on seen disk will result in a higher SNR than the same observations of the same disk seen face-on. Beside this, there is no significant difference between imaging of edge-on seen and face-on seen disks (for the employed disk models). This can be explained by the fact that for spatially resolved imaging only the peak SNR is considered, which depends on the scale and brightness of the brightest structures in the disk. This is in both cases the radial width of the ring and in the case of an edge-on seen disk the vertical height (which is of the same order). For spatially unresolved observations, the orientation of the disk has no effect at all.

The above qualitative discussion leads to an important recommendation for optimal spatially resolved imaging of debris disks with ALMA. As long as the structures of interest are bright enough, one should always use a spatial resolution similar to the scales of interest. Most importantly, one should avoid to over-resolve the structures, since sensitivity is then decreasing with the square of the spatial resolution.

ALMA will not only increase our knowledge about the known, spatially resolved debris disks due to the higher sensitivity and spatial resolution. Due to the nearly constant sensitivity to dust mass in spatially resolved imaging at distances up to $\approx 100\,\mathrm{AU}$ (for disks with radial extents of few tens of AU), ALMA will significantly increase the sample of debris disks spatially resolved at millimeter wavelengths towards more distant systems.

10 On the observability of planet-disk interaction in debris disks

The presence of planets and debris disks is thought to be correlated. In a system with a debris disk and one or more planets, one would expect gravitational interaction between the dust grains and the planet, trapping them into resonance (Wyatt 2006; Wolf et al. 2007; Stark & Kuchner 2008, 2009). This results in structures in the disk that may be observable, providing a method to infer and characterize planets in a regime of masses, brightness, and radial distances from the star that is not accessible through other techniques such as radial velocity measurements or direct imaging (Udry & Mayor 2008; Marois et al. 2008; Kalas et al. 2008). Clumpy structures in debris disks have been observed in several cases (e.g., ϵ Eri, Greaves et al. 1998; AU Mic, Liu 2004; HD 107146, Corder et al. 2009; Hughes et al. 2011).

In this chapter, the observability of structures in debris disks is investigated in a systematic way. A number of initial configurations of the planetary and planetesimal system are set up. From each of these configurations, the spatial dust distribution is simulated using N-body simulations and images are created at different observing wavelengths. As shown in the previous chapter, ALMA will allow one to obtain high spatial resolution images of a large sample of debris disks in the (sub-)mm. To investigate the ability to observe the structures found from the N-body simulations, ALMA observations of the synthetic images are simulated. Furthermore, the *James Webb* Space Telescope (JWST; Gardner et al. 2006) will allow for high sensitivity, high spatial resolution imaging in the optical to mid-infrared in the near future, providing additional opportunity to observe planet-disk interaction in this wavelength range. Available information on the capabilities of the JWST are used to make predictions on the ability to detect and spatially resolve the simulated structures with this future facility.

The approach for the N-body simulations and the image creation are described in Sect. 10.1. The results from the dynamical simulations are presented and briefly discussed in Sect. 10.2. In Sect. 10.4, the observability of the found structures with different facilities is evaluated. Conclusions are drawn in Sect 10.5.

10.1 Modeling planet-disk interaction in debris disks

The tool `MODUST` (Sect. 5.1) is employed to simulate the dynamical evolution of a large ensemble of dust particles in the gravitational potential of a central star. The influences of planetary perturbations, radiation pressure, Poynting-Robertson drag, and stellar-wind

drag are considered. Electromagnetic (Lorentz) forces on charged dust particles are neglected (Gustafson 1994; Holmes et al. 2003). Mutual collisions of dust particles are not considered in the dynamical modeling.

10.1.1 Initial conditions and approach

Since the simulation of the resulting dust distribution is very time consuming, it is not possible to perform a dense sampling of a large, high dimensional parameter space. The present work concentrates on the following parameter regime:

- One central star (no multiple systems),
- A solar-type star as central star, photospheric emission realized by a black body with $T_{\rm eff} = 5778\,{\rm K}$, $L_\star = 1.0\,L_\odot$, $M_\star = 1.0\,M_\odot$, $\xi = 0.35$ (Sect. 2.2, stellar wind),
- One planet (considered to dominate the dynamics of the system),
- One initial dust disk (no initial multi-ring systems),
- Planetary orbit and initial dust disk are coplanar.

Astronomical silicate (Draine & Lee 1984; Weingartner & Draine 2001) with a bulk density of $2.7\,{\rm g/cm^3}$ is employed for the chemical composition of the dust. The dust is assumed to be produced through collisions in a disk of planetesimals. It is then redistributed by the influence of various forces listed above (see Sect. 2.2 for a detailed physical description). This is realized by placing the initial dust distribution at the same position as the planetesimal disk postulated to produce the dust. Particles that are lost because they are sublimated or ejected from the system are replaced by new ones from this reservoir of initial dust grains. Furthermore, the grain size distribution of *all grains in the system* applied follows a power-law as expected from an equilibrium collisional cascade (exponent -3.5). This approach is used to mimic dust production through collisions of the parent bodies. Note that the local grain size distribution may be significantly different due to the size dependent redistribution of the grains through radiation pressure and Poynting-Robertson drag and due to the dynamical interaction with the planet (Moro-Martín & Malhotra 2002, 2003).

The lower boundary $a_{\rm min}$ of the applied grain size distribution is defined by the blow-out size ($\beta = 0.5$, $a_{\rm min} \approx 0.43\,\mu{\rm m}$). The upper boundary $a_{\rm max}$ of the distribution is set to $2\,{\rm mm}$ ($\beta \approx 1.06 \times 10^{-4}$). The impact of even larger grains (see discussion in Sect. 4.4) can be neglected in the present study. These grains are distributed the same way as the large grains considered, since the effect of the stellar radiation on the grain dynamics can be neglected for grains this large and all other forces considered are size independent. Thus, the additional emission of these grains would only increase the brightness of the structures produced by the large grains by few percent. This has no significant impact on the conclusions drawn from the simulations.

Gaussian distributions have been applied to set the initial eccentricities and inclinations of the test particles. At the start of the integration, the majority of dust grains have orbital

eccentricities between 0 and ~ 0.4 (RMS of the Gaussian distribution = 0.15). The full width at half maximum of the inclination distribution has been set to 10°. These values are consistent with measurements on dust parent bodies in the Kuiper Belt of the Solar System (Jewitt et al. 1996; Vitense et al. 2010). The semi major axes of the particles are distributed following a power-law (surface density $\Sigma(r) \propto r^{-\alpha}$; Wolf & Hillenbrand 2003) from a lowest to a highest value considered as the inner and outer radius of the disk, $r_{\rm in}$ and $r_{\rm out}$.

To properly sample the thermal reemission of different grain sizes in the final images to be created, the grain size distribution is sampled by 50 grain sizes distributed logarithmically between the lower and the upper grain size. For each size bin, `MODUST` is started once to get the distribution of the particles of this particular size in the system. A total number of 1000 test particles per size bin is used. The system evolves over 5 times the corresponding Poynting-Robertson time scale (Eq. 2.29) of grains of the corresponding β at the outer edge of the disk, but not longer than the assumed age of the system (see motivation of the single runs below). Over the last 10% of each run time (equally distributed), 100 snapshots of the particle distribution are taken following Rodmann (2006) to virtually increase the number of particles in each size bin.

The parameter space explored is motivated by the aspiration to cover a number of general configurations possible and by analogies to our Solar System and other known debris disks. The position and shape of the dust disk as well as the position, mass and eccentricity of the planet are used as parameters for the initial conditions. The different combinations of values explored for these parameters are listed in Table 10.1 and described in the following:

- A first sequence of initial conditions (Ia to Id) place the planet ($1\,M_{\rm J}$[1], circular orbit) in 1:1 or in 2:1 resonance with the initial planetesimal belt. The initial dust disk is a narrow ring ($r_{\rm out} = 1.1\,r_{\rm in}$, constant surface density) with two realizations of $r_{\rm in}$ (5 AU for runs Ia and Ib and 50 AU for runs Ic and Id). The two assumed positions of the dust ring are motivated by our Solar System (Asteroid Belt and Kuiper Belt) as well as typical positions of the dust in other known debris disks around solar type stars (e.g., ϵ Eri, Backman et al. 2009; HD 105 Hillenbrand et al. 2008; q[1] Eri, Marshall et al. 2011). An age (maximum run time $t_{\rm max}$ of the simulation) of 50 Myr is assumed for these runs (e.g., the approximate age of HD 105; Apai et al. 2008).
- A second sequence of initial conditions (IIa to IId) is motivated by the HD 107146 debris disk (Ertel et al. 2011; Chapt. 6 of the present work). The planet is orbiting at the inner edge of an extended disk ($r_{\rm in} = 70$ AU, $r_{\rm out} = 250$ AU, $\Sigma(r) \propto r^{-0.5}$). This model is similar to the results obtained for this disk in Chapt. 6, although a much more complex radial density distribution has been found there. Such a more complex distribution might be the result of the interaction of the disk with a possible planet and the temporal evolution of the disk. Different parameters for the planet are explored (Table 10.1). The age of the system is increased (100 Myr) compared to that employed in sequence I to account for the slightly larger age of HD 107146.

[1] $M_{\rm J}$: Jovian mass.

Table 10.1: Initial conditions for the different runs with MODUST.

Run	$r_{\rm in}$ [AU]	$r_{\rm out}$ [AU]	α	$M_{\rm pl}$ [$M_{\rm J}$]	$a_{\rm pl}$ [AU]	$e_{\rm pl}$	$t_{\rm max}$ [Myr]
Ia	5.0	5.5	0.0	1.0	5.0	0.0	50
Ib	5.0	5.5	0.0	1.0	3.15	0.0	50
Ic	50.0	55.0	0.0	1.0	50.0	0.0	50
Id	50.0	55.0	0.0	1.0	31.5	0.0	50
IIa	70.0	250.0	0.5	0.5	70.0	0.0	100
IIb	70.0	250.0	0.5	1.0	70.0	0.0	100
IIc	70.0	250.0	0.5	5.0	70.0	0.0	100
IId	70.0	250.0	0.5	1.0	70.0	0.1	100
IIIa	35.0	210.0	0.5	0.5	70.0	0.0	100
IIIb	35.0	210.0	0.5	1.0	70.0	0.0	100
IIIc	35.0	210.0	0.5	5.0	70.0	0.0	100
IIId	35.0	210.0	0.5	1.0	70.0	0.1	100

- A third sequence of models (IIIa to IIId) place the planet within a broad disk. Therefore, the initial conditions of sequence II are modified, so that the disk is now closer to the star (Table 10.1). The inner radius is comparable to that of the Kuiper Belt.

The tool MODIM (Sect. 5.2.3) is used to simulate images from the derived dust distributions. The image extension in one dimension used is 301 pixels for Sequence I (pixel resolution of 0.1 AU for runs Ia and Ib and 1.0 AU for runs Ic and Id) and 251 pixels for Sequence II and Sequence III (pixel resolution of 2.0 AU).

10.2 Results from the dynamical modeling

From the computed images, one can draw a number of conclusions on the nature and strength of the structures produced, on the requirements for strong structures to be produced, and on the wavelength dependence of structures visible in the data. The results can be seen in Figs. 10.1, 10.2, 10.3, and 10.4. In the following, these results are discussed briefly.

10.2.1 The face-on case

In the case of a face-on or nearly face-on oriented disk, the azimuthal and radial disk structure can be observed directly. This allows to draw strong conclusions on the disk structure from observations without the need of detailed modeling or disentangling the

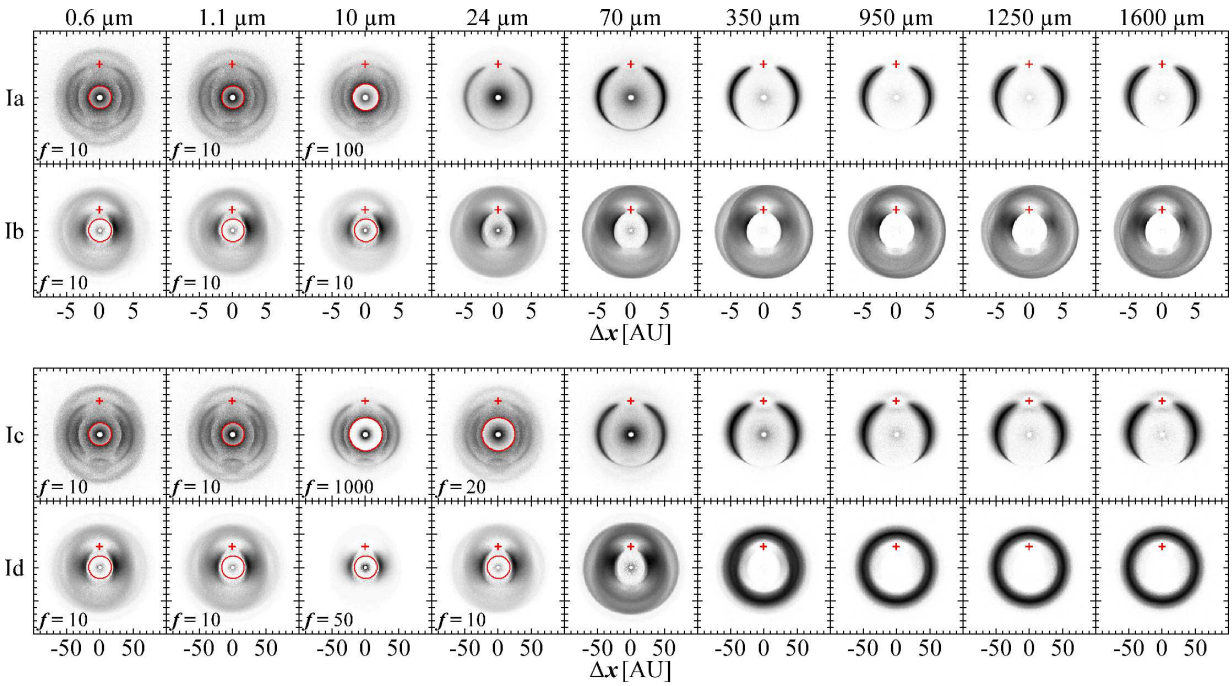

Fig. 10.1: Simulated images from model sequence I for a face-on orientation of the disk at different wavelengths. The wavelength is indicated at the top of each column. The star is at the center. The position of the planet is indicated by the red cross. The flux is given in arbitrary units and displayed in a logarithmic stretch from zero to peak value. The region marked by a red circle in some images has been attenuated by a factor f to properly display the dynamical range of the images (indicated in the lower-left corner of each image). If no value of f is given, no attenuation has been applied.

real structure from projection effects. On the other hand, it is impossible to draw any strong conclusion on the vertical structure of the disk.

Prominent structures at short wavelengths

Short wavelengths (optical and near-infrared scattered light as well as short wavelength thermal reemission) predominantly trace small grains. These grains are subject to efficient Poynting-Robertson drag causing them to move radially through the system. Thus, they can easily reach regions in the disk where they can be trapped into resonance by the planet. This causes prominent structures in their distribution. The shape and strength of these structures depend on the mass of the planet. In general, a more massive planet is able to keep a larger region clear of dust than a less massive one. On the other hand, less massive planets produce a very prominent, bar-like structure.

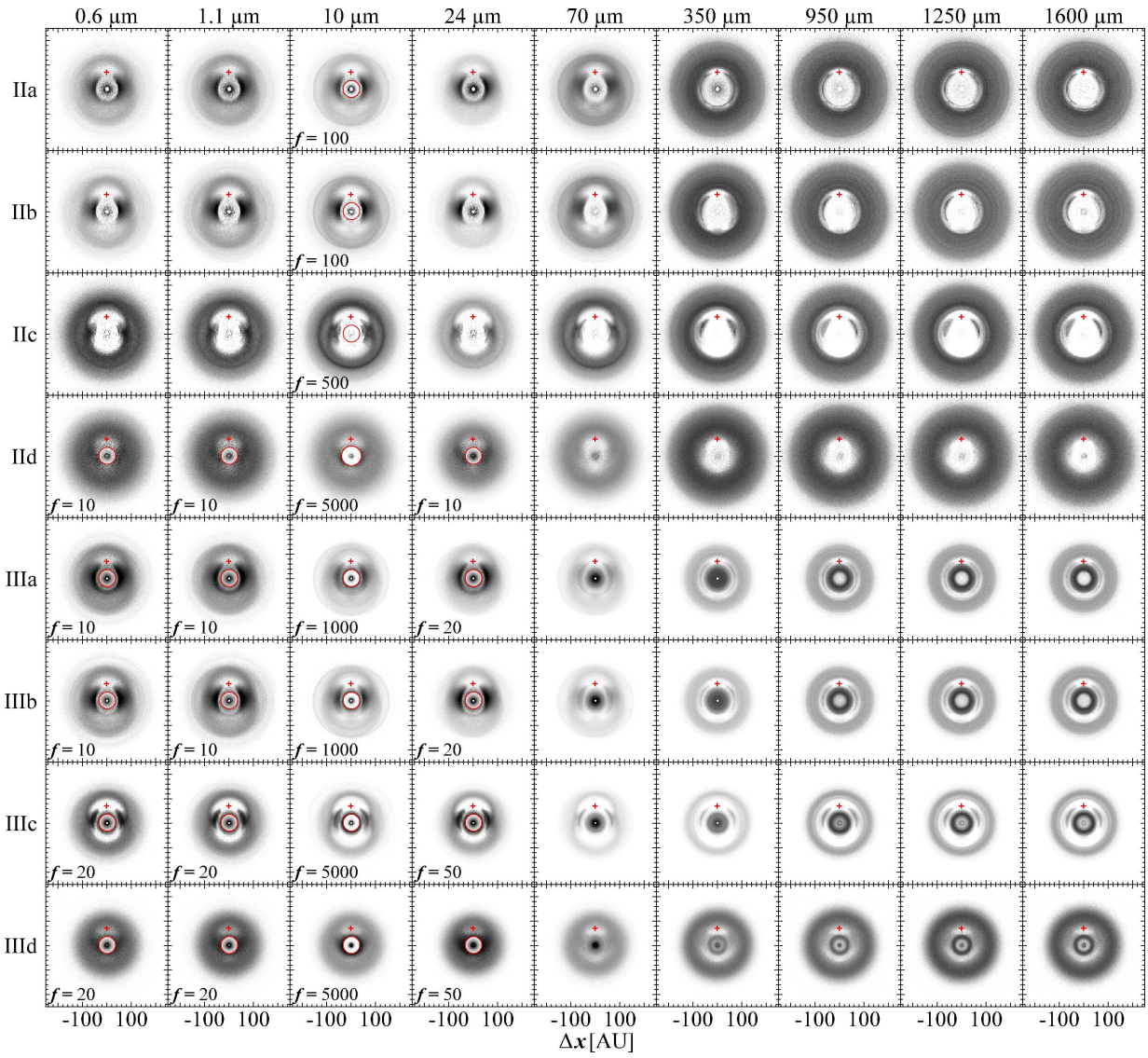

Fig. 10.2: Same as Fig. 10.1, but for model sequences II and III. The flux is given in arbitrary units and displayed in a logarithmic stretch from zero to 1/2 of the peak value at wavelengths up to 24 μm and to 2 times the peak value at longer wavelengths.

Prominent structures at small distance from the star

In a similar way as above, particles at small radii are more efficiently affected by Poynting-Robertson drag than particles at larger distance from the star. Thus, the same resonant configuration of planet and disk results in more prominent structures in the distribution of larger grains (at long thermal reemission wavelengths), if placed closer to the star.

Prominent 1:1 resonance at long wavelength thermal reemission

Large particles are mostly traced by long wavelength thermal reemission, since they emit more efficiently at these wavelengths and are cooler than smaller grains. These grains are not moving significantly in radial direction through the system due to Poynting-Robertson drag (as long as they are not too close to the star, see previous point). Only their eccentricity causes a small, periodic change of their radial distance from the star in addition to the dynamical perturbation through the planet. Hence, they can only be trapped into resonance at the radial position where they are placed initially. This results in prominent structures caused by 1:1 resonance with the planet, while other resonances can be neglected in most of the cases. The result is a very prominent horseshoe structure (at long wavelength thermal reemission). The orbital velocity of these large grains at the same distance from the star as the planet is nearly the same as that of the planet due to the negligible effect of radiation pressure. This makes the resulting structures more stable and, thus, even more prominent. If the planet is placed far away from the disk, so that it cannot influence the disk by 1:1 resonance, its effect is very small. In any case, the prominence of the structures increases with increasing mass of the planet.

Prominent gaps

If the planet is placed within a broad disk, it opens a ring-like gap in the disk at long wavelengths. The width of the gap is increasing with increasing mass of the planet.

Faint inner disks

In all simulations, there is always a more or less significant amount of predominantly small grains which the planet is unable to prevent from moving towards the star. These particles move inwards till they reach their sublimation radius. This inner disk is particularly bright at short wavelengths (thermal reemission and scattered light).

Accumulation of dust close to the planet

There is a small amount of dust accumulated close to the planet. These particles are directly captured by the planet and form a disk around it. This results in an increased brightness of the planet (due to its dust disk), which increases the chances for direct detection. This scenario has been suggested to explain the high brightness of Fomalhaut b (Kalas et al. 2008).

10.2.2 The edge-on case

If a disk is seen edge-on, one is faced with a number of challenges when deriving its radial, azimuthal, and vertical structure. Since debris disks are optically thin, one integrates all flux on the line of sight. This results in strong degeneracies between radial and azimuthal structures. Furthermore vertical structures cannot be assigned to a particular radial and

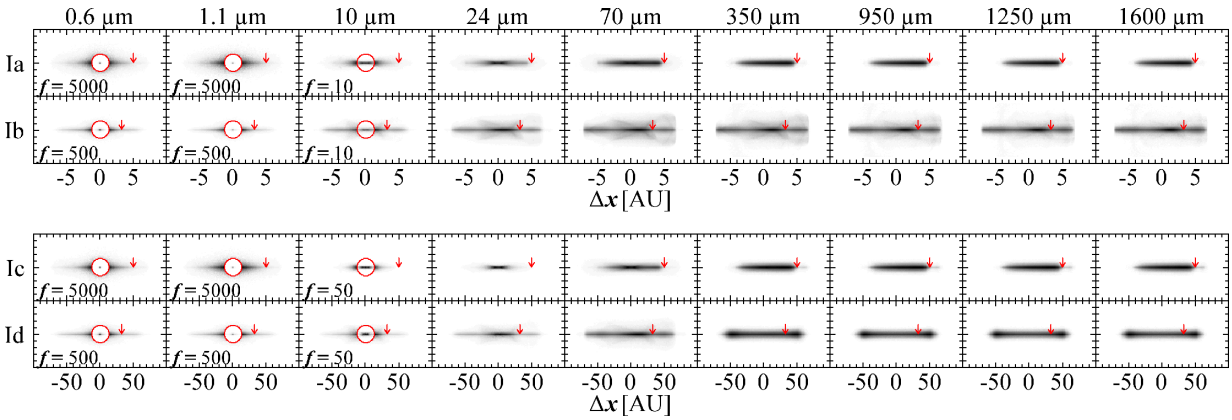

Fig. 10.3: Same as Fig. 10.1, but for an edge-on orientation of the disk. The star is at the center. The position of the planet is indicated by the red arrow.

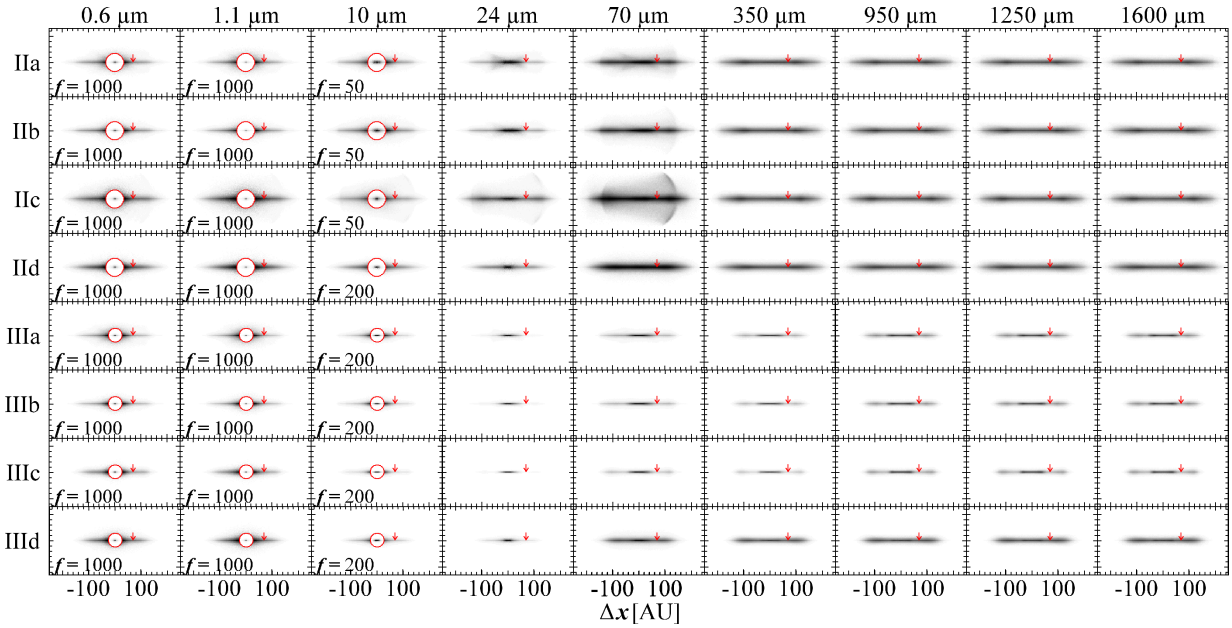

Fig. 10.4: Same as Fig. 10.2, but for an edge-on orientation of the disk. The position of the planet is indicated by the red arrow. The flux is given in arbitrary units and displayed in a logarithmic stretch from zero to 1/2 of the peak value at wavelengths up to 24 μm. At longer wavelengths the flux stretches logarithmically form zero to 1/2 of the peak value for model sequence II and to the peak value for model sequence III.

azimuthal position in the disk, but only to a distance from the star projected on the sky plane. However, most of the known, resolved debris disks are seen close to edge-on. This is most likely because of the higher surface brightness due to more emitting material on the line of sight, which results in an observational bias. For that reason, it is particularly interesting to search for prominent structures in edge-on seen debris disks due to planet-disk interaction that can be identified uniquely.

Particles scattered out of the disk mid plane

Particularly for massive planets close to the radial position of the dust production, there is a halo of particles scattered out of the disk mid plane by the interaction with the planet. The halo consists mostly of small and intermediate-sized grains moving efficiently through the disk in radial direction. At short to intermediate thermal reemission wavelengths, there are resonant structures visible. These structures are particularly prominent at these wavelengths, since they mostly consist of intermediate-sized grains. These grains are affected by Poynting-Robertson drag and radiation pressure sufficiently to interact with the planet and, thus, to be scattered out of the disk mid plane. On the other hand, Poynting-Robertson drag is not strong enough to prevent these grains from being trapped into resonance.

Asymmetries in the disk radial brightness profile

There is a brightness asymmetry between the two ansae of the disk. The disk ansa containing the planet is slightly brighter than the opposite ansa. This is due to the accumulation of dust in the resonances, which results in clumps of larger density (see face-on case).

Multiple peaks and dips in the disk radial brightness profile

A multi-ring structure as seen in particular in the long wavelength results from sequence III results in a wavy radial brightness profile along the disk mid plane in the edge-on case, while peaks are seen at the position of rings and dips are seen at the position of the gaps in the disk. The strength of these wavy structures depends on the exact configuration of the system as well as on the observing wavelength.

10.2.3 Age dependence of the above phenomena

The dominating effect that causes the dust grains to change their orbits beside the gravitational interaction with the planet is Poynting-Robertson drag. Thus, one has to compare the Poynting-Robertson time scale (Eq. 2.29) of different grains with the age of the systems. This time scale is short for small grains (large β) and increases with grain size (decreasing β). It also depends on the radial distance from the star. Thus, systems with the dust placed closer to the star evolve faster. Furthermore, structures in small grains evolve faster than in large grains. The older a system is, the larger grains have time to significantly move in radial direction and can be trapped into different resonances. Since these larger grains are traced by longer wavelengths, the transition between prominent

resonant structures and single 1:1 resonant horseshoe structure in the face-on case will be visible best at longer wavelengths for older systems.

It is important to note that no collisions between the dust particles are considered in the dynamical simulations. Structures that only appear after long time or that are particularly traced by particles that are very abundant may be destroyed by chaotic events like collisions. Furthermore, particles may be destroyed through collisions before they are able to form these structures. The strength of this effect decreases with decreasing dust mass. Thus, such structures are a result of the present modeling, but are not necessarily expected to be present in real systems (particularly in systems with very massive disks).

10.2.4 Potential for observations and modeling

From the above discussions, it is found that planet-disk interaction in debris disks produces structures in the disk that allow one to constrain the parameters of the planet-disk system (e.g., planetary mass, major axis, eccentricity, radial distribution of the parent bodies). However, data at one of the wavelength regimes considered are expected to provide only weak constraints, especially when taking into account observational effects like noise, resolution effects, and stellar PSF subtraction uncertainties (see Sect. 10.4 for simulated observations and discussion). It is also important to note that the same parameters of the planet result in very different structures depending on the configuration of the planetesimal belt producing the dust. On the model images themselves, this is particularly obvious when comparing the images at mid-infrared wavelengths (and shorter) in face-on orientation produced from sequences II and III (e.g., at 24 μm) and the corresponding (sub-)mm images (Fig. 10.2). While the mid-infrared data allow one to distinguish particularly well between planetary masses and eccentricities (e.g., between runs IIa to IId), the (sub-)mm data allow one to constrain in particular the major axis of the planet and the position of the parent bodies (e.g., compare images from runs IIa and IIIa). Thus, combined observations at both wavelength regimes will be particularly useful for detailed modeling of the planet-disk systems.

10.3 Comparison to previous simulations

It is possible to identify the structures described by Kuchner & Holman (2003) using simple geometrical arguments in the images produced from the present simulations (Fig. 10.1 and 10.2).

The present simulations are analogous to the work presented by Stark & Kuchner (2008), while the models are in a different region of the parameter space (more massive planets, further away from the star, larger dust grains with smaller β considered in the present work). While Stark & Kuchner (2008) concentrated on the effects of terrestrial planets on exozodiacal dust clouds, the scope of the present work is to search for structures induced by giant planets in debris disks and to simulate observations of the structures found. This requires a good sampling of the grain size dependent emissivity of the dust and, thus,

the grain size distribution. The grains in Stark & Kuchner (2008) are assumed to be not larger than $\sim 120\,\mu$m and to be produced by an external source (i.e., a planetesimal belt at considerable distance from the region modeled), which is a reasonable assumption for exozodiacal dust. In the present case, the dust producing planetesimal belt has to be taken into account. Thus, larger grains have to be considered. Furthermore, these grains cannot be neglected, since observations at (sub-)mm wavelengths will be simulated from the distributions, where millimeter-sized dust grains have a significant contribution to the dust emission. A total of 50 grain size bins are used in the present work in contrast to five bins in Stark & Kuchner (2008) and grains up to a size of 2 mm are considered. Nonetheless, the results from both works can be compared qualitatively. In particular, for models that represent similar parameter regimes, the results are very similar and differences can be attributed to the above described differences in the approaches as well as to the differences in the nature of the images themselves.

Wyatt (2006) modeled planet-disk interaction in debris disks using dynamical simulations including a migrating planet. Although the present approach is substantially different, both works attempt to model structures in debris disks. Thus, it is worth a brief comparison of the two approaches. In contrast to Wyatt (2006) no migrating planet is used in the present work to trap the planetesimals into resonance initially, but the dust is assumed to be produced through collisions in a ring-like, featureless disk. Furthermore, in the present work a much simpler approach is used to mimic dust creation in the planetesimal belt. On the other hand, Wyatt (2006) investigated the liberation of particles from the initial resonances only, while in the present approach the possibility is included that particles are trapped into other resonances than those in which they are initially (they do not have to be in resonance initially at all). Thus, the migrating planet is not necessary to produce resonant structures in the present approach.

These differences basically result in an inverse situation in the resulting model images. In Wyatt (2006), very prominent structures are seen at long wavelengths (tracing large particles that remain in the resonances in which they are initially). At short wavelengths, the disks appear smoother, since the particles emitting efficiently at these wavelengths cannot be held in the initial resonance. In contrast, the initial dust distribution in the present work is not necessarily in resonance with the planet. This results in a much smoother appearance of the disk at long wavelengths tracing particles that cannot be trapped into resonance efficiently, since they are not significantly moving radially through the system. Thus, strong structures at (sub-)mm wavelengths are only found in the present work, if the initial dust distribution is placed close to a strong resonance with the planet, or if the dust is close enough to the star that even millimeter-sized particles are significantly affected by Poynting-Robertson drag. On the other hand, small particles are trapped into resonances easily in the present work, because they move radially through the system due to Poynting-Robertson drag and, thus, can "find" those resonances.

Table 10.2: Reference systems for the simulated ALMA observations.

Run	Reference system	λ_{ref} [μm]	d [pc]	Host star	Age [Myr]	r_{dust} [AU]	F_{disk} (λ_{ref}) [mJy]	M_{disk} [$M_{\odot}$]
Ib	ϵ Eri	24	3.2	K2 V	850	3	330.0	5.7×10^{-11}
Ic	HD 105	850	40.0	G0 V	30	45 – 120	10.7	1.2×10^{-7}
IIc	HD 107146	350	28.5	G2 V	130	50 – 250	319.0	7.3×10^{-7}
IIIa	HD 107146	350	28.5	G2 V	130	50 – 250	319.0	3.7×10^{-7}
IIId	HD 107146	350	28.5	G2 V	130	50 – 250	319.0	5.5×10^{-7}

References. ϵ Eri: Backman et al. (2009); HD 105: Nilsson et al. (2010); Hillenbrand et al. (2008); HD 107146: Corder et al. (2009); Ertel et al. (2011); Chapt. 6 of the present work.

10.4 Evaluating the observability

In the following, observations of the modeled disk images are simulated using different near-future facilities. In addition, the detectability of structures with the *Hubble* Space Telescope are briefly discussed to explain, why the prominent scattered light structures seen in the present simulations have not been detected yet.

10.4.1 ALMA

ALMA is the most promising instrument to study structures in debris disks in the (sub-)mm regime in the near future. The procedure `simdata` of the CASA ALMA simulator is used to predict results of observations of selected results from the dynamical simulations. The optimum array configuration is selected by the resulting SNR and spatial resolution in the simulated images.

Selection of runs and preparation of the images

The selection of the runs for which ALMA simulations are carried out is done by the prominence of the structures seen in the (sub-)mm:

- Runs Ib, Ic, IIc, and IIId are found to well represent the prominent structures in the synthetic images for face-on orientation of the disk (Fig. 10.1 and 10.2).
- Run IIIa is selected as an example for structures seen in edge-on orientation of the disk (Fig. 10.4).

From these runs, observations are simulated at band 6 (central wavelength 1250 μm, found in Chapt. 9 to be the most sensitive one for the intended observations) as follows:

- Known debris disks with radial dust distributions similar to the simulated ones are selected as reference objects. Systems around solar-type stars are considered, since for

the dynamical simulations solar-type stars are used as well.

- A representative photometric measurement (in the (sub-)mm, where possible) is used to scale the total flux of the simulated images. Therefore, the total flux of the disk at the wavelength of these observations is computed.
- The disk is placed at the distance of the reference debris disk. A flux scaling factor is derived by comparing the flux of the modeled disk with the measured flux at the reference wavelength. This scaling factor is applied to the image at band 6 to properly scale the flux in this image to a realistic value.
- The stellar contribution of the host star of the reference debris disk is added to the center of the synthetic image.

The reference debris disk for each run, the reference wavelength, the applied flux at this wavelength, some basic information about the reference system, and the resulting dust mass when scaling the model disk to the observed flux are shown in Table 10.2. It is important to note that the model scaled to the observed flux of the reference debris disk at one wavelength is not expected to reproduce the whole spectral energy distribution of the disk properly. However, the reference debris disks are selected by their similarity to the model systems in the radial dust distribution and band 6 is clearly in the Rayleigh-Jeans regime of the dust reemission. Thus, the flux at this wavelength is considered to be at least realistic for a debris disk similar to the reference disk.

The reference debris disks used for the scaling of the model are motivated as follows:

- ϵ Eri for run Ib: The inner ring of debris ($\sim$ 3 AU from the star; Backman et al. 2009) is used. For this ring, the 24 μm flux is used as reference value to scale the flux in all model images, since the other disk components are expected to have significant contribution to the flux at longer wavelengths.
- HD 105 for run Ic: HD 105 is a massive debris disk around a solar-type star. Most of the dust is expected to be concentrated at a distance of 40 AU to 50 AU from the star (Hillenbrand et al. 2008).
- HD 107146 for runs IIc, IIIa, and IIId: The work on the HD 107146 disk (Ertel et al. 2011; Chapt. 6 of the present work) was the motivation for these runs (Sect. 10.1.1).

Parameters for the CASA simulations

The simulations are carried out using all configurations of the ALMA array in full operations provided by the CASA simulator. Observing conditions and parameters for the simulations are identical to the simulations in Chapt. 9. Band 6 (central wavelength 1250 μm) is used. Single pointing observations are simulated rather than mosaicking, since all simulated images fit into one field of view of a single pointing at band 6.

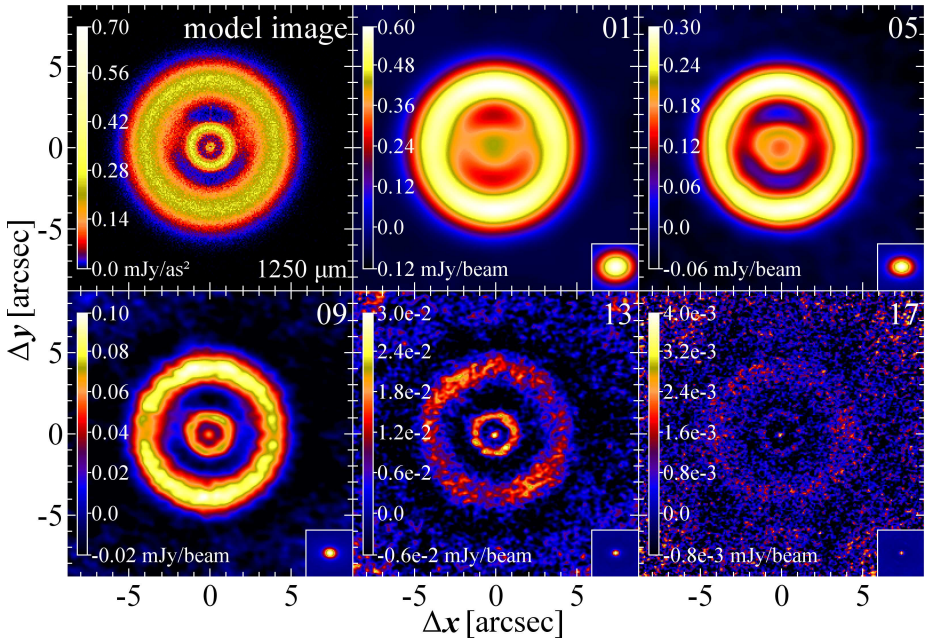

Fig. 10.5: Simulated ALMA observations at 1250 μm of the model image resulting from run IIId (face-on orientation) for different array configurations. Only the results from a representative number of array configurations are shown. The number in the upper-right corner of each image denotes the array number used. The corresponding beam is displayed in the lower-right corner of each image. See Sect. 10.4.1 for a detailed description of the parameters used for the simulated observations.

Results

One finds from the simulations of observations at different spatial resolution (different maximum baseline) that a trade-off between sensitivity and spatial resolution is necessary (see also Sect. 9.3). This is particularly well illustrated on the example of run IIId (Fig. 10.5). The bar-like structure within the (outer) gap in the disk is only visible at the lowest resolutions, while one needs a higher resolution to clearly resolve the inner gap and to clearly separate the innermost peak from the inner ring of dust at 1″ to 2″ from the star. For the five model disks considered for the ALMA simulations, the best array configurations based on high SNR and high resolution are selected. The model image resulting from run Ib is found to be too faint to be detected by any of the simulated observations. For the other four model images, the results are shown in Fig. 10.6. The selection of the optimum array configuration for each case is described in the following. The results are consistent with the suggestions for optimal spatially resolved imaging of debris disks derived in Sect. 9.3.

For *run Ic*, the structures are very smooth and no substructure is seen. Thus, one can use the peak SNR as a good tracer for the significance of the structures detected. Based on an additional, visible inspection of the images, a peak SNR of 22 (array 19,

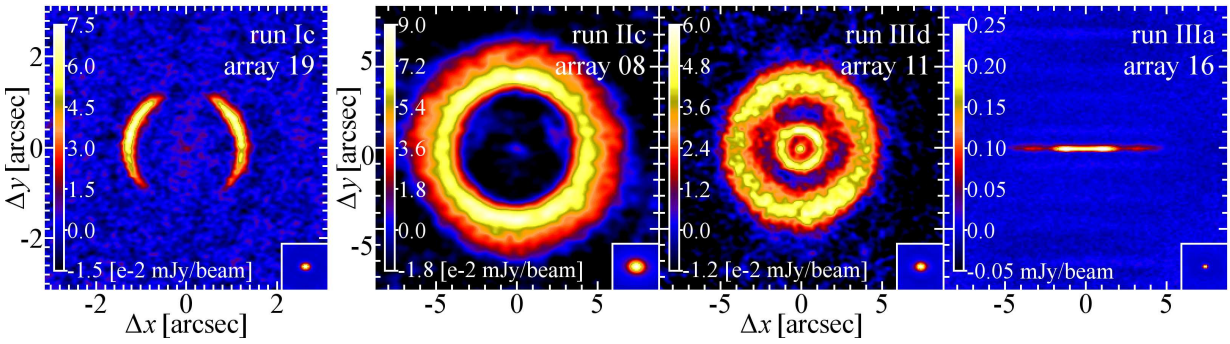

Fig. 10.6: Simulated ALMA observations on all selected model images. The optimum array configuration has been selected. The run as well as the array number are displayed in the upper-right corner, the corresponding beam is displayed in the lower-right corner of each image. See Sect. 10.4.1 for a detailed description of the parameters used for the simulated observations.

FWHM = 0.″11 × 0.″15) is found to give the best results, while the next larger array would result in a peak SNR of 15, but large parts of the disk would be detected at an SNR < 10.

For *run IIc*, the structure of interest would be the faint horseshoe structure at the inner edge of the disk. This structure can in any case only be observed at an SNR of up to 4. This is reached when the size of the beam is comparable to the size of this structure. The optimum is reached using array 08 (FWHM = 0.″62 × 0.″78). It is important to note that there is a negative background which is nearly homogeneous over the whole image. This can be attributed to the limitations of ALMA to observe very extended structures and of the simulations as described in Sect. 9.3. The signal has to be evaluated as the flux above this homogeneous background.

In the case of *run IIId*, value is placed on the multi-ring structure, while the bar-like structure is ignored. An example for an array configuration that results in a significant detection of the bar-like structure can be seen in Fig. 10.5. A peak SNR of 10 (array 11, FWHM = 0.″38 × 0.″47) is found to result in significant detection of the three disk components (outer and inner ring as well as innermost accumulation of dust), since they have a very similar surface brightness. The bar-like structure is visible at low SNR in these simulated observations, as expected from the previous discussion about the connection between spatial resolution and sensitivity to surface brightness.

In the case of the edge-on seen disk from *run IIIa*, the structure of interest is the gap in the disk seen as a dip in the radial brightness distribution and the outer disk seen as a secondary peak of the surface brightness beyond this gap. An SNR of 15 (array 16, FWHM = 0.″16 × 0.″22 – similar to the vertical extent of the disk) in the secondary peak of the surface brightness results in a clear detection of both features and allows one to marginally resolve the vertical extent of the disk.

10.4.2 Hubble Space Telescope

From the dynamical simulations, prominent structures in debris disks are found, in particular in scattered light and short-wavelength thermal reemission. In contrast, no face-on seen debris disk is known to exhibit such structures in scattered light observations. Thus, it is worth to briefly examine the observability of such structures in face-on seen disks with present instruments in scattered light, in particular with the HST with which most of the scattered light detected debris disks have been discovered. This is done in the present work on the example of the HD 107146 debris disk. It is one of the few (close to) face-on seen debris disks observed in scattered light (Ardila et al. 2004; Ertel et al. 2011).

The HST/ASC image in the F606W ($\lambda_c = 0.6\,\mu$m) filter presented by Ardila et al. (2004) is used to evaluate the observability of simulated structures in these data. Therefore, the model subtracted image of Ertel et al. (2011; Chapt. 6 of the present work) is employed, which represents the pure PSF subtraction residuals (within the capabilities of the modeling carried out). To these data, simulated images from the dynamical modeling (inclination of 25° from face-on applied from Ardila et al. 2004) are added after scaling them to the scattered light flux of the fitted disk at the same wavelength. This results in simulated observations on the model images using the same strategy as for the original observations. The results for the model images from runs IIb and IIc are shown in Fig. 10.7.

While the disk is clearly detected, the structures of the modeled images are corrupted by the strong PSF subtraction residuals. Thus, one would not be able to draw strong conclusions on the azimuthal structure of the disk from such data. Furthermore, there is only a small number of face-on seen debris disks detected in scattered light. In contrast, the two most prominent edge-on seen debris disks β Pic and AU Mic exhibit clumpy and warped structures that might be interpreted as structures in the disk induced by planet-disk interaction (e.g., Liu 2004; Golimowski et al. 2006). All this suggests that the structures found by the modeling in this work may be present, but not detected in face-on seen debris disks, yet.

10.4.3 Space-based near to mid-infrared telescopes

Near future, space-based, near to mid-infrared telescopes (e.g., the *James Webb* Space Telescope, JWST, or the Space Infrared Telescope for Cosmology and Astrophysics, SPICA) are expected to provide high sensitivity, high angular resolution imaging capabilities in the optical to near-infrared. In this section, observations with such facilities are predicted based on available information about the expected capabilities of the JWST. Since the focus of this work is on spatially resolved imaging capabilities, the two relevant instruments are the Near InfraRed Camera (NIRCam) and the Mid InfraRed Instrument (MIRI). NIRCam provides imaging capabilities in the 0.6 μm – 5.0 μm wavelength range. In this range, coronagraphy is necessary to block the direct stellar radiation. The HST is very successful in coronagraphic imaging of bright debris disks and the JWST will exceed these capabilities due to higher sensitivity and spatial resolution. However, the performance of coronagraphic instruments depends on several influences such as PSF stability. Thus, the exact results of

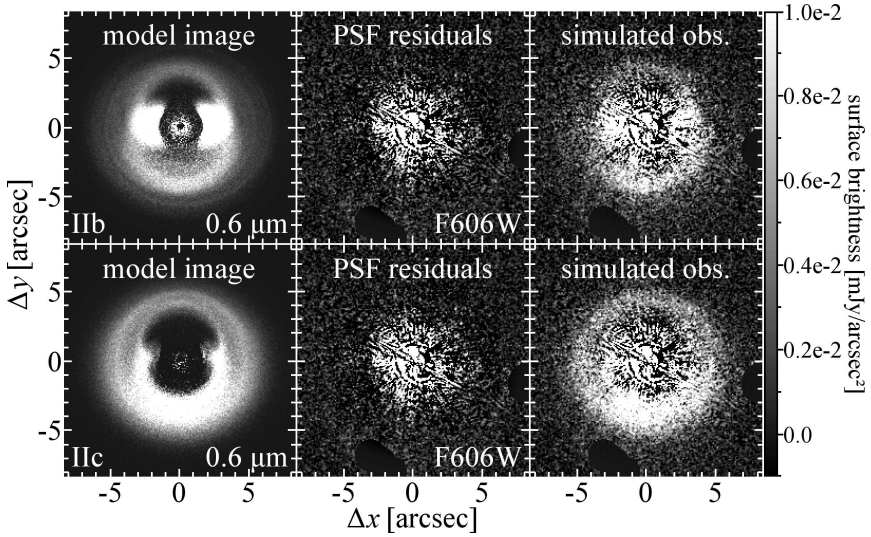

Fig. 10.7: Simulated HST/ACS coronagraphic observations of the simulated images from runs IIb and IIc at 0.6 μm. The disk is inclined by 25° along the x-axis, so that the lower half of the disk points towards the observer. For details see Sect. 10.4.2.

such observations are hard to predict without detailed knowledge about the performance of the instrument during science operations. Hence, the focus of the present section is placed on predictions on the capability of debris disk observations through none-coronagraphic imaging as possible with MIRI.

MIRI will provide imaging capabilities in the wavelength range of 5.0 μm – 29 μm. In particular at the long wavelength edge of this range, thermal radiation of debris disks is expected to have a detectable level. With a spatial resolution of $\approx 1''$ and high sensitivity, MIRI is the first instrument that will allow for resolved imaging of a large number of debris disks in this wavelength range.

A number of runs are selected from the dynamical simulations in order to explore the capabilities of MIRI to detect the structures found. Since the star contributes significantly to the flux at mid-infrared wavelengths, a stellar PSF subtraction is expected to be necessary to clearly reveal any resolved disk structure. To evaluate the observability of structures in debris disks, a two step approach is used:

(1) Observations of the disk only are simulated by convolving the synthetic disk images with the telescope PSF. From the resulting images, the sensitivity needed is estimated and the capability to spatially resolve the structures is evaluated.

(2) The stellar PSF contribution is estimated and the PSF subtraction accuracy needed is evaluated.

For simulated observations of the disk only, the images at 24 μm resulting from the dynamical simulations are scaled to the 24 μm fluxes of two reference debris disks, ϵ Eri and HD 107146. A summary of the considered runs and the references used for each run

Table 10.3: Reference systems for the simulated JWST observations.

Run	Reference	$F_{\rm disk}$ [mJy]	$F_\star$ [mJy]	$M_{\rm disk}$ [$M_\odot$]
Ia	ϵ Eri	330.0	1726	8.5×10^{-12}
Ib	ϵ Eri	330.0	1726	7.3×10^{-12}
IIa	HD 107146	19.0	40.8	4.4×10^{-8}
IIc	HD 107146	19.0	40.8	1.4×10^{-7}
IId	HD 107146	19.0	40.8	5.7×10^{-8}
IIIc	HD 107146	19.0	40.8	7.4×10^{-9}

Notes. The reference wavelength at which the fluxes are given is 24 μm for both systems. Also note the information given in Table 10.2 about the two reference systems.
References. ϵ Eri: Backman et al. (2009); HD 107146: Hillenbrand et al. (2008).

is given in Table 10.3. This approach is expected to result in a realistic mid-infrared brightness of the disk images, which is important for the simulated observations, but not in a good reproduction of the SED of the system over the whole wavelength range. The disks are placed at the distance of the reference debris disks. The images are convolved with a simulated PSF of MIRI at 25.5 μm (Fig. 10.8) produced by the software `WebbPSF`[1]. The resulting sensitivity of the observations is estimated using the 10 σ sensitivity of 30 μJy (10 σ, λ = 25.5 μm, integration time = 10^4 s)[2] and scaling it with the square root of the actual integration time (Gardner et al. 2006).

Since ϵ Eri is the only known debris disk this close and it is seen close to face-on, only the face-on orientation is used for the simulated observations on the example of the inner disk in this system. The results are shown in Fig. 10.9. For the simulated observations on the example of the HD 107146 debris disk, face-on and edge-on orientations are used, since a number of disks with different orientation is known at similar distance. The results from these simulated observations are shown in Fig. 10.10. In both the ϵ Eri and the HD 107146 case, one can see that the disks are spatially resolved. One can clearly distinguish between the different planet-disk configurations in both the face-on and the edge-on case. Only the results of run IIIc do not show a clearly resolved image of the disk. In contrast, the bright, unresolved inner part of the disk dominates the emission, which results in a bright image of the PSF overlayed on the outer disk structure.

In Fig. 10.8, one can clearly see the hexagonal structure and the peaks of the PSF at high order. Since the star gives a dominant contribution to the flux in the mid-infrared, one has to perform accurate PSF subtraction to distinguish between real disk structures and these high order PSF structures. To evaluate the accuracy of stellar PSF subtraction necessary, the contribution of the PSF depending on the radial distance from the star has

[2]http://www.stsci.edu/jwst/science/data-simulation-resources; effective Aug. 2011

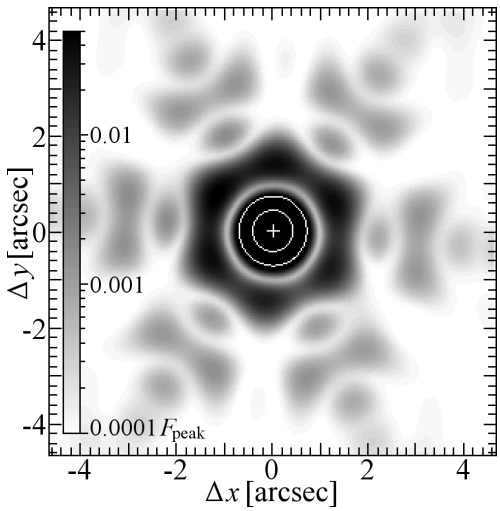

Fig. 10.8: Simulated PSF of JWST/MIRI at 25.5 μm. The image is shown in a logarithmic stretch from 0 to 5% of the peak flux to highlight the high order structure. The white contours represent 10% and 50% of the peak flux.

to be computed. Therefore, the PSF used to convolve the disk images is scaled to the total flux of the star in each of the two reference systems. The maximum of the PSF in one pixel wide radial bins (pixel scale of the simulated disk images) is computed. The result is shown in Fig. 10.11. To get a reliable image of the disk, the contribution of the stellar PSF should be reduced by PSF subtraction (e.g., through observations of a reference star) to a level of $\approx 1/10$ or less of the disk flux at comparable distance from the star. The accuracy

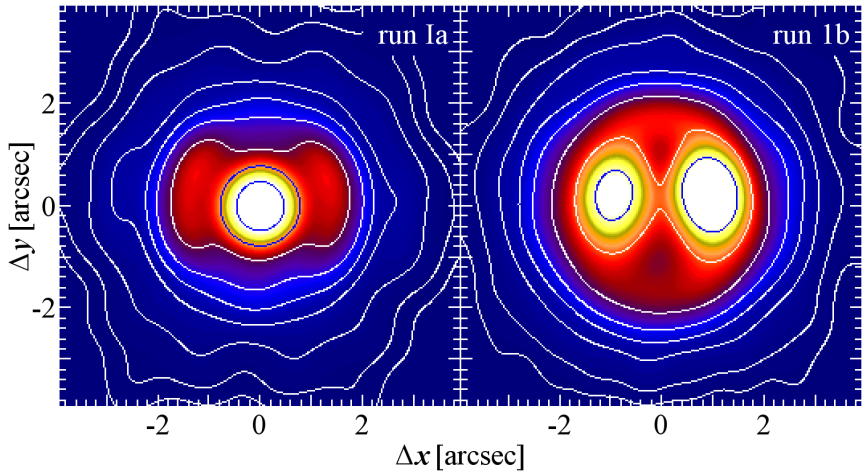

Fig. 10.9: JWST/MIRI images at 25.5 μm simulated from the runs Ia and Ib. The ϵ Eri inner debris disk is used as reference. The contours represent 3 σ, 5 σ, 10 σ, 20 σ, ... (double every step) SNR levels for a total integration time of 10 s. The images are shown in a logarithmic stretch.

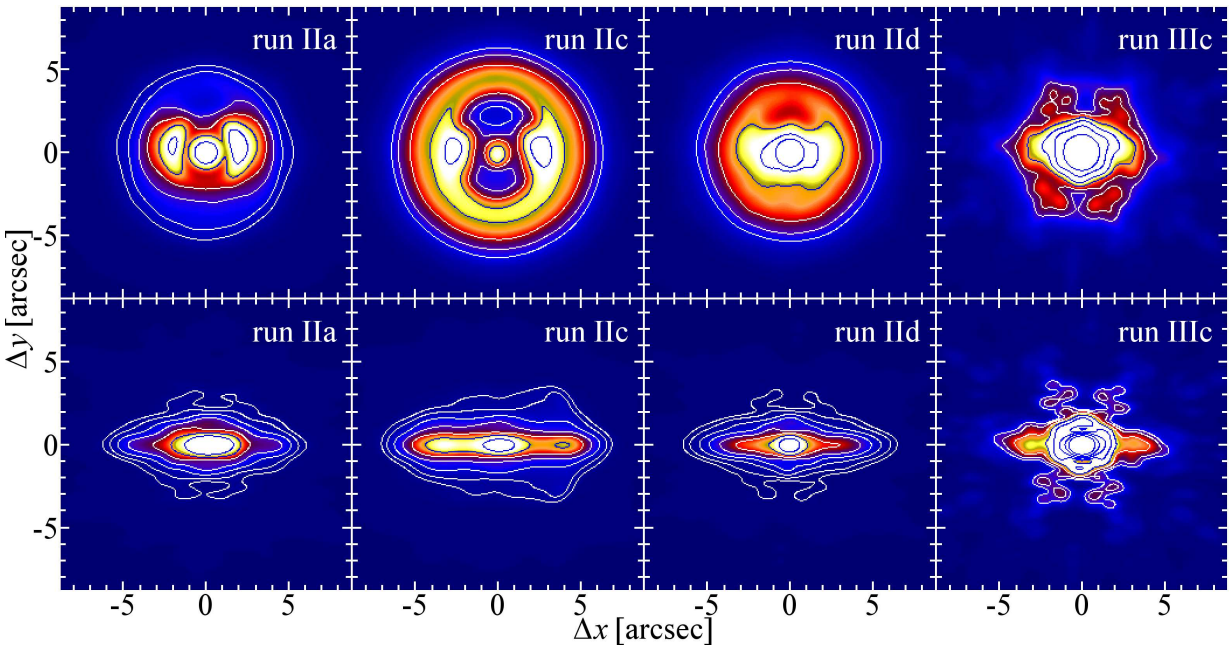

Fig. 10.10: Images at 25.5 μm produced from the runs IIa, IIc, IId, and IIIc. The HD 107146 debris disk is used as reference. The contours represent 3 σ, 5 σ, 10 σ, 20 σ, ... (double every step) SNR levels for a total integration time of 900 s. The images are shown in a logarithmic stretch.

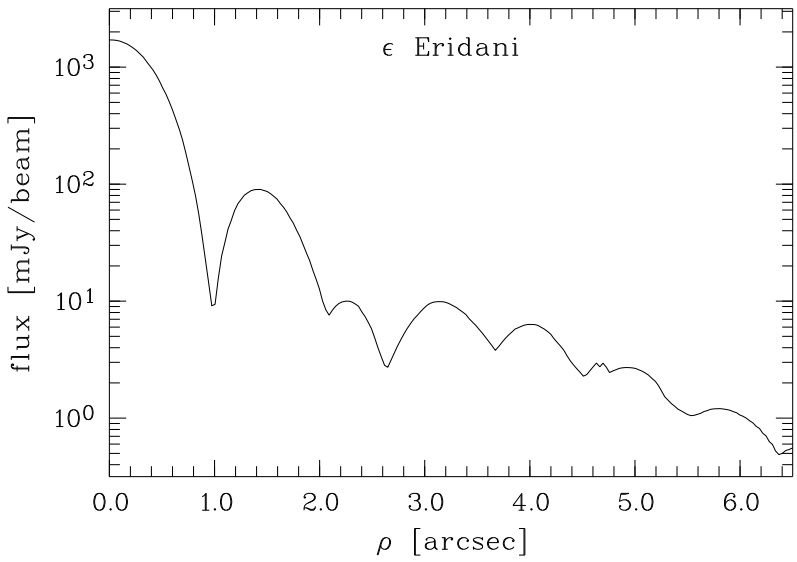

Fig. 10.11: Radial distribution of the PSF structures at 25.5 μm as the maximum flux at a given radial distance. The total flux is scaled to the flux of the ϵ Eri stellar photosphere. To scale it to the HD 107146 stellar photosphere, one has to divide it by 42.3.

Table 10.4: PSF subtraction accuracy necessary for observations on the modeled debris disks.

Run	ρ_{disk} [arcsec]	F_{disk} $\left[\frac{\mathrm{mJy}}{\mathrm{beam}}\right]$	ρ_{peak} [arcsec]	F_{PSF} $\left[\frac{\mathrm{mJy}}{\mathrm{beam}}\right]$	σ [%]
Ia	1.0	21.8	1.4	90.0	2.4
Ib	1.0	55.6	1.4	90.0	6.2
IIa (fo)	2.0	1.3	1.4	2.1	6.2
IIa (eo)	2.0	1.1	1.4	2.1	5.2
IIc (fo)	2.6	0.6	2.3	0.2	30.0
IIc (eo)	3.0	1.3	3.2	0.2	65.0
IId (fo)	3.0	0.2	3.2	0.2	10.0
IId (eo)	3.0	0.9	3.2	0.2	45.0

Notes. The quantity ρ_{disk} denotes the (projected) distance from the star at which the disk flux is measured (the brightest structures of intent), ρ_{peak} denotes the distance from the star of the closest peak of the stellar PSF[3], F_{disk} and F_{PSF} are the surface brightness of the disk and the PSF structures at the corresponding distances, and σ denotes the accuracy at which the stellar PSF has to be subtracted to reduce the PSF structures to 1/10 of the disk structure (i.e., $1/10 \times F_{\mathrm{disk}}/F_{\mathrm{PSF}}$). Values are given for a face-on (fo) and edge-on (eo) orientation of the disk.

necessary for the different runs is given in Table 10.4. This is the result of a comparison of the simulated disk observations (Fig.10.9 and 10.10) and the results plotted in Fig. 10.11. One finds that a PSF subtraction accuracy of 1% is sufficient to detect and spatially resolve all simulated debris disks considered in this study (significantly lower accuracy is needed in some cases). Since this uncertainty dominates the total uncertainty in the observations, very accurate photometry is required in order to scale the reference PSF to the correct level. This represents the minimum requirements to unequivocally detect structures in the model debris disks without further considerations. However, a sophisticated approach might include proper rotation of the optics, so that edge-on seen disks are imaged between the bright hexagonal wings of the PSF – in regions where the PSF structures are less bright – increasing the depth of the observations. Furthermore, it might be possible in some cases to scale the reference PSF to the high order structures of the PSF in regions of the science observations where no significant signal from the disk is expected.

10.5 Conclusions

It has been demonstrated that planet-disk interaction may produce detectable structures in the dust distribution of debris disks. This depends on the configuration of the planet-

[3]Of the two peaks of the PSF next to ρ_{disk} in radial distance, the brighter one is considered.

disk system as well as on the observing wavelength. The detected structures give one the opportunity to infer and characterize extrasolar planets in a range of masses and radial distances from the star unreached by other techniques. In particular, detailed modeling of a combination of high sensitivity, high spatial resolution observations at mid-infrared and (sub-)mm wavelengths allows one to put strong constraints on the configuration of the planet-disk system. It is demonstrated that HST scattered light observations are in most cases unable to unambiguously detect such structures, in particular in face-on seen debris disks. In contrast, both ALMA and the JWST will allow one to detect and spatially resolve the dust distribution in debris disks at a level that enables one to distinguish between different planet-disk configurations. Mid-infrared observations of debris disks with the JWST will allow one to detect and spatially resolve dust in debris disks even at a distance of several tens of AU from the star, where only few dust emission at these wavelengths is expected. For such observations, stellar PSF subtraction with an accuracy of few percent is necessary to unequivocally detect structures in the spatial distribution of the dust.

11 ALMA observations of the AU Microscopii debris disk

The first practical application of the sensitivity studies presented in the previous chapters is an observing program[1] for the first cycle of ALMA observations starting late 2011 (ALMA cycle 0, Early Science, ES). For the observations carried out in this cycle, the first 16 ALMA antennas are already provided for limited observing capabilities. This results in a number of limitations compared to the full array, such as limited sensitivity and spatial resolution. Already at this early stage, ALMA is able to exceed the capabilities of earlier (sub-)mm interferometers. The observing program is summarized in the following.

11.1 Overview

Goal of the project are spatially resolved multi-wavelength observations of the planetesimal belt in the AU Microscopii debris disk. AU Mic is a young, nearby M1e star (12 Myr, 9.9 pc, Zuckerman et al. 2001). It harbors an edge-on seen debris disk (radial extent ≈ 100 AU in scattered light, e.g., Augereau & Beust 2006). It is one of the closest debris disks known and the most prominent one around a low-mass star. Thus, it is particularly well studied in optical to near-infrared scattered light (Liu 2004; Krist et al. 2005; Metchev et al. 2005; Augereau & Beust 2006; Figs. 11.1, and 11.2). The disk has been marginally resolved at 350 μm (Chen et al. 2005). The data give strong evidence for a ring of planetesimals at ≈ 35 AU from the star creating the dust through collisions (Augereau & Beust 2006). Sub-structures in the scattered light surface brightness of the disk have been attributed to planet-disk interaction (Liu 2004; Krist et al. 2005; Fig. 11.2). Its youth makes it particularly interesting to constrain the presence and properties of planets in the system, strongly constraining planet formation time scales and mechanisms.

ALMA ES provides for the first time the sensitivity and spatial resolution to study debris disks at sub-arcsecond resolution in the (sub-)mm. Its compact shape expected in (sub-)mm observations (few tens of AU in radius) and edge-on orientation – resulting in a particularly high surface brightness – make the AU Mic debris disk particularly well suited for these observations (very short observing time necessary). This has been proven by the ALMA test image of the sibling disk around β Pic (ALMA ES Primer[2]).

[1] PI: S. Ertel, accepted as a filler project
[2] http://almascience.eso.org/document-and-tools

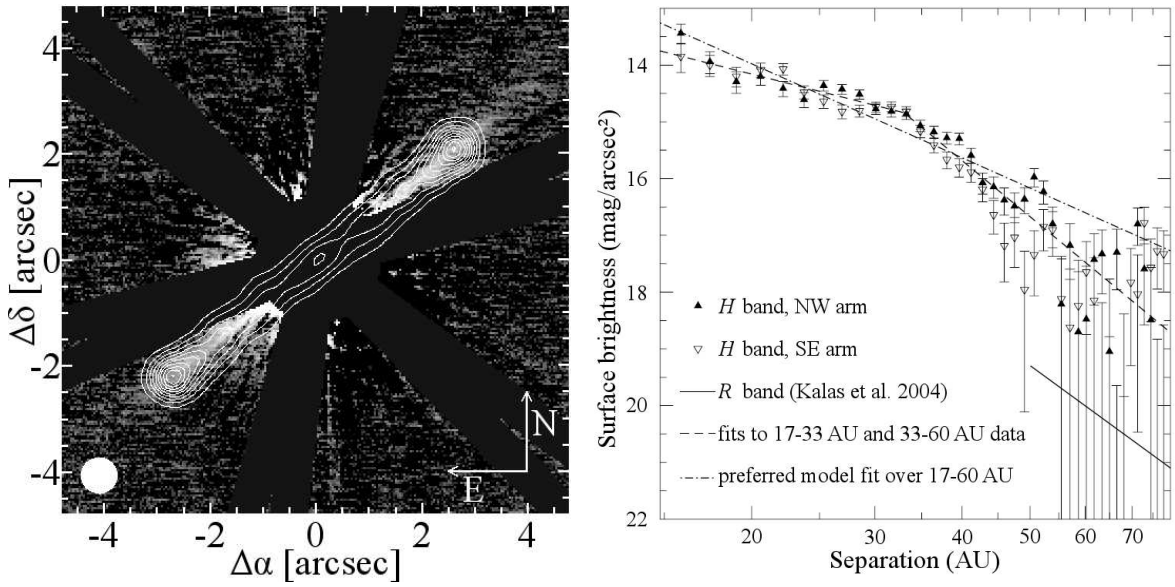

Fig. 11.1: *Left*: Scattered light image from Metchev et al. (2005). Overlayed are contours of the simulated ALMA data at 1250 μm. Contours start at 3 σ with increments of 3 σ. The beam FWHM of the ALMA observations is plotted in the lower left corner. *Right*: Derived radial profile from Metchev et al. (2005). A break in the radial surface brightness at $\approx$ 35 AU is clearly visible.

11.2 Scientific goals of the project

The immediate objective is to reveal and spatially resolve the distribution of large, millimeter-sized dust grains. This information can be extracted directly from the data obtained without the need of detailed modeling. The obtained data will allow one to determine the position and shape of the belt of parent bodies and, thus, to strongly constrain models of how and where the dust is produced. Furthermore, the two most urgent questions left open by previous studies of this system are addressed by ALMA observations:

- *Dust creation mechanisms and dynamics – A bridge from early-type to late-type stars*: The shape of the radial profile of the disk in scattered light is very similar to that of the prototype debris disk around β Pic (A6 V, 12 Myr, 19.3 pc, Zuckerman et al. 2001; Gray et al. 2006; Golimowski et al. 2006). However, since AU Mic is much less luminous, the dynamics in these two well studied debris disks must be dominated by different mechanisms (i.e., radiation pressure for β Pic, stellar wind pressure for AU Mic, Augereau & Beust 2006; Strubbe & Chiang 2006). The data will complement a large variety of spatially resolved scattered light data and SED data. The scattered light data already exhibit radial color gradients attributed to grain segregation (Augereau & Beust 2006). Only a combination of high spatial resolution multi-wavelength observations at scattered light and thermal reemission – building a bridge from the smallest to the largest dust particles and further to planetesimals – can result

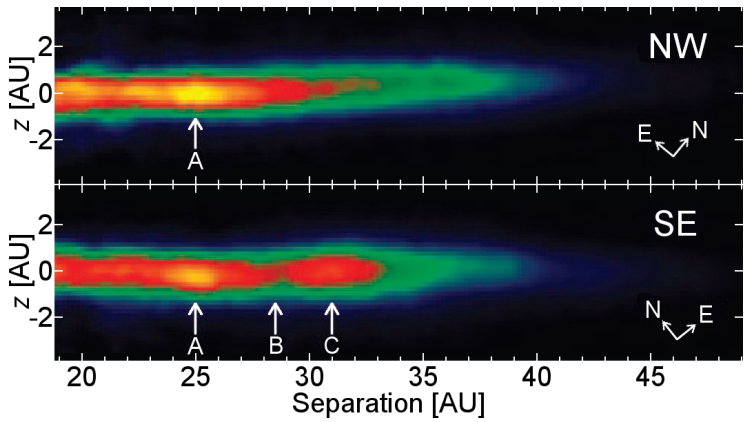

Fig. 11.2: Scattered light data from Liu (2004). White arrows mark the significant substructures in the disk.

in a comprehensive understanding of dust production and the dust and planetesimal dynamics in the system (Krivov 2010; Ertel et al. 2011). One will be able to follow the evolution of the dust grains from their creation to their removal from the system through detailed modeling.

- *Planet formation around low mass stars – Time scales, mechanisms, outcome*: AU Mic is of an age where terrestrial planet formation is expected to climax (Boss 1998; Laughlin et al. 2004). In contrast to the β Pic disk containing a significant amount of (probably not primordial) gas (Beust & Valiron 2007; Zagorovsky et al. 2010), upper limits have been placed on gas present in the AU Mic disk (Roberge et al. 2005). This constrains the time scales of gas removal and disk evolution and, thus, the time

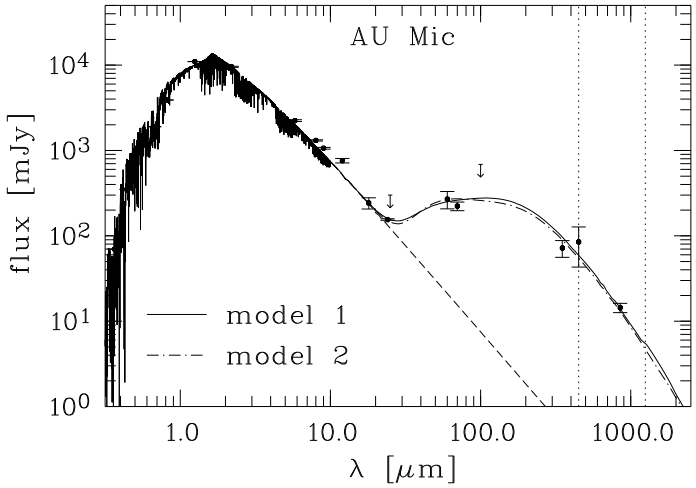

Fig. 11.3: SED fits for AU Mic. Vertical, dotted lines indicate the wavelengths of the proposed observations.

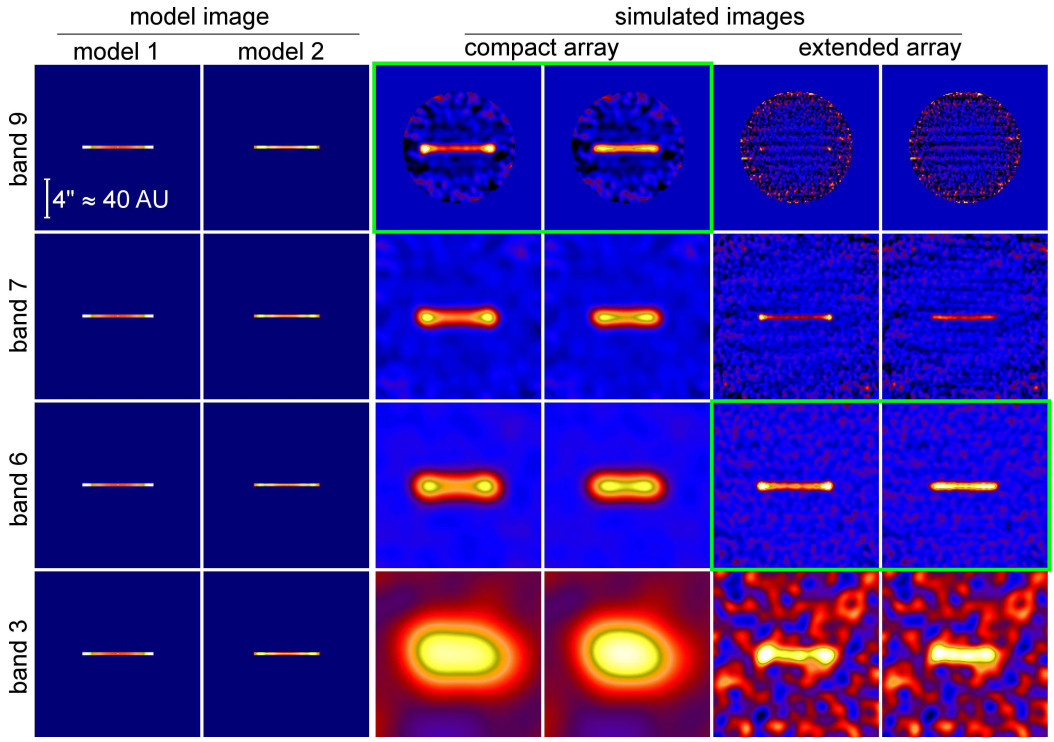

Fig. 11.4: Parameter study to find the optimal array-band-combination for the intended observations. Total observing time for these simulations: 2 h. The images are displayed in arbitrary units, scaled to properly display the SNR. The green boxed configurations give the highest spatial resolution at reasonable SNR (> 10).

scales and mechanisms of gas giant planet formation. This, together with constraining the presence of planets in the system or even the properties of found planets, will strongly establish planet formation models. Signposts of structures in the disk due to planet-disk interaction have already been found in the scattered light data of the AU Mic debris disk (Liu 2004; Krist et al. 2005; Fig. 11.2). Only ALMA observations provide the spatial resolution and sensitivity to unequivocally reveal structures in debris disks induced by planet-disk interaction at (sub-)mm wavelengths.

11.3 Preliminary modeling and observing strategy

To evaluate the observability, the SED of the system has been modeled (Fig. 11.3) using a two power-law approach (radial dust distribution and grain size distribution). The large grains may not be assumed to be distributed the same way as the small ones traced by the scattered light data available due to differences in their dynamics (Augereau & Beust 2006; Strubbe & Chiang 2006; Chapt. 2.2 of the present work). However, the shape of the scattered light profiles provides useful constraints. A break in the radial distribution of the

small grains at ≈ 35 AU (Fig. 11.1) is interpreted as the outer rim of the underlaying parent body distribution (Augereau & Beust 2006). Two models are found (*model 1*: narrow ring at 35 AU, *model 2*: broad disk – outer edge at 35 AU), both being consistent with the entire data set available, but clearly distinguishable in the proposed observations (Fig. 11.4). This illustrates the modeling degeneracies that are to be broken.

Due to the limited number of array-band-combinations available during ES, the observing strategy described in the previous sections cannot be applied directly. Thus, images of the two models are computed at the four wave bands and for both arrays available during ALMA ES. The CASA simulator is used to select the optimal set-up and to estimate the appropriate observing time for the proposed continuum observations (Fig. 11.4). Those combinations are preferred that provide the highest spatial resolution and reasonable SNR (10 to 20) for both models. The compact array in band 9 ($\approx 450\,\mu$m) and the extended array in band 6 ($\approx 1250\,\mu$m) are found to optimally meet these criteria. Furthermore, these combinations provide both very similar spatial resolution ($0\farcs7 \approx 7$ AU, the highest resolution resulting in reasonable SNR in less than 2 hours of observing time) and SNR at two different, well separated wavelengths. This allows for the first time for resolved multi-wavelength observations at (sub-)mm wavelengths that do not suffer from different SNR and spatial resolution. Thus, observations at both bands are proposed.

For the two selected combinations, a peak SNR of ≥ 20 is requested for both models. This results in high sensitivity observations that allow one both to detect sub-structure in the observed disk with high confidence and to detect faint, extended structures associated with the disk. A total observing time (including overheads and calibration) of 165 min at band 9 (compact configuration, RMS of 0.5 mJy/beam) and 54 min at band 6 (extended, required RMS of 0.05 mJy/beam) is found to be necessary to reach the intended SNR. This also provides a good u-v coverage increasing confidence on detected structures.

12 VLT/VISIR imaging of dust in the habitable zone of nearby solar-type stars

The VLT Imager and Spectrometer for the mid-InfraRed (VISIR) is an instrument at one of the Unit Telescopes (Melipal, UT3) of the ESO Paranal observatory. It provides diffraction limited imaging and spectroscopic capabilities. It represents one of the few instruments that provide the user with imaging capabilities that are comparable to the JWST (similar spatial resolution, but significantly lower sensitivity). Thus, for very bright sources it might allow for observations similar to those proposed for the JWST in Sect. 10.4.3. To explore what is already possible with VISIR, a total of $\approx$ 250 debris disk host stars have been searched for significant excess at mid-infrared wavelengths accessible to VISIR. The two most exciting objects found have been selected for pilot observations.

12.1 Target selection

Since the excess of a debris disk in the mid-infrared is usually increasing with wavelengths, the longest waveband of VISIR (Q2, $\lambda_c = 18.72\,\mu$m) has been selected for the observations. The sample of 250 stars has been searched for excess larger than 50 mJy in Q band ($10\,\sigma$ / 1 h integration following the P86 VISIR user manual[1]). Of the objects found, 31 could be observed from Paranal during P86 (Oct. 2010 – Mar. 2011), the period for which the observations were planned. Limiting the distance of the objects to 30 pc, where an emitting area of 20 AU in diameter (Saturn's orbit) can be spatially resolved with VISIR in Q band (diffraction limited FWHM $\approx 0\farcs6$), returns 10 objects. Emission at mid-infrared wavelengths is expected to originate from warm dust located within few AU from a star, comparable to the habitable zone in the system (Smith et al. 2008). 6 of these objects, including famous ones like the edge-on debris disk around β Pic, were already observed with comparable resolution and sensitivity in the mid-infrared. Of the 4 remaining objects, two have been selected for observations:

- ϵ Eri (HD 22049): A solar-type (K2 V) star and one of the "fabulous four" debris disks, together with β Pic, Vega, and Fomalhaut. Its distance of only 3.2 pc allows resolved direct imaging of regions very close to the star ($\approx$ 2 AU in diameter), usually only attainable by interferometry. The disk has been spatially resolved with *Spitzer*/MIPS

[1] http://www.eso.org/sci/facilities/paranal/instruments/visir/doc/

at 24 μm and 70 μm and in the (sub-)mm from the ground (Greaves et al. 1998, 2005; Backman et al. 2009). It is not detected in scattered light. The face-on disk shows a multi-ring structure at 20 AU to 120 AU (Backman et al. 2009). An unresolved component is seen in the MIPS 24 μm image, constrained from SED modelling to a diameter of $\approx$ 6 AU (2″), well resolvable with VISIR in Q band. The excess flux of the disk of 130 mJy (minimum mean surface brightness of the disk of 41 mJy/square-arcsec assuming 130 mJy to be distributed equally in a circular area of $\approx$ 3.2 square-arcsec) is expected to be detectable with VISIR in the Q2 Filter. A Jovian-mass radial velocity planet is known to orbit the star in 3.4 AU (Hatzes et al. 2000). The spectral energy distribution compiled by Backman et al. (2009) and a sketch of the model presented there are shown in Fig. 12.1.

- δ Eri (HD 23249): An old, solar-type (K0IV) star just leaving the main sequence, 9.0 pc from the Sun. Significant excess at 24 μm, but no excess at 70 μm in *Spitzer*/MIPS observations is found (Beichman et al. 2006). This is a strong indication for dust close to the star, but very few dust at distances larger than $\approx$ 20 AU, where most of the dust in other known debris disks is located. Rhee et al. (2007) ruled out contamination by other sources. With an age of 12.6 Gyr (Perrin et al. 1977), this is the first detection of a debris disk around such an old star, indicating that this disk is the result of a more recent event such as the collision of two large bodies orbiting the star. The extent of the disk is estimated adopting a ring in the range of 1 to 5 AU from the star, where dust around a K-type star is expected to be bright in Q band (Smith et al. 2008). The surface brightness of the disk is estimated to 70 mJy/square-arcsec (67 mJy in $\approx$ 0.95 square-arcsec).

In addition to the two science targets, a reference star has to be observed to compare the PSF of this point source with the observations of the science targets. Therefore, γ Eri (M1IIIb) has been selected. It is by a factor of $\approx$ 10 brighter in Q band than the science targets, which allows for short integration times that still result in a high SNR. This allows one to subtract the PSF reference from the science targets without adding significant noise. Being the only suitable reference star at very similar declination and right ascension, γ Eri does not match in optical to near-infrared colors. However, no significant deviations are expected in Q band, where stars of both spectral types K and M are expected to be in the Rayleigh-Jeans regime of their emission.

12.2 Observations

Observations were carried out in service mode. The data of δ Eri were taken on Dec. 12th 2010. The observations of ϵ Eri have been divided into two sequences with half the time on target each, while only one of these sequences has been carried out on Dec. 29th 2010. The second sequence has not been observed due to the high pressure on the telescope. Each observing sequence consisted of an integration on the PSF reference star γ Eri, followed by an integration on the science target, followed again by an integration on γ Eri. This

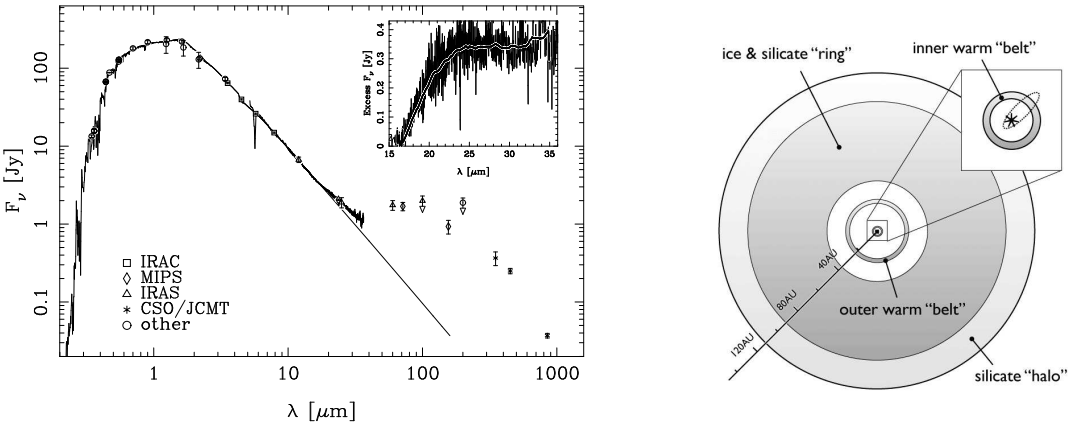

Fig. 12.1: SED of the ϵ Eri system (*left*) and sketch of the model presented by Backman et al. (2009) (right). The innermost ring of dust in this model is the one intended to be imaged in the present work. The Q band excess of the system can be read from the zoomed panel in the SED plot. Both figures are taken from Backman et al. (2009).

sequence was chosen to be able to measure the PSF variation during the observations. The VISIR template `VISIR_img_obs_AutoChopNod` has been used with perpendicular relative Chop/Nod direction, a Chopping Amplitude of 8″ and a Jitter Width of 1″. Total integration times and other relevant information on the exposures are listed in Table 12.1.

The optical DIMM (Differential Image Motion Monitor) seeing was requested to be $\leq 0\farcs8$ (the criterium for diffraction limited observations in Q band as given in the VISIR user manual), which has been fulfilled for all observations of the science targets. However, of the exposures on the PSF reference target, 75% for δ Eri and 50% for ϵ Eri have been observed at optical DIMM seeing between $0\farcs8$ and $1\farcs2$ (or with no seeing value given in the observing log at all). Thus, it cannot be guaranteed that these observations are completely difraction limited.

Table 12.1: Summary of VISIR observations.

Target	Date	Start time [UT]	T [s]	Notes
γ Eri	2010-12-01	3:03	600	PSF reference
δ Eri	2010-12-01	3:24	2138	science target
γ Eri	2010-12-01	4:16	600	PSF reference
γ Eri	2010-12-29	3:14	335	PSF reference
ϵ Eri	2010-12-29	3:28	2430	science target
γ Eri	2010-12-29	4:27	335	PSF reference

12.3 Data reduction and analysis

12.3.1 Reduction and photometric calibration

Standard reductions of the data are provided by the observatory using the VISIR data reduction pipeline (see VISIR data reduction cookbook[2]). The result of the applied observing strategy and data reduction is one frame for each total integration, in which four independent images of the target are visible (Fig. 12.2). Each of these images corresponds to one position of chopping and nodding with 1/4 of the total integration time. Two of these images are positive and two are negative. The images are background subtracted and bias and flat field corrected. From these frames, the four individual images are extracted, respectively, and negative images are converted to positive ones. Photometric calibration is carried out using standard stars provided by the observatory, observed every three hours. Photometry is carried out using the ESO/MIDAS[3] procedure `MAGNITUDE/CIRCLE` for aperture photometry with a circular aperture. The radial width of the concentric radial bins used is 30 pixel for the flux area, 10 pixel no man's land, and 10 pixel for the background area, where one pixel corresponds to $0\farcs075$. The flux area is selected this large ($2\farcs25$ in radius), since the possible disk extent of the science targets has to be included in the aperture. For consistency, the same values are chosen for the photometry of the standard stars. The resulting fluxes have been computed as the average of the four images in one frame of ϵ Eri and δ Eri, respectively, and of the 16 images in four frames of γ Eri. The resulting Q band ($\lambda_c = 18.72\,\mu$m) fluxes are 2.68 Jy, 3.19 Jy, and 32.01 Jy for ϵ Eri, δ Eri, and γ Eri. Uncertainties on the photometry have a number of sources. They include uncertainties of the flux measurements of the standard stars and of the science targets (photometric uncertainty). Additional uncertainties come from the unstable sky transparency between the measurement of a calibrator and a science target (absolute calibration uncertainty). The photometric uncertainty is estimated as the standard deviation of the four independent measurements in each frame. A typical value of 3% and 5% has been found for the science targets and calibrators. The calibration uncertainty can be estimated as the difference of the flux obtained from calibration standards observed prior and after the science observations, which is found to be $\approx 8\%$. This results in a typical uncertainty of the photometric calibration of $\approx 10\%$.

12.3.2 Visualizing the disk

The Q band excess in the ϵ Eri system has been measured by Backman et al. (2009) to ≈ 130 mJy corresponding to $\approx 5\%$ of the total flux of the system. For δ Eri, the excess measured by *Spitzer*/MIPS at 24 μm is ≈ 214 mJy (Beichman et al. 2006) implying an even lower excess at Q band. Thus, the Q band excess in this system can be estimated to be $< 7\%$ of the total flux measured by the present observations. The ad hoc approach to visualize the

[2] http://www.eso.org/sci/facilities/paranal/instruments/visir/doc/VISIR_datareduction-cookbook_v080.0.pdf
[3] http://www.eso.org/sci/software/esomidas/

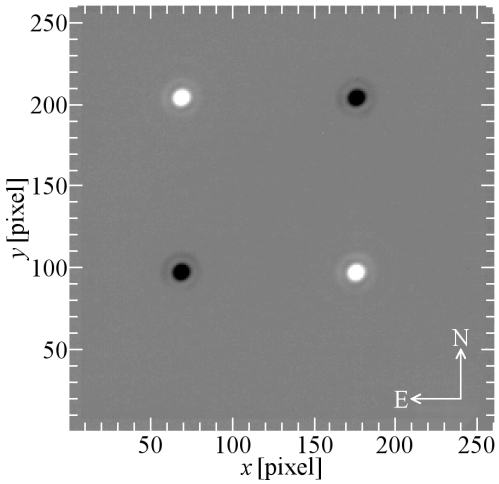

Fig. 12.2: Example of a VISIR frame after standard data reduction. The object is imaged four times in the frame, twice positive and twice negative, with 1/4 of the total integration time each. One pixel corresponds to 0.″075.

disk would be to subtract from the science image the image of the reference star after scaling it to the stellar photosphere. However, one would then have to consider the photometric and calibration uncertainties, which would be much larger than the difference between the two images. Thus, a different approach is used that does not (necessarily) result in a real profile of the disk, but allows to constrain the radial position of the dust. This approach is similar to that used by Gräfe et al. (2011) and is explained in the following. A face-on seen disk is assumed, which is valid for ϵ Eri, but has to be considered when interpreting the results, if the orientation of the disk is not known.

- First, all images of one target corresponding to one observing sequence (Sect. 12.2) are co-aligned on sub-pixel scale and added to increase the SNR in the final image. Therefore, the resolution of the images is increased by a factor of ten through linear rebinning. In the resulting images, the center of the PSF is determined using a two dimensional Gaussian fit. The images are then co-aligned and added. This is done for all images of one science target as well as for all images of the PSF reference star that belong to one of the science targets, respectively.
- In the resulting images, the new center of the PSF is determined in the same way as before. The average of the fluxes and radial distances of all pixels in ten sub-pixel (one native pixel) wide radial bins centered on this position is obtained. These data represent the radial profile of the star-disk system in each stacked image. This way, one profile is created for each science target and one for each corresponding reference star observation.
- The observations of the science targets were diffraction limited, resulting in the fact that seeing variations do not have a significant effect on the uncertainties (in contrast

to Gräfe et al. 2011). Uncertainties on the profiles are, thus, dominated by pixel-to pixel noise and uncertainties in the determination of the center of the PSF. These uncertainties can be estimated as the standard deviation of the fluxes of all pixels in one radial bin. However, this cannot be done on the rebinned images, since the rebinning would falsify the results. Thus, the above step is repeated on the native images. The standard deviation of the mean in each bin is computed. This value is averaged over all profiles (images) of one science target and all corresponding profiles of the reference star and divided by the square root of the number of profiles considered (four for each science target and eight for each reference star observation) to mimic the averaging over all related images of one target.

- The radial positions of the profile measurements in all profiles agree to an accuracy of $\approx$ 1 sub-pixel ($\approx$ 1/10 of an native pixel or $\approx$ 1/70 of the PSF FWHM). Thus, this difference can be ignored and measurements in the same radial bin, but in different profiles can be compared directly. The profile of the reference star is then scaled to the same peak height as the corresponding science target and subtracted from this profile. This intentionally results in an over-subtraction of the stellar contribution from the profiles of the science targets. Hence, the result is a strict lower limit of the contribution of the disk to the profile of the whole system. Uncertainties on the difference profile are computed by adding the uncertainties on the profile of the science target and the reference star, respectively.

12.4 Results

No significant excess has been detected for ϵ Eri ($\approx -0.3\,\sigma$) and for δ Eri ($\approx 0.8\,\sigma$). This is due to the large photometric uncertainty compared to the *Spitzer* data. The *Spitzer*/MIPS and *Spitzer*/IRS data are strong evidence for an excess and the obtained VISIR photometric data are not contradictory to this. Thus, one can assume a disk emitting in the mid-infrared to be present.

The resulting difference profiles obtained for the two science targets are shown in Fig. 12.3. While for ϵ Eri a difference signal with a significance of up to $5\,\sigma$ can be measured, a negative difference signal is seen for δ Eri. This negative signal can be interpreted in the context of some of the exposures on the PSF reference star being not completely diffraction limited but affected by seeing. This is particularly strong for δ Eri for which only 25% of the exposures on the reference target have been observed at conditions where diffraction limited observations can be guaranteed. However, since all exposures on the science target were diffraction limited, this fact will always lead to an over-subtraction of the PSF of the reference star due to its larger extent. Thus, values $< -3\,\sigma$ are not unexpected in the difference profiles and are not contradictory to the uncertainties being reliable. This makes the detection of the extent of the profile of ϵ Eri even stronger. From this profile, one can estimate that significant emission is detected in the range of 1.5 AU to 4.0 AU from the star.

Integrating the ϵ Eri difference profile over the whole range of radii considered, one finds

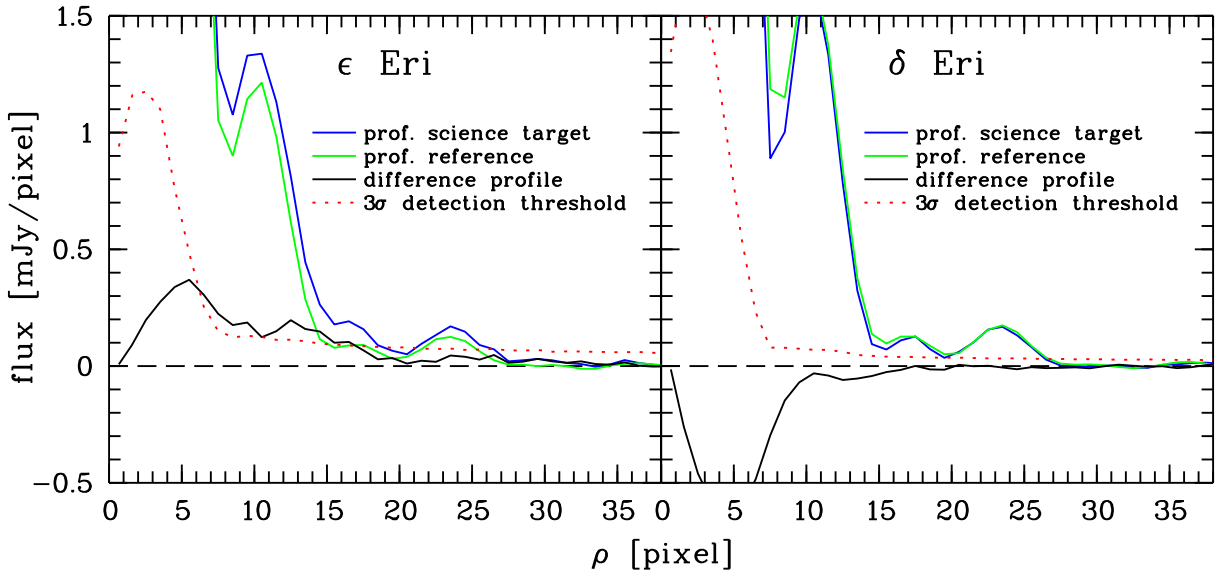

Fig. 12.3: Radial profiles, difference profiles and thresholds for ϵ Eri and δ Eri. Radial distance is measured in native detector pixels, where 1 pix $\widehat{=}$ 0.″075 $\widehat{=}$ 0.24 AU. The uncertainties in the inner regions are dominated by the steep slope of the profiles of science and reference target causing a large scatter of the pixel values in one radial bin. This slope flattens in the innermost regions causing the flattening and inwards decreasing threshold there.

a total flux of 234.6 ± 149.1 mJy where the uncertainty is given as $1\,\sigma$. Integrating it over all radii where significant ($> 3\,\sigma$) flux has been detected, one finds a total flux of 119.1 ± 30.8 mJy. Keeping in mind the large uncertainties, one can compare these values with the excess at the same wavelength of ≈ 130 mJy reported by Backman et al. (2009). Both measurements are consistent with this value, while the value of 119.1 ± 30.8 mJy agrees particularly well. Thus, one can conclude that the subtraction of the PSF of the reference star did not lead to a significant over-subtraction of disk flux. This means that the disk flux has no significant contribution to the central part of the system and that the dust is, hence, distributed in a disk from ≈ 1.5 AU to ≈ 4.0 AU from the star. The average surface brightness of the disk in Q band is then 30.4 ± 7.5 mJy/square-arcsec.

12.5 Conclusions

The inner dust species around ϵ Eri is found to be likely distributed in a broad disk. The origin of this inner disk in the context of the presence of the known planet at very similar distance from the star (Hatzes et al. 2000) has been discussed by Brogi et al. (2009) and Reidemeister et al. (2011) in different ways. Brogi et al. (2009) argue that the origin of the dust must be an Asteroid Belt like ring of planetesimals inside the orbit of the planet, because otherwise the planet would prevent dust produced further away to reach the regions

where it is detected. In contrast, Reidemeister et al. (2011) showed that the planet does not significantly prevent small dust grains to spiral inwards due to Poynting-Robertson drag, and that the dust may have its origin in the outer regions of the debris disk. Since the disk is extended and the predicted orbit of the planet lies between the inner and outer boundaries of the disk, one can conclude that the present observations favor the scenario presented by Reidemeister et al. (2011).

With respect to the feasibility of observations like the ones presented, one can conclude that the success depends very much on the fact that all data obtained are diffraction limited. The sensitivity of VISIR at the status it had during the observations presented in this work is too low to observe a large sample of debris disks[4]. Due to the uncertainties of absolute photometric calibration, the method presented in this work to interpret the data has to be used rather than naive imaging of the disk, as long as these uncertainties cannot be lowered significantly. This method allows one to put strong constraints on the spatial extent of the disk in the case of a detection, but does not allow one to put any constraints on it, if the disk is not detected. In the case of ϵ Eri, a higher SNR of the observations by less than one order of magnitude would already allow one real imaging of the disk rather than only extracting a radial profile due to the easy scaling of the reference PSF possible. The method used favors the detection of mid-infrared bright, extended debris disks with significant inner clearings larger in diameter than the resolution element of the instrument used. Only the much higher sensitivity and the much lower calibration uncertainties of space based instruments like the JWST will allow for spatially resolved, direct imaging of a large number of debris disks in the mid-infrared.

[4]Note that VISIR has been equipped with a new, advanced detector which is available since P89; see P89 user manual for details: http://www.eso.org/sci/facilities/paranal/instruments/visir/doc/

13 Conclusive remarks

13.1 Summary

In the present work, the spatial structure of debris disks has been studied through detailed analytical modeling of available high quality, multi-wavelength data. Therefore, a number of specialized modeling and model fitting tools have been designed. Furthermore, planet-disk interaction in debris disks has been modeled using N-body simulations and strategies for future observations with present and near future instruments have been developed. These strategies have been applied to the preparation and execution of observing programs that aim at spatially resolving the structures in known debris disks. In detail, the results of the present thesis are as follows:

HD 107146 is modeled to be a massive, featureless debris disk with a peak surface density around 130 AU from the star (Chapt. 6). The origin of the ring-like shape is found to be most probably a birth ring scenario. Furthermore, evidence for an additional, inner disk component is found, the origin of which most probably is dust produced at the inner edge of the outer disk and dragged inwards due to Poynting-Robertson drag.

In Chapt. 7, the potential discovery of a new class of debris disks through new *Herschel* data is presented. These disks are predominantly composed of small dust grains. The properties of these disks are investigated via a qualitative discussion of the slope of the SED of a debris disk as well as via detailed modeling. Possible scenarios to explain these disks are presented. However, it is shown that the understanding of data obtained with *Herschel* is still incomplete and that updates of the data reduction pipeline may significantly alter the results.

In Chapt. 8, the modeling of two debris disks is presented that are spatially resolved by *Herschel*/DUNES observations. Evidence for a multi-ring structure or, alternatively, an outwards increasing surface density distribution is found. An outwards increasing surface density of a debris disk can be explained in the context of a birth ring scenario and a disk with low collisional activity.

From the spatially resolved observations and modeling of HD 107146, HD 207129, and q^1 Eri, it has been found that even for massive debris disk that are expected to be clearly collision dominated from earlier estimates, transport mechanisms may play a significant role in the dust dynamics, at least in some regions of the disk.

A general analysis of the capability of ALMA for spatially resolved imaging of debris disks is presented in Chapt. 9 and an observing strategy is suggested. In particular, band 6 (central wavelength 1250 μm) is found to result in the highest SNR for a typical debris disk. It is shown that the best trade-off between high sensitivity and high spatial resolution is

reached, if the spatial resolution of the observations is comparable to the dominating structures in the disk, as long as these structures are bright enough.

Chapt. 10 describes the analysis of structures induced in debris disks due to planet-disk interaction and the observability of these structures with present and future instruments. It is found that this process can result in structures that help to constrain the properties of the planet responsible. The structures are found to be observable with the next generation space-based mid-infrared telescopes such as the JWST as well as with ALMA. In particular, a combination of mid-infrared and (sub-)mm observations results in the strongest constraints on the planetary/planetesimal systems.

Chapt. 11 describes the first practical application of the sensitivity studies presented before. The result is an accepted proposal for the first ALMA observing period (ALMA cycle 0, Early Science). It is demonstrated that even with the limited capabilities of the incomplete ALMA array, it is possible to significantly advance our knowledge about the AU Microscopii debris disk and about the evolution of circumstellar disks and planetary/planetesimal systems in general.

The first spatially resolved observations of the ϵ Eridani innermost debris disk (few AU from the star) are presented in Chapt. 12. The disk is found to be a broad dust ring between 1.5 AU and 4.0 AU from the star. Conclusions on the interaction of the dust and the giant planet at 3.4 AU from the star as well as on the origin of the dust in this disk are drawn from comparison of the observational results to the results of earlier, theoretical studies.

13.2 Outlook

It has been demonstrated that near-future instruments will significantly advance our understanding of the configuration and evolution of planetary/planetesimal systems. New modeling approaches have been developed to account for the expected high quality data. The new observations are expected to reveal the complexity of the systems hidden to previous observations in most of the cases. New, more complex models will be needed to raise to these challenges.

Future high spatial resolution observations at optical to mid-infrared wavelengths will be necessary to confirm the inner disk around HD 107146. Further HST coronagraphic observations have already been executed (program GO 122287, PI: G. Schneider, personal communication) where 8 orbits of STIS coronagraphy in the broadband optical are devoted to probe the inner regions of the HD 107146 disk as close as $\rho = 0\farcs3$ (8.6 AU) from the star.

The search for planets around the host stars of the debris disks presented in Chapt. 7 and detailed collisional and dynamical modeling will confirm or rule out the scenarios to explain the peculiarities of the disks presented there.

ALMA and JWST observations will be necessary to explore whether the models used to simulate planet-disk interaction in debris disks are sufficient or whether the simplifications there are invalid. The ALMA observations of the AU Microscopii disk may give first hints

here. Follow up observations of the spatially resolved debris disks from *Herschel*/DUNES with ALMA will help to further constrain the models of these disks and to investigate the origin of an outwards increasing surface density, as well as the configurations of the planetary/planetesimal systems present.

Further VISIR observations of the innermost regions of the ϵ Eridani debris disk with the new detector will help to further constrain the spatial extent and composition of this dust belt and possibly even to directly image the disk rather than only extracting radial profiles.

List of Figures

List of Tables

Bibliography

Absil, O., E. di Folco, A. Mérand, J.-C. Augereau, V. Coudé du Foresto, D. Defrère, P. Kervella, J. P. Aufdenberg, M. Desort, D. Ehrenreich, A.-M. Lagrange, G. Montagnier, J. Olofsson, T. A. ten Brummelaar, H. A. McAlister, J. Sturmann, L. Sturmann, and N. H. Turner. 2008. A near-infrared interferometric survey of debris disc stars. II. CHARA/FLUOR observations of six early-type dwarfs. A&A**487:**1041–1054.

Absil, O., B. Mennesson, J. Le Bouquin, E. Di Folco, P. Kervella, and J. Augereau. 2009. An Interferometric Study of the Fomalhaut Inner Debris Disk. I. Near-Infrared Detection of Hot Dust with VLTI/VINCI. ApJ**704:**150–160.

Apai, D., M. Janson, A. Moro-Martín, M. R. Meyer, E. E. Mamajek, E. Masciadri, T. Henning, I. Pascucci, J. S. Kim, L. A. Hillenbrand, M. Kasper, and B. Biller. 2008. A Survey for Massive Giant Planets in Debris Disks with Evacuated Inner Cavities. ApJ**672:**1196–1201.

Ardila, D. R., D. A. Golimowski, J. E. Krist, M. Clampin, J. P. Williams, J. P. Blakeslee, H. C. Ford, G. F. Hartig, and G. D. Illingworth. 2004. A Resolved Debris Disk around the G2 V Star HD 107146. ApJ**617:**L147–L150.

Ardila, D. R., D. A. Golimowski, J. E. Krist, M. Clampin, J. P. Williams, J. P. Blakeslee, H. C. Ford, G. F. Hartig, and G. D. Illingworth. 2005. Erratum: "A Resolved Debris Disk around the G2 V Star HD 107146". ApJ**624:**L141–L142.

Augereau, J.-C., O. Absil, J. Bouvier, G. Duchêne, J.-F. Lestrade, S. Maret, C. Martin-Zaïdi, F. Ménard, A. Morbidelli, J. Olofsson, E. Pantin, C. Pinte, and P. Thébault. 2008. DIGIT, GASPS, DEBRIS and DUNES: four HERSCHEL Open Time Key Programs to survey the dust cycle in circumstellar disks. In C. Charbonnel, F. Combes, & R. Samadi, editor. Sf2a-2008, pages 443–+ .

Augereau, J.-C., and H. Beust. 2006. On the AU Microscopii debris disk. Density profiles, grain properties, and dust dynamics. A&A**455:**987–999.

Augereau, J. C., A. M. Lagrange, D. Mouillet, J. C. B. Papaloizou, and P. A. Grorod. 1999. On the HR 4796 A circumstellar disk. A&A**348:**557–569.

Aumann, H. H. 1985. IRAS observations of matter around nearby stars. PASP**97:**885–891.

Aumann, H. H., C. A. Beichman, F. C. Gillett, T. de Jong, J. R. Houck, F. J. Low, G. Neugebauer, R. G. Walker, and P. R. Wesselius. 1984. Discovery of a shell around Alpha Lyrae. ApJ**278:**L23–L27.

Backman, D., M. Marengo, K. Stapelfeldt, K. Su, D. Wilner, C. D. Dowell, D. Watson, J. Stansberry, G. Rieke, T. Megeath, G. Fazio, and M. Werner. 2009. Epsilon Eridani's Planetary Debris Disk: Structure and Dynamics Based on Spitzer and Caltech Submillimeter Observatory Observations. ApJ**690:**1522–1538.

Backman, D. E., and F. Paresce. 1993. Main-sequence stars with circumstellar solid material - The VEGA phenomenon. In E. H. Levy & J. I. Lunine, editor. Protostars and planets iii, pages 1253–1304 .

Beichman, C. A., G. Bryden, T. N. Gautier, K. R. Stapelfeldt, M. W. Werner, K. Misselt, G. Rieke, J. Stansberry, and D. Trilling. 2005*a*. An Excess Due to Small Grains around the Nearby K0 V Star HD 69830: Asteroid or Cometary Debris? ApJ**626:**1061–1069.

Beichman, C. A., G. Bryden, G. H. Rieke, J. A. Stansberry, D. E. Trilling, K. R. Stapelfeldt, M. W. Werner, C. W. Engelbracht, M. Blaylock, K. D. Gordon, C. H. Chen, K. Y. L. Su, and D. C. Hines. 2005*b*. Planets and Infrared Excesses: Preliminary Results from a Spitzer MIPS Survey of Solar-Type Stars. ApJ**622:**1160–1170.

Beichman, C. A., G. Bryden, K. R. Stapelfeldt, T. N. Gautier, K. Grogan, M. Shao, T. Velusamy, S. M. Lawler, M. Blaylock, G. H. Rieke, J. I. Lunine, D. A. Fischer, G. W. Marcy, J. S. Greaves, M. C. Wyatt, W. S. Holland, and W. R. F. Dent. 2006. New Debris Disks around Nearby Main-Sequence Stars: Impact on the Direct Detection of Planets. ApJ**652:**1674–1693.

Beust, H., and P. Valiron. 2007. High latitude gas in the β Pictoris system. A possible origin related to falling evaporating bodies. A&A**466:**201–213.

Binney, J., and M. Merrifield. 1998. Galactic Astronomy. Princeton, NJ: Princeton University Press.

Birnstiel, T., C. P. Dullemond, and F. Brauer. 2010. Gas- and dust evolution in protoplanetary disks. A&A**513:**A79+.

Boccaletti, A., J. Augereau, P. Baudoz, E. Pantin, and A. Lagrange. 2009. VLT/NACO coronagraphic observations of fine structures in the disk of β Pictoris. A&A**495:**523–535.

Boffi, F. R., et al. 2007. "ACS Instrument Handbook", Version 8.0. Baltimore: STScI .

Bohren, C. F., and D. R. Huffman. 1983. Absorption and scattering of light by small particles. New York: Wiley.

Boss, A. P. 1998. Evolution of the Solar Nebula. IV. Giant Gaseous Protoplanet Formation. ApJ**503:**923–+.

Briggs, R. E. 1962. Steady-State Space Distribution of Meteoric Particles under the Operation of the Poynting-Robertson Effect. AJ**67:**268–+.

Brogi, M., F. Marzari, and P. Paolicchi. 2009. Dynamical stability of the inner belt around Epsilon Eridani. A&A**499:**L13–L16.

Brott, I., and P. H. Hauschildt. 2005. A PHOENIX Model Atmosphere Grid for Gaia. In C. Turon, K. S. O'Flaherty, & M. A. C. Perryman, editor. The three-dimensional universe with gaia, volume 576 of *ESA Special Publication*, pages 565–+ .

Brown, M. E., A. J. Burgasser, and W. C. Fraser. 2011. The Surface Composition of Large Kuiper Belt Object 2007 OR10. ApJ**738:**L26+.

Brown, R. H., D. P. Cruikshank, Y. J. Pendleton, and G. J. Veeder. 1997. Surface composition of Kuiper Belt object 1993 SC. Science **276:**937–939.

Bryden, G., C. A. Beichman, D. E. Trilling, G. H. Rieke, E. K. Holmes, S. M. Lawler, K. R. Stapelfeldt, M. W. Werner, T. N. Gautier, M. Blaylock, K. D. Gordon, J. A. Stansberry, and K. Y. L. Su. 2006. Frequency of Debris Disks around Solar-Type Stars: First Results from a Spitzer MIPS Survey. ApJ**636:**1098–1113.

Buenzli, E., C. Thalmann, A. Vigan, A. Boccaletti, G. Chauvin, J. C. Augereau, M. R. Meyer, F. Ménard, S. Desidera, S. Messina, T. Henning, J. Carson, G. Montagnier, J. L. Beuzit, M. Bonavita, A. Eggenberger, A. M. Lagrange, D. Mesa, D. Mouillet, and S. P. Quanz. 2010. Dissecting the Moth: discovery of an off-centered ring in the HD 61005 debris disk with high-resolution imaging. A&A**524:**L1+.

Burns, J. A., P. L. Lamy, and S. Soter. 1979. Radiation forces on small particles in the solar system. Icarus **40:**1–48.

Carpenter, J. M., S. Wolf, K. Schreyer, R. Launhardt, and T. Henning. 2005. Evolution of Cold Circumstellar Dust around Solar-type Stars. AJ**129:**1049–1062.

Chen, C. H., B. M. Patten, M. W. Werner, C. D. Dowell, K. R. Stapelfeldt, I. Song, J. R. Stauffer, M. Blaylock, K. D. Gordon, and V. Krause. 2005. A Spitzer Study of Dusty Disks around Nearby, Young Stars. ApJ**634:**1372–1384.

Corder, S., J. M. Carpenter, A. I. Sargent, B. A. Zauderer, M. C. H. Wright, S. M. White, D. P. Woody, P. Teuben, S. L. Scott, M. W. Pound, R. L. Plambeck, J. W. Lamb, J. Koda, M. Hodges, D. Hawkins, and D. Bock. 2009. A Resolved Ring of Debris Dust around the Solar Analog HD 107146. ApJ**690:**L65–L68.

Crovisier, J., T. Y. Brooke, M. S. Hanner, H. U. Keller, P. L. Lamy, B. Altieri, D. Bockelee-Morvan, L. Jorda, K. Leech, and E. Lellouch. 1996. The infrared spectrum of comet C/1995 O1 (Hale-Bopp) at 4.6 AU from the Sun. A&A**315:**L385–L388.

de Muizon, M. J. 2005. Debris Discs Around Stars: The 2004 ISO Legacy. Space Sci. Rev.**119:**201–214.

Debes, J. H., A. J. Weinberger, and M. J. Kuchner. 2009. Interstellar Medium Sculpting of the HD 32297 Debris Disk. ApJ**702:**318–326.

Dermott, S. F., S. Jayaraman, Y. L. Xu, B. Å. S. Gustafson, and J. C. Liou. 1994. A circumsolar ring of asteroidal dust in resonant lock with the Earth. Nature**369:**719–723.

Dohnanyi, J. S. 1969. Collisional Model of Asteroids and Their Debris. J. Geophys. Res.**74:**2531–+.

Dominik, C., and G. Decin. 2003. Age Dependence of the Vega Phenomenon: Theory. ApJ**598:**626–635.

Draine, B. T. 2003. Scattering by Interstellar Dust Grains. I. Optical and Ultraviolet. ApJ**598:**1017–1025.

Draine, B. T. 2006. On the Submillimeter Opacity of Protoplanetary Disks. ApJ**636:**1114–1120.

Draine, B. T., and A. A. Fraisse. 2009. Polarized Far-Infrared and Submillimeter Emission from Interstellar Dust. ApJ**696:**1–11.

Draine, B. T., and H. M. Lee. 1984. Optical properties of interstellar graphite and silicate grains. ApJ**285:**89–108.

Eiroa, C., D. Fedele, J. Maldonado, B. M. González-García, J. Rodmann, A. M. Heras, G. L. Pilbratt, J. Augereau, A. Mora, B. Montesinos, D. Ardila, G. Bryden, R. Liseau, K. Stapelfeldt, R. Launhardt, E. Solano, A. Bayo, O. Absil, M. Arévalo, D. Barrado, C. Beichmann, W. Danchi, C. Del Burgo, S. Ertel, M. Fridlund, M. Fukagawa, R. Gutiérrez, E. Grün, I. Kamp, A. Krivov, J. Lebreton, T. Löhne, R. Lorente, J. Marshall, R. Martínez-Arnáiz, G. Meeus, D. Montes, A. Morbidelli, S. Müller, H. Mutschke, T. Nakagawa, G. Olofsson, I. Ribas, A. Roberge, J. Sanz-Forcada, P. Thébault, H. Walker, G. J. White, and S. Wolf. 2010. Cold DUst around NEarby Stars (DUNES). First results. A resolved exo-Kuiper belt around the solar-like star ζ^2 Ret. A&A**518:**L131+.

Ertel, S., S. Wolf, C. Eiroa, and the Herschel/DUNES team. 2012. Peculiar debris disks from Herschel/DUNES. submitted to A&A.

Ertel, S., S. Wolf, S. Metchev, G. Schneider, J. M. Carpenter, M. R. Meyer, L. A. Hillenbrand, and M. D. Silverstone. 2011. Multi-wavelength modeling of the spatially resolved debris disk of HD 107146. A&A**533:**A132+.

Fitzgerald, M. P., P. G. Kalas, G. Duchêne, C. Pinte, and J. R. Graham. 2007. The AU Microscopii Debris Disk: Multiwavelength Imaging and Modeling. ApJ**670:**536–556.

Gardner, J. P., J. C. Mather, M. Clampin, R. Doyon, M. A. Greenhouse, H. B. Hammel, J. B. Hutchings, P. Jakobsen, S. J. Lilly, K. S. Long, J. I. Lunine, M. J. McCaughrean, M. Mountain, J. Nella, G. H. Rieke, M. J. Rieke, H.-W. Rix, E. P. Smith, G. Sonneborn, M. Stiavelli, H. S. Stockman, R. A. Windhorst, and G. S. Wright. 2006. The James Webb Space Telescope. Space Sci. Rev.**123:**485–606.

Gautier, T. N., III, G. H. Rieke, J. Stansberry, G. C. Bryden, K. R. Stapelfeldt, M. W. Werner, C. A. Beichman, C. Chen, K. Su, D. Trilling, B. M. Patten, and T. L. Roellig. 2007. Far-Infrared Properties of M Dwarfs. ApJ**667:**527–536.

Golimowski, D. A., D. R. Ardila, J. E. Krist, M. Clampin, H. C. Ford, G. D. Illingworth, F. Bartko, N. Benítez, J. P. Blakeslee, R. J. Bouwens, L. D. Bradley, T. J. Broadhurst, R. A. Brown, C. J. Burrows, E. S. Cheng, N. J. G. Cross, R. Demarco, P. D. Feldman, M. Franx, T. Goto, C. Gronwall, G. F. Hartig, B. P. Holden, N. L. Homeier, L. Infante, M. J. Jee, R. A. Kimble, M. P. Lesser, A. R. Martel, S. Mei, F. Menanteau, G. R. Meurer, G. K. Miley, V. Motta, M. Postman, P. Rosati, M. Sirianni, W. B. Sparks, H. D. Tran, Z. I. Tsvetanov, R. L. White, W. Zheng, and A. W. Zirm. 2006. Hubble Space Telescope ACS Multiband Coronagraphic Imaging of the Debris Disk around β Pictoris. AJ**131:**3109–3130.

Gomes, R., H. F. Levison, K. Tsiganis, and A. Morbidelli. 2005. Origin of the cataclysmic Late Heavy Bombardment period of the terrestrial planets. Nature**435:**466–469.

Gräfe, C., S. Wolf, V. Roccatagliata, J. Sauter, and S. Ertel. 2011. Mid-infrared observations of the transitional disks around DH Tauri, DM Tauri, and GM Aurigae. A&A**533:**A89+.

Gray, R. O., C. J. Corbally, R. F. Garrison, M. T. McFadden, E. J. Bubar, C. E. McGahee, A. A. O'Donoghue, and E. R. Knox. 2006. Contributions to the Nearby Stars (NStars) Project: Spectroscopy of Stars Earlier than M0 within 40 pc-The Southern Sample. AJ**132:**161–170.

Greaves, J. S., W. S. Holland, G. Moriarty-Schieven, T. Jenness, W. R. F. Dent, B. Zuckerman, C. McCarthy, R. A. Webb, H. M. Butner, W. K. Gear, and H. J. Walker. 1998. A Dust Ring around epsilon Eridani: Analog to the Young Solar System. ApJ**506:**L133–L137.

Greaves, J. S., W. S. Holland, M. C. Wyatt, W. R. F. Dent, E. I. Robson, I. M. Coulson, T. Jenness, G. H. Moriarty-Schieven, G. R. Davis, H. M. Butner, W. K. Gear, C. Dominik, and H. J. Walker. 2005. Structure in the ϵ Eridani Debris Disk. ApJ**619:**L187–L190.

Griffin, M., B. Swinyard, L. Vigroux, A. Abergel, P. Ade, P. André, J.-P. Baluteau, J. Bock, A. Franceschini, W. Gear, J. Glenn, M. Huang, D. Griffin, K. King, E. Lellouch, D. Naylor, S. Oliver, G. Olofsson, I. Perez-Fournon, M. Page, M. Rowan-Robinson, P. Saraceno,

E. Sawyer, G. Wright, A. Zavagno, A. Abreu, G. Bendo, A. Dowell, D. Dowell, M. Ferlet, T. Fulton, P. Hargrave, G. Laurent, S. Leeks, T. Lim, N. Lu, H. Nguyen, A. Pearce, E. Polehampton, D. Rizzo, B. Schulz, S. Sidher, D. Smith, L. Spencer, I. Valtchanov, A. Woodcraft, K. Xu, and L. Zhang. 2008. Herschel-SPIRE: design, ground test results, and predicted performance. In Society of photo-optical instrumentation engineers (spie) conference series, volume 7010 of *Society of Photo-Optical Instrumentation Engineers (SPIE) Conference Series*.

Grün, E., B. A. S. Gustafson, S. Dermott, and H. Fechtig. 2001. Interplanetary Dust. Berlin: Springer.

Gustafson, B. A. S. 1994. Physics of Zodiacal Dust. Annual Review of Earth and Planetary Sciences **22:**553–595.

Habing, H. J., C. Dominik, M. Jourdain de Muizon, R. J. Laureijs, M. F. Kessler, K. Leech, L. Metcalfe, A. Salama, R. Siebenmorgen, N. Trams, and P. Bouchet. 2001. Incidence and survival of remnant disks around main-sequence stars. A&A**365:**545–561.

Haniff, C. 2007. An introduction to the theory of interferometry. New A Rev.**51:**565–575.

Hatzes, A. P., W. D. Cochran, B. McArthur, S. L. Baliunas, G. A. H. Walker, B. Campbell, A. W. Irwin, S. Yang, M. Kürster, M. Endl, S. Els, R. P. Butler, and G. W. Marcy. 2000. Evidence for a Long-Period Planet Orbiting ϵ Eridani. ApJ**544:**L145–L148.

Hillenbrand, L. A., J. M. Carpenter, J. S. Kim, M. R. Meyer, D. E. Backman, A. Moro-Martín, D. J. Hollenbach, D. C. Hines, I. Pascucci, and J. Bouwman. 2008. The Complete Census of 70 μm-bright Debris Disks within "the Formation and Evolution of Planetary Systems" Spitzer Legacy Survey of Sun-like Stars. ApJ**677:**630–656.

Holmes, E. K., S. F. Dermott, B. Å. S. Gustafson, and K. Grogan. 2003. Resonant Structure in the Kuiper Disk: An Asymmetric Plutino Disk. ApJ**597:**1211–1236.

Hughes, A. M., D. J. Wilner, S. M. Andrews, J. P. Williams, K. Y. L. Su, R. A. Murray-Clay, and C. Qi. 2011. Resolved Submillimeter Observations of the HR 8799 and HD 107146 Debris Disks. ArXiv e-prints .

Jewitt, D., J. Luu, and J. Chen. 1996. The Mauna Kea-Cerro-Tololo (MKCT) Kuiper Belt and Centaur Survey. AJ**112:**1225.

Jura, M., J. Farihi, and B. Zuckerman. 2007. Externally Polluted White Dwarfs with Dust Disks. ApJ**663:**1285–1290.

Kalas, P., J. R. Graham, E. Chiang, M. P. Fitzgerald, M. Clampin, E. S. Kite, K. Stapelfeldt, C. Marois, and J. Krist. 2008. Optical Images of an Exosolar Planet 25 Light-Years from Earth. Science **322:**1345–.

Kalas, P., J. R. Graham, and M. Clampin. 2005. A planetary system as the origin of structure in Fomalhaut's dust belt. Nature**435:**1067–1070.

Kenyon, S. J., and B. C. Bromley. 2001. Gravitational Stirring in Planetary Debris Disks. AJ**121:**538–551.

Kenyon, S. J., and B. C. Bromley. 2004. Collisional Cascades in Planetesimal Disks. II. Embedded Planets. AJ**127:**513–530.

Kilic, M., T. von Hippel, S. K. Leggett, and D. E. Winget. 2006. Debris Disks around White Dwarfs: The DAZ Connection. ApJ**646:**474–479.

Kring, D. A., and B. A. Cohen. 2002. Cataclysmic bombardment throughout the inner solar system 3.9-4.0 Ga. Journal of Geophysical Research (Planets) **107:**5009.

Krist, J. E., D. R. Ardila, D. A. Golimowski, M. Clampin, H. C. Ford, G. D. Illingworth, G. F. Hartig, F. Bartko, N. Benítez, J. P. Blakeslee, R. J. Bouwens, L. D. Bradley, T. J. Broadhurst, R. A. Brown, C. J. Burrows, E. S. Cheng, N. J. G. Cross, R. Demarco, P. D. Feldman, M. Franx, T. Goto, C. Gronwall, B. Holden, N. Homeier, L. Infante, R. A. Kimble, M. P. Lesser, A. R. Martel, S. Mei, F. Menanteau, G. R. Meurer, G. K. Miley, V. Motta, M. Postman, P. Rosati, M. Sirianni, W. B. Sparks, H. D. Tran, Z. I. Tsvetanov, R. L. White, and W. Zheng. 2005. Hubble Space Telescope Advanced Camera for Surveys Coronagraphic Imaging of the AU Microscopii Debris Disk. AJ**129:**1008–1017.

Krist, J. E., K. R. Stapelfeldt, G. Bryden, G. H. Rieke, K. Y. L. Su, C. C. Chen, C. A. Beichman, D. C. Hines, L. M. Rebull, A. Tanner, D. E. Trilling, M. Clampin, and A. Gáspár. 2010. HST and Spitzer Observations of the HD 207129 Debris Ring. AJ**140:**1051–1061.

Krivov, A. V. 2010. Debris disks: seeing dust, thinking of planetesimals and planets. Research in Astronomy and Astrophysics **10:**383–414.

Krivov, A. V., T. Löhne, and M. Sremčević. 2006. Dust distributions in debris disks: effects of gravity, radiation pressure and collisions. A&A**455:**509–519.

Krivov, A. V., S. Müller, T. Löhne, and H. Mutschke. 2008. Collisional and Thermal Emission Models of Debris Disks: Toward Planetesimal Population Properties. ApJ**687:**608–622.

Kuchner, M. J., and M. J. Holman. 2003. The Geometry of Resonant Signatures in Debris Disks with Planets. ApJ**588:**1110–1120.

Kurucz, R. L. 1969. A Matrix Method for Calculating the Source Function, Mean Intensity, and Flux in a Model Atmosphere. ApJ**156:**235–+.

Laughlin, G., P. Bodenheimer, and F. C. Adams. 2004. The Core Accretion Model Predicts Few Jovian-Mass Planets Orbiting Red Dwarfs. ApJ**612:**L73–L76.

Liseau, R., C. Eiroa, D. Fedele, J.-C. Augereau, G. Olofsson, B. González, J. Maldonado, B. Montesinos, A. Mora, O. Absil, D. Ardila, D. Barrado, A. Bayo, C. A. Beichman, G. Bryden, W. C. Danchi, C. Del Burgo, S. Ertel, C. W. M. Fridlund, A. M. Heras, A. V. Krivov, R. Launhardt, J. Lebreton, T. Löhne, J. P. Marshall, G. Meeus, S. Müller, G. L. Pilbratt, A. Roberge, J. Rodmann, E. Solano, K. R. Stapelfeldt, P. Thébault, G. J. White, and S. Wolf. 2010. Resolving the cold debris disc around a planet-hosting star . PACS photometric imaging observations of q^1 Eridani (HD 10647, HR 506). A&A**518:**L132+.

Lissauer, J. J. 1987. Timescales for planetary accretion and the structure of the protoplanetary disk. Icarus**69:**249–265.

Liu, M. C. 2004. Substructure in the Circumstellar Disk Around the Young Star AU Microscopii. Science **305:**1442–1444.

Liu, M. C., B. C. Matthews, J. P. Williams, and P. G. Kalas. 2004. A Submillimeter Search of Nearby Young Stars for Cold Dust: Discovery of Debris Disks around Two Low-Mass Stars. ApJ**608:**526–532.

Löhne, T., J. Augereau, S. Ertel, J. P. Marshall, C. Eiroa, A. Mora, O. Absil, K. Stapelfeldt, P. Thébault, C. Del Burgo, W. Danchi, A. V. Krivov, J. Lebreton, G. Letawe, P. Magain, J. Maldonado, B. Montesinos, G. L. Pilbratt, G. J. White, and S. Wolf. 2011. Modelling the huge, Herschel-resolved debris ring around HD 207129. A&A, in press.

Löhne, T., A. V. Krivov, and J. Rodmann. 2008. Long-Term Collisional Evolution of Debris Disks. ApJ**673:**1123–1137.

Makino, J. 1991. Optimal order and time-step criterion for Aarseth-type N-body integrators. ApJ**369:**200–212.

Makino, J., and S. J. Aarseth. 1992. On a Hermite integrator with Ahmad-Cohen scheme for gravitational many-body problems. PASJ**44:**141–151.

Maness, H. L., P. Kalas, K. M. G. Peek, E. I. Chiang, K. Scherer, M. P. Fitzgerald, J. R. Graham, D. C. Hines, G. Schneider, and S. A. Metchev. 2009. Hubble Space Telescope Optical Imaging of the Eroding Debris Disk HD 61005. ApJ**707:**1098–1114.

Marois, C., B. Macintosh, T. Barman, B. Zuckerman, I. Song, J. Patience, D. Lafrenière, and R. Doyon. 2008. Direct Imaging of Multiple Planets Orbiting the Star HR 8799. Science **322:**1348–.

Marois, C., B. Zuckerman, Q. M. Konopacky, B. Macintosh, and T. Barman. 2010. Images of a fourth planet orbiting HR 8799. Nature**468:**1080–1083.

Marshall, J. P., T. Löhne, B. Montesinos, A. V. Krivov, C. Eiroa, O. Absil, G. Bryden, J. Maldonado, A. Mora, J. Sanz-Forcada, D. Ardila, J.-C. Augereau, A. Bayo, C. Del

Burgo, W. Danchi, S. Ertel, D. Fedele, M. Fridlund, J. Lebreton, B. M. González-García, R. Liseau, G. Meeus, S. Müller, G. L. Pilbratt, A. Roberge, K. Stapelfeldt, P. Thébault, G. J. White, and S. Wolf. 2011. A Herschel resolved far-infrared dust ring around HD 207129. A&A**529:**A117+.

Matthews, B. C., B. Sibthorpe, G. Kennedy, N. Phillips, L. Churcher, G. Duchêne, J. S. Greaves, J.-F. Lestrade, A. Moro-Martin, M. C. Wyatt, P. Bastien, A. Biggs, J. Bouvier, H. M. Butner, W. R. F. Dent, J. di Francesco, J. Eislöffel, J. Graham, P. Harvey, P. Hauschildt, W. S. Holland, J. Horner, E. Ibar, R. J. Ivison, D. Johnstone, P. Kalas, J. Kavelaars, D. Rodriguez, S. Udry, P. van der Werf, D. Wilner, and B. Zuckerman. 2010. Resolving debris discs in the far-infrared: Early highlights from the DEBRIS survey. A&A**518:**L135+.

Maybhate, A., A. Armstrong, et al. 2010. "ACS Instrument Handbook", Version 10.0. Baltimore: STScI .

Melis, C., M. Jura, L. Albert, B. Klein, and B. Zuckerman. 2010. Echoes of a Decaying Planetary System: The Gaseous and Dusty Disks Surrounding Three White Dwarfs. ApJ**722:**1078–1091.

Metchev, S. A., J. A. Eisner, L. A. Hillenbrand, and S. Wolf. 2005. Adaptive Optics Imaging of the AU Microscopii Circumstellar Disk: Evidence for Dynamical Evolution. ApJ**622:**451–462.

Metchev, S. A., L. A. Hillenbrand, and M. R. Meyer. 2004. Ten Micron Observations of Nearby Young Stars. ApJ**600:**435–450.

Meyer, M. R., L. A. Hillenbrand, D. Backman, S. Beckwith, J. Bouwman, T. Brooke, J. Carpenter, M. Cohen, S. Cortes, N. Crockett, U. Gorti, T. Henning, D. Hines, D. Hollenbach, J. S. Kim, J. Lunine, R. Malhotra, E. Mamajek, S. Metchev, A. Moro-Martin, P. Morris, J. Najita, D. Padgett, I. Pascucci, J. Rodmann, W. Schlingman, M. Silverstone, D. Soderblom, J. Stauffer, E. Stobie, S. Strom, D. Watson, S. Weidenschilling, S. Wolf, and E. Young. 2006. The Formation and Evolution of Planetary Systems: Placing Our Solar System in Context with Spitzer. PASP**118:**1690–1710.

Moór, A., P. Ábrahám, A. Derekas, C. Kiss, L. L. Kiss, D. Apai, C. Grady, and T. Henning. 2006. Nearby Debris Disk Systems with High Fractional Luminosity Reconsidered. ApJ**644:**525–542.

Moro-Martín, A., and R. Malhotra. 2002. A Study of the Dynamics of Dust from the Kuiper Belt: Spatial Distribution and Spectral Energy Distribution. AJ**124:**2305–2321.

Moro-Martín, A., and R. Malhotra. 2003. Dynamical Models of Kuiper Belt Dust in the Inner and Outer Solar System. AJ**125:**2255–2265.

Murray, C. D., and S. F. Dermott. 1999. Solar system dynamics. Cambridge, UK: Cambridge University Press.

Najita, J., and J. P. Williams. 2005. An 850 μm Survey for Dust around Solar-Mass Stars. ApJ**635:**625–635.

Nilsson, R., R. Liseau, A. Brandeker, G. Olofsson, G. L. Pilbratt, C. Risacher, J. Rodmann, J.-C. Augereau, P. Bergman, C. Eiroa, M. Fridlund, P. Thébault, and G. J. White. 2010. Kuiper belts around nearby stars. A&A**518:**A40+.

Oliveira, I., J. Olofsson, K. M. Pontoppidan, E. F. van Dishoeck, J.-C. Augereau, and B. Merín. 2011. On the Evolution of Dust Mineralogy, from Protoplanetary Disks to Planetary Systems. ApJ**734:**51–+.

Oppenheimer, B. R., and S. Hinkley. 2009. High-Contrast Observations in Optical and Infrared Astronomy. ARA&A**47:**253–289.

Ott, S., H. Science Centre, and E. Space Agency. 2010. The Herschel Data Processing System - HIPE and Pipelines - Up and Running Since the Start of the Mission. ArXiv e-prints .

Perrin, M.-N., G. Cayrel de Strobel, R. Cayrel, and P. M. Hejlesen. 1977. Fine structure of the H-R diagram for 138 stars in the solar neighbourhood. A&A**54:**779–795.

Perryman, M. A. C., L. Lindegren, J. Kovalevsky, E. Hoeg, U. Bastian, P. L. Bernacca, M. Crézé, F. Donati, M. Grenon, F. van Leeuwen, H. van der Marel, F. Mignard, C. A. Murray, R. S. Le Poole, H. Schrijver, C. Turon, F. Arenou, M. Froeschlé, and C. S. Petersen. 1997. The HIPPARCOS Catalogue. A&A**323:**L49–L52.

Phillips, N. M., J. S. Greaves, W. R. F. Dent, B. C. Matthews, W. S. Holland, M. C. Wyatt, and B. Sibthorpe. 2010. Target selection for the SUNS and DEBRIS surveys for debris discs in the solar neighbourhood. MNRAS**403:**1089–1101.

Poglitsch, A., C. Waelkens, N. Geis, H. Feuchtgruber, B. Vandenbussche, L. Rodriguez, O. Krause, E. Renotte, C. van Hoof, P. Saraceno, J. Cepa, F. Kerschbaum, P. Agnèse, B. Ali, B. Altieri, P. Andreani, J. Augueres, Z. Balog, L. Barl, O. H. Bauer, N. Belbachir, M. Benedettini, N. Billot, O. Boulade, H. Bischof, J. Blommaert, E. Callut, C. Cara, R. Cerulli, D. Cesarsky, A. Contursi, Y. Creten, W. De Meester, V. Doublier, E. Doumayrou, L. Duband, K. Exter, R. Genzel, J. Gillis, U. Grözinger, T. Henning, J. Herreros, R. Huygen, M. Inguscio, G. Jakob, C. Jamar, C. Jean, J. de Jong, R. Katterloher, C. Kiss, U. Klaas, D. Lemke, D. Lutz, S. Madden, B. Marquet, J. Martignac, A. Mazy, P. Merken, F. Montfort, L. Morbidelli, T. Müller, M. Nielbock, K. Okumura, R. Orfei, R. Ottensamer, S. Pezzuto, P. Popesso, J. Putzeys, S. Regibo, V. Reveret, P. Royer, M. Sauvage, J. Schreiber, J. Stegmaier, D. Schmitt, J. Schubert, E. Sturm, M. Thiel, G. Tofani, R. Vavrek, M. Wetzstein, E. Wieprecht, and E. Wiezorrek. 2010.

The Photodetector Array Camera and Spectrometer (PACS) on the Herschel Space Observatory. A&A**518:**L2+.

Poynting, J. H. 1903. Radiation in the solar system : its effect on temperature and its pressure on small bodies. MNRAS**64:**A1+.

Press, W. H., S. A. Teukolsky, W. T. Vetterling, and B. P. Flannery. 1992. Numerical recipes in FORTRAN. The art of scientific computing. Cambridge, UK: Cambridge University Press.

Reach, W. T. 1997. The structured zodiacal light: IRAS, COBE, and ISO observations. In H. Okuda, T. Matsumoto, & T. Rollig, editor. Diffuse infrared radiation and the irts, volume 124 of *Astronomical Society of the Pacific Conference Series*, pages 33–+ .

Reach, W. T. 2010. Structure of the Earth's circumsolar dust ring. Icarus**209:**848–850.

Reidemeister, M., A. V. Krivov, C. C. Stark, J. Augereau, T. Löhne, and S. Müller. 2011. The cold origin of the warm dust around ϵ Eridani. A&A**527:**A57+.

Rhee, J. H., I. Song, B. Zuckerman, and M. McElwain. 2007. Characterization of Dusty Debris Disks: The IRAS and Hipparcos Catalogs. ApJ**660:**1556–1571.

Roberge, A., A. J. Weinberger, S. Redfield, and P. D. Feldman. 2005. Rapid Dissipation of Primordial Gas from the AU Microscopii Debris Disk. ApJ**626:**L105–L108.

Robertson, H. P. 1937. Dynamical effects of radiation in the solar system. MNRAS**97:**423–+.

Roccatagliata, V., T. Henning, S. Wolf, J. Rodmann, S. Corder, J. M. Carpenter, M. R. Meyer, and D. Dowell. 2009. Long-wavelength observations of debris discs around sun-like stars. A&A**497:**409–421.

Rodmann, J. 2006. Dust in Circumstellar Disks. Ph.D. thesis, University of Heidelberg, http://www.ub.uni-heidelberg.de/archiv/6123.

Safronov, V. S., and E. V. Zvjagina. 1969. Relative Sizes of the Largest Bodies during the Accumulation of Planets. Icarus**10:**109.

Schmitt, W., T. Henning, and R. Mucha. 1997. Dust evolution in protoplanetary accretion disks. A&A**325:**569–584.

Schneider, G., M. D. Silverstone, and D. C. Hines. 2005. Discovery of a Nearly Edge-on Disk around HD 32297. ApJ**629:**L117–L120.

Schwenn, R., and E. Marsch. 1990. Physics of the Inner Heliosphere I. Large-Scale Phenomena. Berlin: Springer.

Sheret, I., W. R. F. Dent, and M. C. Wyatt. 2004. Submillimetre observations and modelling of Vega-type stars. MNRAS**348:**1282–1294.

Sicardy, B., C. Beauge, S. Ferraz-Mello, D. Lazzaro, and F. Roques. 1993. Capture of grains into resonances through Poynting-Robertson drag. Celestial Mechanics and Dynamical Astronomy **57:**373–390.

Silverstone, M. D. 2000. The Vega Phenomenon: Evolution and multiplicity. Ph.D. thesis, UNIVERSITY OF CALIFORNIA, LOS ANGELES.

Smith, R., M. C. Wyatt, and W. R. F. Dent. 2008. The nature of mid-infrared excesses from hot dust around Sun-like stars. A&A**485:**897–915.

Stapelfeldt, K. R., E. K. Holmes, C. Chen, G. H. Rieke, K. Y. L. Su, D. C. Hines, M. W. Werner, C. A. Beichman, M. Jura, D. L. Padgett, J. A. Stansberry, G. Bendo, J. Cadien, M. Marengo, T. Thompson, T. Velusamy, C. Backus, M. Blaylock, E. Egami, C. W. Engelbracht, D. T. Frayer, K. D. Gordon, J. Keene, W. B. Latter, T. Megeath, K. Misselt, J. E. Morrison, J. Muzerolle, A. Noriega-Crespo, J. Van Cleve, and E. T. Young. 2004. First Look at the Fomalhaut Debris Disk with the Spitzer Space Telescope. ApJS**154:**458–462.

Stark, C. C., and M. J. Kuchner. 2008. The Detectability of Exo-Earths and Super-Earths Via Resonant Signatures in Exozodiacal Clouds. ApJ**686:**637–648.

Stark, C. C., and M. J. Kuchner. 2009. A New Algorithm for Self-consistent Three-dimensional Modeling of Collisions in Dusty Debris Disks. ApJ**707:**543–553.

Stern, S. A. 1996. Signatures of collisions in the Kuiper Disk. A&A**310:**999–1010.

Strubbe, L. E., and E. I. Chiang. 2006. Dust Dynamics, Surface Brightness Profiles, and Thermal Spectra of Debris Disks: The Case of AU Microscopii. ApJ**648:**652–665.

Su, K. Y. L., G. H. Rieke, K. A. Misselt, J. A. Stansberry, A. Moro-Martin, K. R. Stapelfeldt, M. W. Werner, D. E. Trilling, G. J. Bendo, K. D. Gordon, D. C. Hines, M. C. Wyatt, W. S. Holland, M. Marengo, S. T. Megeath, and G. G. Fazio. 2005. The Vega Debris Disk: A Surprise from Spitzer. ApJ**628:**487–500.

Su, K. Y. L., G. H. Rieke, J. A. Stansberry, G. Bryden, K. R. Stapelfeldt, D. E. Trilling, J. Muzerolle, C. A. Beichman, A. Moro-Martin, D. C. Hines, and M. W. Werner. 2006. Debris Disk Evolution around A Stars. ApJ**653:**675–689.

Su, K. Y. L., G. H. Rieke, K. R. Stapelfeldt, R. Malhotra, G. Bryden, P. S. Smith, K. A. Misselt, A. Moro-Martin, and J. P. Williams. 2009. The Debris Disk Around HR 8799. ApJ**705:**314–327.

Teplitz, H. I., R. Chary, D. Elbaz, M. Dickinson, C. Bridge, J. Colbert, E. Le Floc'h, D. T. Frayer, J. H. Howell, D. C. Koo, C. Papovich, A. Phillips, C. Scarlata, B. Siana, H. Spinrad, and D. Stern. 2011. Spitzer Infrared Spectrometer 16 μm Observations of the Goods Fields. AJ**141:**1–+.

Tera, F., D. A. Papanastassiou, and G. J. Wasserburg. 1974. Isotopic evidence for a terminal lunar cataclysm. Earth and Planetary Science Letters **22:**1.

Thébault, P. 2009. Vertical structure of debris discs. A&A**505:**1269–1276.

Thébault, P., and J. Augereau. 2007. Collisional processes and size distribution in spatially extended debris discs. A&A**472:**169–185.

Thébault, P., J. C. Augereau, and H. Beust. 2003. Dust production from collisions in extrasolar planetary systems. The inner beta Pictoris disc. A&A**408:**775–788.

Trilling, D. E., G. Bryden, C. A. Beichman, G. H. Rieke, K. Y. L. Su, J. A. Stansberry, M. Blaylock, K. R. Stapelfeldt, J. W. Beeman, and E. E. Haller. 2008. Debris Disks around Sun-like Stars. ApJ**674:**1086–1105.

Udry, S., and M. Mayor. 2008. Exoplanets: The Golden Age of Radial Velocities. In D. Fischer, F. A. Rasio, S. E. Thorsett, & A. Wolszczan, editor. Extreme solar systems, volume 398 of *Astronomical Society of the Pacific Conference Series*, pages 13–+ .

Vitense, C., A. V. Krivov, and T. Löhne. 2010. The Edgeworth-Kuiper debris disk. A&A**520:**A32+.

Voshchinnikov, N. V., and T. Henning. 2008. Is the silicate emission feature only influenced by grain size? A&A**483:**L9–L12.

Voshchinnikov, N. V., V. B. Il'in, T. Henning, and D. N. Dubkova. 2006. Dust extinction and absorption: the challenge of porous grains. A&A**445:**167–177.

Walker, H. J., and R. D. Wolstencroft. 1988. Cool circumstellar matter around nearby main-sequence stars. PASP**100:**1509–1521.

Weinberger, A. J., E. E. Becklin, G. Schneider, B. A. Smith, P. J. Lowrance, M. D. Silverstone, B. Zuckerman, and R. J. Terrile. 1999. The Circumstellar Disk of HD 141569 Imaged with NICMOS. ApJ**525:**L53–L56.

Weinberger, A. J., E. E. Becklin, I. Song, and B. Zuckerman. 2011. The Absence of Cold Dust and the Mineralogy and Origin of the Warm Dust Encircling BD +20 307. ApJ**726:**72–+.

Weingartner, J. C., and B. T. Draine. 2001. Dust Grain-Size Distributions and Extinction in the Milky Way, Large Magellanic Cloud, and Small Magellanic Cloud. ApJ**548:**296–309.

Wetherill, G. W. 1980. Formation of the terrestrial planets. ARA&A**18:**77–113.

Williams, J. P., J. Najita, M. C. Liu, S. Bottinelli, J. M. Carpenter, L. A. Hillenbrand, M. R. Meyer, and D. R. Soderblom. 2004. Detection of Cool Dust around the G2 V Star HD 107146. ApJ**604:**414–419.

Wolf, S., and L. A. Hillenbrand. 2003. Model Spectral Energy Distributions of Circumstellar Debris Disks. I. Analytic Disk Density Distributions. ApJ**596:**603–620.

Wolf, S., and L. A. Hillenbrand. 2005. Debris disk radiative transfer simulation tool (DDS). Computer Physics Communications **171:**208–218.

Wolf, S., A. Moro-Martín, and G. D'Angelo. 2007. Signatures of planets in protoplanetary and debris disks. Planet. Space Sci.**55:**569–581.

Wolf, S., and N. V. Voshchinnikov. 2004. Mie scattering by ensembles of particles with very large size parameters. Computer Physics Communications **162:**113–123.

Wooden, D. H. 2000. Comet Grains: Their IR Emission and Their Relation to ISm Grains. Earth Moon and Planets **89:**247–287.

Wyatt, M. C. 2003. Resonant Trapping of Planetesimals by Planet Migration: Debris Disk Clumps and Vega's Similarity to the Solar System. ApJ**598:**1321–1340.

Wyatt, M. C. 2005. The insignificance of P-R drag in detectable extrasolar planetesimal belts. A&A**433:**1007–1012.

Wyatt, M. C. 2006. Dust in Resonant Extrasolar Kuiper Belts: Grain Size and Wavelength Dependence of Disk Structure. ApJ**639:**1153–1165.

Wyatt, M. C. 2008. Evolution of Debris Disks. ARA&A**46:**339–383.

Wyatt, M. C., C. J. Clarke, and M. Booth. 2011. Debris disk size distributions: steady state collisional evolution with Poynting-Robertson drag and other loss processes. Celestial Mechanics and Dynamical Astronomy pages 39–+ .

Wyatt, M. C., W. R. F. Dent, and J. S. Greaves. 2003. SCUBA observations of dust around Lindroos stars: evidence for a substantial submillimetre disc population. MNRAS**342:**876–888.

Wyatt, M. C., S. F. Dermott, C. M. Telesco, R. S. Fisher, K. Grogan, E. K. Holmes, and R. K. Piña. 1999. How Observations of Circumstellar Disk Asymmetries Can Reveal Hidden Planets: Pericenter Glow and Its Application to the HR 4796 Disk. ApJ**527:**918–944.

Yoneda, S., S. B. Simon, P. J. Sylvester, A. Hsu, and L. Grossman. 1993. Large Siderophile-Element Fractionations in Murchison Sulfides. Meteoritics **28:**465–+.

Zagorovsky, K., A. Brandeker, and Y. Wu. 2010. Gas Emission from Debris Disks Around A and F Stars. ApJ**720:**923–939.

Zuckerman, B., and E. E. Becklin. 1993. Submillimeter studies of main-sequence stars. ApJ**414:**793–802.

Zuckerman, B., I. Song, M. S. Bessell, and R. A. Webb. 2001. The β Pictoris Moving Group. ApJ**562:**L87–L90.

Acknowledgements

Although not considered as co-authors in a thesis, there are always people without the support of whom such a work would never be possible. In particular, I would like to thank

- *Sebastian Wolf* for supervision, continuous support, patience, and for always reminding me to do a little better than I can.
- *Kristin* for going this way with me, for keeping away all tedious trouble, her love and warmth, and last but not least for language editing.
- *Petra Mohr* for language editing.
- *All my friends and colleagues at the ITAP* for the nice atmosphere, the scientific and the worldly discussion, for sharing their wisdom, for teaching me pudency, and last but not least for all the fun we had.
- *All collaborators and co-authors* for their support, for sharing their wisdom, for the scientific discussion, and for language editing.
- *Brigitte Kuhr* and *Holger Boll* for administrative and IT support, much more than it was their job.

Furthermore, I thank for financial support by the state of Schleswig-Holstein and by the DFG under contract WO857/7-1.

Erklärung

Hiermit erkläre ich, dass

(1) die Arbeit, abgesehen von Beratung durch den Betreuer Prof. Dr. S. Wolf, nach Inhalt und Form die eigene Arbeit ist, sofern nicht im Text ausdrücklich anders angegeben,

(2) die Arbeit keiner anderen Stelle im Rahmen eines Prüfungsverfahrens vorgelegen hat oder vorliegt,

(3) Teile der Arbeit veröffentlicht worden sind oder zur Veröffentlichung eingereicht wurden: Ertel et al. (2011, 2012); Löhne et al. (2011),

(4) die Arbeit unter Einhaltung der Regeln guter wissenschaftlicher Praxis der Deutschen Forschungsgemeinschaft entstanden ist.

Steve Ertel